

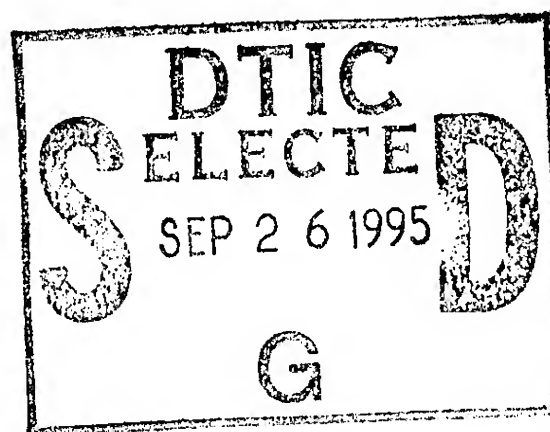


NRL/MR/6722--95-7656

# Advanced Radiation Theory Support Annual Report 1994, Final Report

RADIATION HYDRODYNAMICS BRANCH

*Plasma Physics Division*



July 28, 1995

DTIC QUALITY INSPECTED 1

Approved for public release; distribution unlimited.

19950922 119

REPORT DOCUMENTATION PAGE			Form Approved OMB No. 0704-0188	
Public reporting burden for this collection of information is estimated to average 1 hour per response, including the time for reviewing instructions, searching existing data sources, gathering and maintaining the data needed, and completing and reviewing the collection of information. Send comments regarding this burden estimate or any other aspect of this collection of information, including suggestions for reducing this burden, to Washington Headquarters Services, Directorate for Information Operations and Reports, 1215 Jefferson Davis Highway, Suite 1204, Arlington, VA 22202-4302, and to the Office of Management and Budget, Paperwork Reduction Project (0704-0188), Washington, DC 20503.				
1. AGENCY USE ONLY (Leave Blank)	2. REPORT DATE  July 28, 1995	3. REPORT TYPE AND DATES COVERED  Final Report		
4. TITLE AND SUBTITLE  Advanced Radiation Theory Support Annual Report 1994, Final Report			5. FUNDING NUMBERS	
6. AUTHOR(S)  Radiation Hydrodynamics Branch				
7. PERFORMING ORGANIZATION NAME(S) AND ADDRESS(ES)  Naval Research Laboratory Washington, DC 20375-5320			8. PERFORMING ORGANIZATION REPORT NUMBER  NRL/MR/6722--95-7656	
9. SPONSORING/MONITORING AGENCY NAME(S) AND ADDRESS(ES)  Defense Nuclear Agency RAEV Alexandria VA 22310			10. SPONSORING/MONITORING AGENCY REPORT NUMBER	
11. SUPPLEMENTARY NOTES  This research was sponsored by the defense Nuclear Agency under Job Order Title, "Advanced Radiation Theory Support," MIPR No. 94-557.				
12a. DISTRIBUTION/AVAILABILITY STATEMENT  Approved for public release; distribution unlimited.			12b. DISTRIBUTION CODE	
13. ABSTRACT (Maximum 200 words)  This report details the work of the Radiation Hydrodynamics Branch conducted in FY94 with respect to several critical problems concerning (1) the analysis of experimental z-pinch data, (2) the optimization of PRS performance on existing pulse-power generators, and (3) the design and analysis of advanced simulator z-pinch experiments. Separate sections describe progress in (1) the analysis of Physics International Inc. (PI) A1/Mg mixture experiments, (2) the design and analysis of A1 experiments at PI that produced a doubling of previous K-shell yields, (3) an analysis of Saturn data that correlated x-ray yields with the mass fraction of plasma that produced the radiation, (4) proposals for new PRS experiments that should increase mass participation, decrease plasma opacity, and increase x-ray yields and simulation fidelity, (5) the identification of new issues for scaling K-shell yields to higher photon and output energies, (6) calculations of the effects of MITL losses on power flow to PRS loads in advanced multi-mega-ampere simulators, (7) the development of diagnostics for determining the opacity of line emission in PRS plasmas, and (8) the development of diagnostics to measure the rate of ionization through the L-shell of moderate atomic number plasmas such as nickel or selenium.				
14. SUBJECT TERMS  Z-pinch physics Plasma radiation sources Radiation MHD			15. NUMBER OF PAGES  93	
			16. PRICE CODE	
17. SECURITY CLASSIFICATION OF REPORT  UNCLASSIFIED	18. SECURITY CLASSIFICATION OF THIS PAGE  UNCLASSIFIED	19. SECURITY CLASSIFICATION OF ABSTRACT  UNCLASSIFIED	20. LIMITATION OF ABSTRACT  UL	

## CONTENTS

Executive Summary . . . . .	E-1
I. Enhancing Kilovolt Yields by Mixing Elements of Similar Atomic Number . . . . .	1
II. Increasing X-ray Emission in PRS Loads through Comparisons of Theory with Experiment . . . . .	6
III. Important Inferences Derived from a Theoretical Data Analysis of the Saturn Aluminum PRS Experiments . . . . .	24
IV. Increasing X-ray emission in PRS Loads Through Comparisons of Experiment with Experiment . . . . .	37
V. Low $\eta$ Scaling of K-shell Emission with Mass and Z . . . . .	47
VI. The effect of Lossy MITLs on Power Flow in DECADE-and Jupiter-class Generators . . . . .	55
VII. Diagnosing the Opacity of K Shell Lines in Z Pinches . . . . .	67
VIII. Diagnosing Plasmas using Line Ratios of Satellite to Resonance Lines in the L-Shell . . . . .	72
References . . . . .	78

Accession For	
NTIS CRA&I	<input checked="" type="checkbox"/>
DTIC TAB	<input type="checkbox"/>
Unannounced	<input type="checkbox"/>
Justification _____	
By _____	
Distribution / _____	
Availability Codes	
Dist	Avail and/or Special
A-1	

## EXECUTIVE SUMMARY

This report describes theoretical work carried out in support of the Plasma Radiation Source (PRS) RAST Program by Code 6720 in FY 1994. A strong collaboration between theory and experiment over the last several years has led to a greater understanding of ways to optimize the coupling of PRS loads to pulsed power. The pathway that has been followed has led continually to higher x-ray yields and to greater understanding of the next steps that are needed to continue the process. Along the way, a number of milestones have been achieved, which are described in this report. The eight sections of the report discuss the following subjects:

- (1) Some excellent data and its analysis led the way to a valuable discovery this year at PI in experiments that used Al wires coated with Mg. A significant departure from slug model implosion dynamics was observed. It produced close to a factor of two increase in K-shell yields when combined with reductions in the K-shell opacities that were produced by the mixed element load design. The theoretical motivation for these experiments is discussed in Section I, and results of the analysis of the spectral data are presented.
- (2) The first demonstration was made this year on Double Eagle of pure aluminum K-shell yields in excess of 50 kJ for 2 cm length loads. The possibility now exists that Double Eagle could equal Saturn's present kilovolt x-ray production in the near future, because there are four options available to pursue this goal. Coated Mg/Al wires could be used in place of pure Al. Loads that are longer than 2 cm could be used. Staggered wire loads could improve performance at larger array diameters and larger kinetic energy inputs. Finally, Double Eagle could be operated at somewhat higher operating voltages. Double Eagle achieved its record yields by operating at larger radii with longer implosion times than it was ever operated at before. The rationale for these experiments is described in Section II. Section II also contains a description of a complementary approach to the "hard-implosion" yield scaling that was used earlier to guide JDOST. It should help to provide a more accurate understanding of how yields scale with mass, implosion velocity, and atomic number. It should eventually provide new guidance for interpreting and understanding experimental PRS data. A comparison of these new theoretical results with the new Double Eagle data is also made in Section II. *Double Eagle's performance has important consequences for DECADE PRS. If DECADE were to achieve 10 times the PRS performance of Double Eagle and Double Eagle were to achieve 100 kJ kilovolt outputs, then DECADE might produce megajoule outputs at 1.5 to 2 keV and greatly exceed its original PRS specs. Moreover, it might achieve this performance without the use of a POS and before all of the bremsstrahlung operational problems are worked out.*
- (3) A complete set of spectral data from the Saturn experiments that were conducted two years ago was completed this year. The data included (1) digitized K-series spectra from which accurate line ratios were computed, (2) K-shell pinhole pictures from which plasma size information was inferred from computer scans of the pictures, (3) XRD traces from which x-ray pulsewidths were inferred, and (4) total K-shell yields. A self-consistent analysis of this data shows trends in the temperatures, densities, and masses of the plasmas from which the emissions took place. In particular, this analysis of the Saturn data showed systematic trends



in the plasma mass participation in the K-shell emission that correlated directly with the yield behavior. This work is discussed in Section III.

- (4) Useful inferences about PRS load design can be drawn from a comparison of the experiments described in Sections I and III. These are discussed in Section IV. The data analyses of these Double Eagle and Saturn experiments confirm a conjecture that was drawn from an earlier analysis of the Saturn yield data alone; namely, that the wire explosion dynamics overlapped deleteriously with the wire array implosion dynamics on Saturn because of the short current risetime of the Saturn generator. A new series of Saturn experiments is proposed in Section IV, using wire loads that should reduce this overlap. If these experiments are carried out and higher yields are observed than were measured in the earlier Saturn experiments, then they would further demonstrate the value and benefits of the data analysis presented in Section III.
- (5) In order to achieve larger x-ray yields at higher x-ray energies, one must generate implosions with higher atomic number elements than Al or Ar that radiate in the K-shell. However, the pulse-power requirements become more severe as one goes up in atomic number, so that it becomes increasingly important to seek ways to optimize x-ray emission from moderate atomic number loads at low  $\eta$ : ( $\eta \sim 1$ ). The scaling of K-shell yields with load mass and atomic number,  $Z$ , at low  $\eta$  was investigated this year and some preliminary results are presented in Section V. In particular, when large implosion velocities are reached for moderate  $Z$  materials, the gradient structure of the plasma has an important influence on x-ray yield scaling. These effects were ignored in the JDOST exercise, but they should not be in the future.
- (6) The conversion of the PBFA II pulse-power generator at Sandia National Laboratories to PRS mode will provide useful data on power flow to the PRS load and on PRS performance at megajoule PRS load energies. Power flow calculations are providing crucial guidance for this redesign effort. How well the MITLs are magnetically insulated and how leakage currents affect power flow are problems affecting both PBFA II and Jupiter designs. These problems were investigated this year for both DECADE- and Jupiter-sized generators and found to have a manageable effect on the power flow. Soft drivers, like DECADE and Jupiter, respond to a convolute short by sending more energy to the load. For PRS loads, the net result is a weaker loss of yield than one might have otherwise expected. This work is reported on in Section VI.
- (7) For many years, the K shell lines of neon ( $Z=10$ ), aluminum ( $Z=13$ ), and argon ( $Z=18$ ) have served as the workhorse elements in DNA simulators, providing x-ray simulation capability in the 1-3 keV region. In experiments using presently available machines, the lines within the K-shell are greatly affected by self-absorption and are optically thick, with optical depths typically in the hundreds. When simulations of a measured K-series spectrum were carried out this year, a discrepancy between the calculated relative amounts of line and continuum radiation and the measured amounts was noted. The H- and He-like recombination edges were easily visible on a theoretical spectrum but barely detectable to the eye on the actual measured pinch spectrum. The calculated continuum comprised 60% of the keV and harder radiation; whereas, it was measured at 25%. Models generally predict a greater fraction of the keV radiation to be in the continuum than is observed. In general, the problem of controlling the

amount of line to continuum radiation in PRS simulators is critical for improving simulation fidelity. The problem of diagnosing line opacities as well as a possible explanation for the discrepancy between experimental and theoretical line-to-continuum ratios is discussed in Section VII.

- (8) A small effort continued in FY94 to construct scalable L-shell multiplet models for use in diagnosing PRS experiments on DECADE and ACE IV. This work is also relevant to problems such as L-shell burn-through. The model development, which is discussed in Section VI, is patterned after the successful use of hydrogen- to helium-like line ratios and power outputs to derive information about the state of a plasma radiating in the K-shell. The same procedures are needed for inferring plasma properties such as temperature and mass for L-shell emissions. These procedures are the critical design element for building thermometers and weight gauges for PRS plasmas. In the L-shell, the multiplet structure of the bound states complicates the problem of building reliable L-shell dynamical models and diagnostics; however, while more work is needed than was necessary for building the K-shell diagnostics, the problem is being handled with years of atomic physics experience and today's computer resources to make it possible.

# ADVANCED RADIATION THEORY SUPPORT ANNUAL REPORT 1994, FINAL REPORT

## I. ENHANCING KILOVOLT YIELDS BY MIXING ELEMENTS OF SIMILAR ATOMIC NUMBER

About a decade ago it was suggested (Apruzese and Davis, J. Appl. Phys. **57**, p. 4349) that the K shell power emitted by a Z pinch plasma could be enhanced by mixing two or more elements of similar atomic number in the load. DNA has been urged to sponsor such experiments for some time (Whitney et al., NRL Memorandum Reports 5970 and 6873, published in 1987 and 1991, respectively). Until recently, however, there had been no experimental test of this concept. During this past year, experiments on Double Eagle at Physics International Co. have shown that pinches comprised of both Al and Mg produce yields up to 50% greater than pure Al pinches imploded under the equivalent conditions. Using Mg-coated Al wires, these shots have also demonstrated that the outer regions of the wire tend to boil off prior to the main pinch. They are then drawn to the axis by the usual  $J \times B$  forces, where they form a plasma somewhat hotter than the later arriving material which surrounds it and comes from the remainder of the wires. This technique can be controlled and used to enhance the yields of existing and future simulators, and has provided valuable insight into load behavior.

The physics behind the mixture enhancement is as follows. First, assume that the principal 1-2 resonance lines of the H- and He-like stages provide a substantial amount of the K shell yield. If the average optical depth of these two lines is  $\tau$  in a one-element pinch, and we replace half of that element with a new element of similar atomic number, there will now be four distinct 1-2 resonance lines, of optical depth  $\tau/2$ , in the resulting two-element pinch. Obviously, in an n-element pinch, there will be  $2n$  distinct strong resonance lines, of approximate optical depth  $\tau/n$ . Thus, by mixing elements, the number of lines is increased, and their opacity is reduced, a promising recipe for both greater power and better simulator spectrum fidelity. Of course, there are fewer ions of each element than would be the case in a one-element pinch of the same mass load. Therefore, the degree of enhancement of the power and/or yield depends on the functional form of the photon escape probability vs. optical depth.

There are two different types of escape probability. The single flight escape probability, usually designated by  $P_e$ , is the probability that a line photon, following emission, leaves the plasma without further interaction with any other particle in that plasma. The probability which is most relevant for the present considerations, however, is the so-called ultimate escape probability,  $P_u$ . Following emission, the line photon may be absorbed by another ion and is very likely to be emitted in the same transition at a slightly different frequency within the line profile. Of course, there is also a chance that the line photon will be destroyed by collisional processes while the ion is in an excited state.  $P_u$  is the probability that, after any number of absorptions and re-emissions, the photon still leaves the plasma. Calculation of these quantities involves detailed knowledge of the atomic rates and line profile, as well as the plasma temperature, density, and size. Fig. 1 illustrates schematically the difference between these quantities and shows a sample calculation for Al and Mg for various fractions of these elements under typical Z pinch conditions.

Fig. 1b shows that if 20% of the Al is removed, the ultimate escape probability for the He-like 1-2 line increases by 11%, from 0.087 to 0.097. Therefore, even though there will be 20% fewer

photons internally generated, this will be partially compensated by their increased chance of escape, causing the Al emissivity to fall to only 89% of its pure-pinch value in the  $\text{He}\alpha$  line. Notice that the  $P_u$  for the corresponding Mg line, assuming a 20% Mg fraction to replace the Al, is 0.64, much higher than that for Al when Al dominates the composition of the load. Photons generated by these Mg ions have an excellent chance of escape, increasing the overall emissivity of the plasma in the keV region of the spectrum.

The experiments at Physics International Co. found that the yield maximized at 50% greater than the pure-Al value when Mg comprised 20% of the load. Fig. 2 illustrates the experimental and predicted fraction of the line yield which is in the Mg lines vs. the Mg fraction. Even though there is considerable scatter in the data, it is clear that the experimental numbers track the predictions. Note that, with only 20% of the load composed of Mg, Mg lines account for 50% of the emitted radiation. Temperatures of the Al and Mg components were separately derived using spectroscopic analysis. Fig. 3 shows that the Al temperatures cluster around 300 eV, whereas the temperature of the Mg component is around 600 eV. This is indirect but powerful evidence that the Al and Mg are spatially separated. Two additional pieces of data confirm this picture. First, spectra from shots have been taken on the Blackjack 5 machine at Maxwell Laboratories, Inc, with Al:Mg alloy wires, in which the Mg and Al are uniformly mixed and cannot separate. These spectra indicate that the Al and Mg have the same temperature, as expected. Also time-resolved Double Eagle data show the Mg lines lighting up 10 ns before the Al, strongly suggesting the the outer Mg coating is imploding and heating first.

In summary, the coated wire array experiments demonstrate that the keV radiation efficiencies of optically thick plasmas can be increased by mixing elements of nearby atomic number. Moreover, the Mg-coated arrays have also allowed us to investigate and gain new and confirmed knowledge about some of the important wire array dynamics. These results support the idea that the wires are not imploding as a shell, but, rather, the outer wire material is blown in ahead of the interiors of the wires. This precursor plasma achieves a higher temperature in the core and radiates very efficiently. If, as in the case demonstrated by these experiments, the core plasma is a different element than the bulk plasma, core radiation freely escapes through the shell, contributing to enhanced yields. Obviously, these results have significant impacts on wire array load design. As loads are scaled to higher current generators where higher masses will in turn cause higher atomic number elements to become optically thick, mixing nearby atomic number elements and controlling the amount of core plasma will increase radiation efficiencies. Moreover, if the core plasma is hot and relatively dense, then coating a higher atomic number on the outside of the cold wires could be more useful. Future experiments will study such loads, and better diagnose these pinches, and also investigate the behavior of coated loads as functions of wire number and initial diameter.

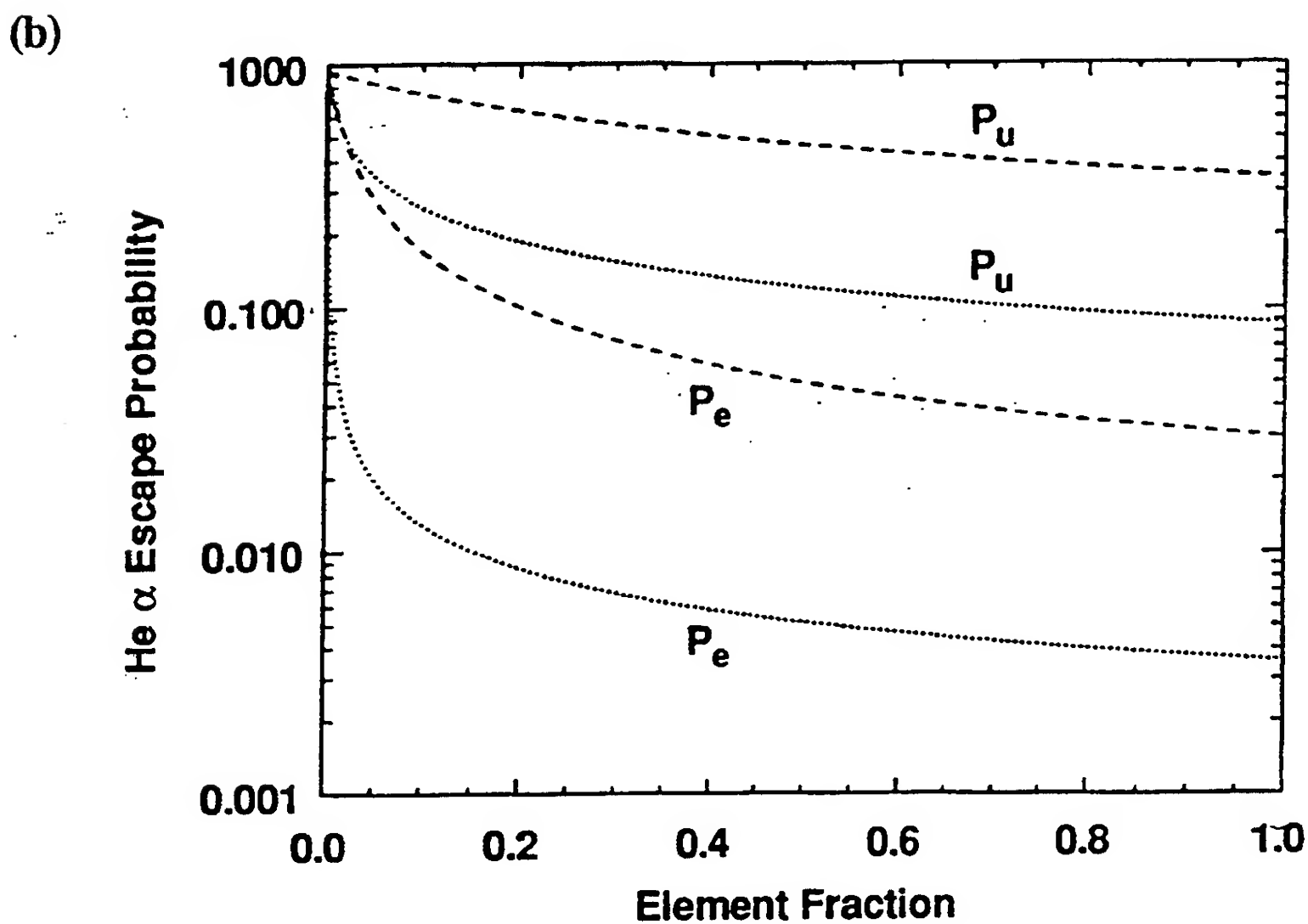
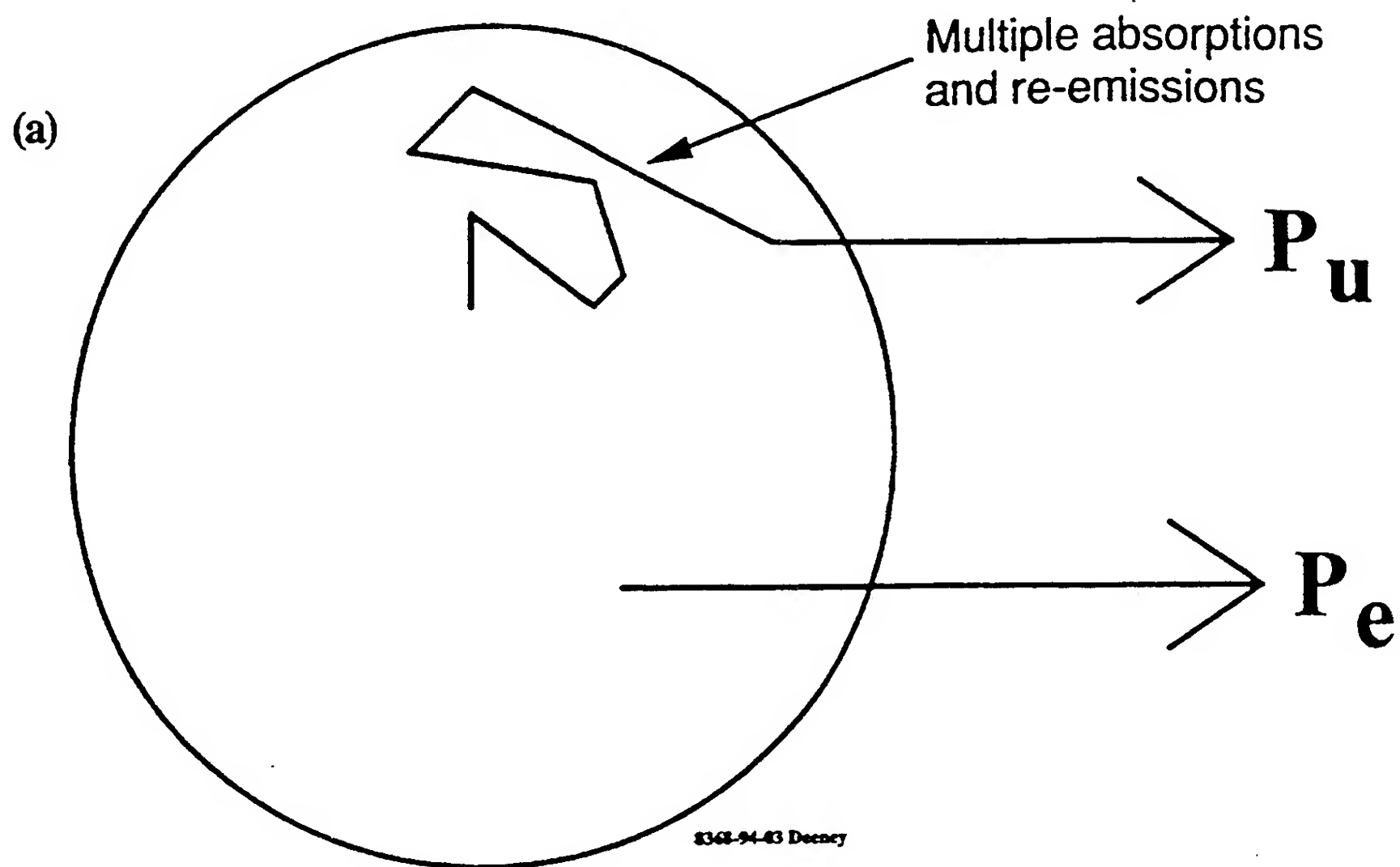


FIG. 1. (a) There are two different escape probabilities for a photon from a plasma: the ultimate escape probability,  $P_u$ , and the local single flight escape probability  $P_e$ .  $P_u$  depends on  $P_e$  and on the probability of collisional loss,  $P_q$ . (b) As the element fraction increases, both probabilities of escape decrease. The optimum is a mix which will maximize the combined probability of escape. This result is for aluminum (dotted lines) and magnesium (dashed lines). The plasma diameter is 3 mm, electron density is  $10^{21}$  cm $^{-3}$ . The line modeled is He-like  $1s^2-1s2p$   $^1P_1$ .

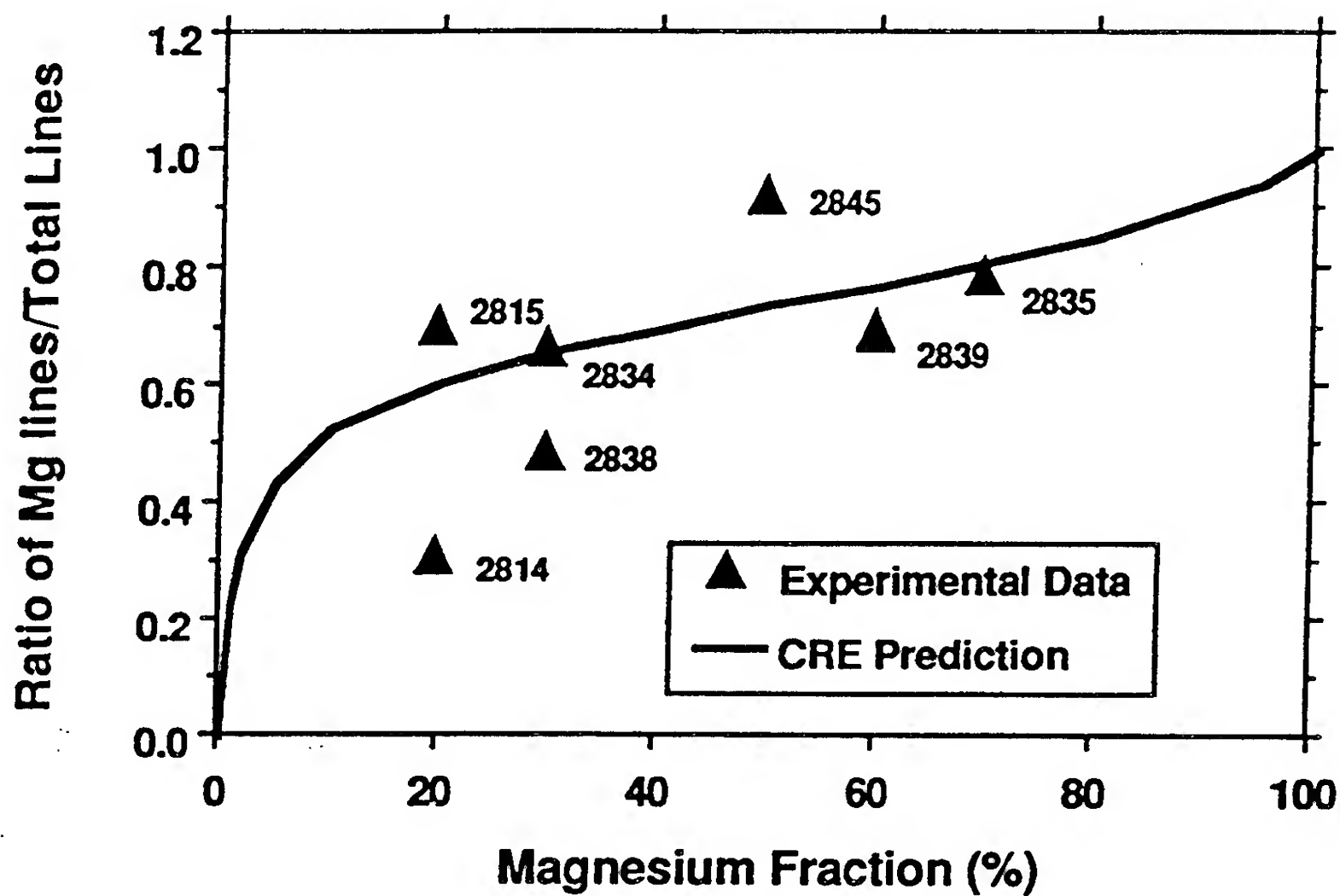
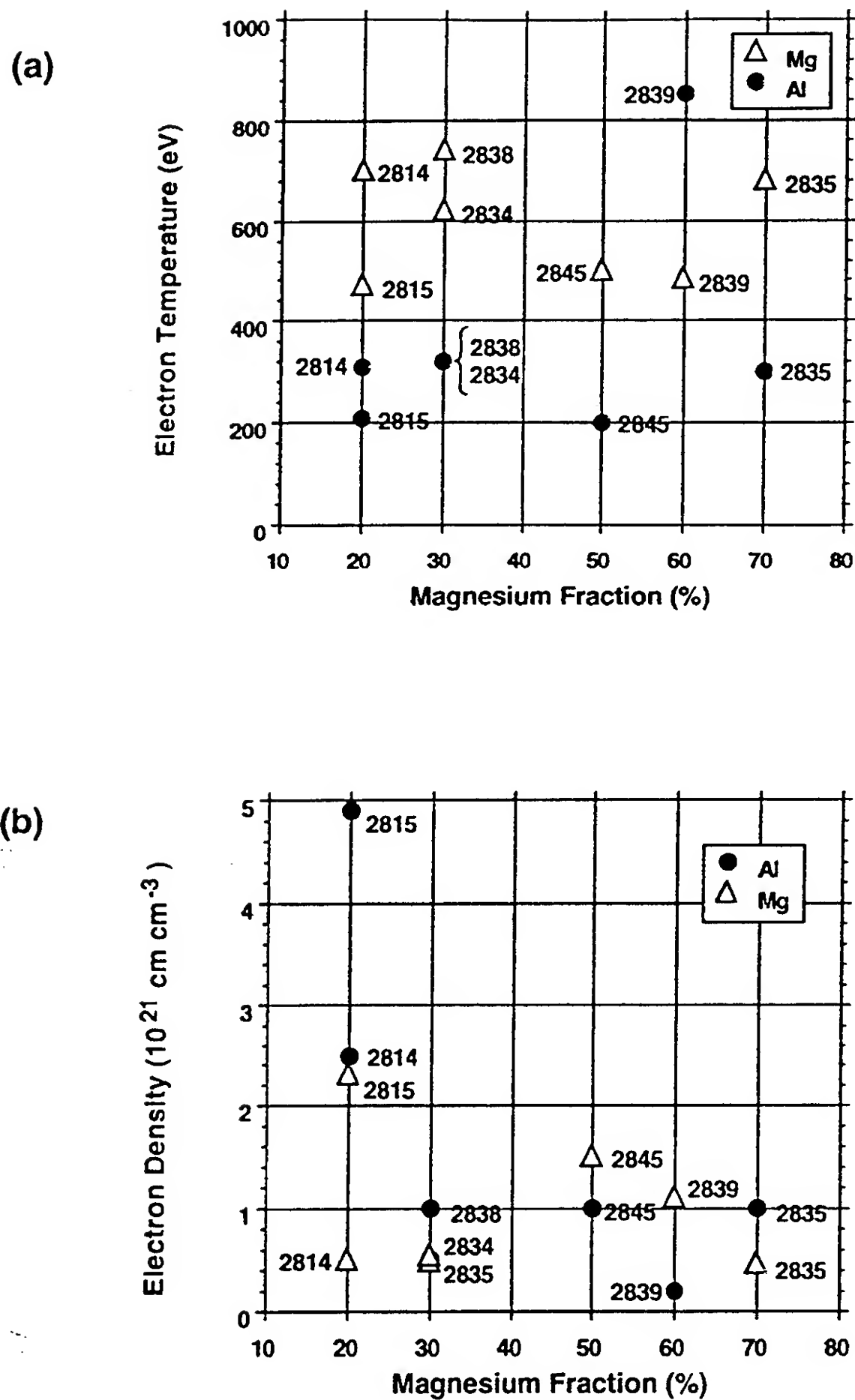


FIG. 2. The measured ratio of the magnesium line energy to the total line energy versus magnesium fraction.



**FIG. 3.** The measured (a) electron temperature and (b) electron density from all the aluminum-magnesium wire arrays. Notice, the electron temperatures deduced from the magnesium lines are higher than those inferred from the aluminum lines although the electron densities are generally lower. This is an indication that the plasmas are not uniformly mixed.



## II. INCREASING X-RAY EMISSION IN PRS LOADS THROUGH COMPARISONS OF THEORY WITH EXPERIMENT

### A. Recent History

The comparison of predicted K-shell yield behavior in aluminum with experimental results from three different pulse-power generators,<sup>1</sup> has provided several useful insights into the multifaceted dynamics of imploding wire z-pinches and into how this dynamics impacts x-ray production. They have also helped to define some of the areas where more research and more careful theoretical/experimental comparisons are needed, and they have suggested ways to increase x-ray yields from PRS loads.

As noted in Ref (1), there are roughly four discernible phases to experimental wire-array dynamics. There is an explosion phase, in which the initiation of the pulse-power discharge creates plasma by exploding the wires in the array. An implosion phase follows during which  $\mathbf{j} \times \mathbf{B}$  forces accelerate plasma toward the axis. In a third (thermalization) phase, the kinetic energy generated during implosion is converted rapidly to thermal energy when the plasma assembles on axis. At this time, the plasma ionizes into high lying (K-shell) ionization stages, and the emission of an intense kilovolt x-ray pulse begins. It continues into a fourth, heating and compression, phase provided sufficient current continues to flow in the plasma.

There are theoretical uncertainties about both the nature of the dynamics in each of these phases and the degree to which they overlap and influence each other. It is often convenient to ignore overlaps and to model the different phases separately. X-ray emission occurs during phases two through four. It was studied theoretically several years ago for phases two and three using a series of one dimensional (1-D) radiative magneto-hydrodynamics (MHD) calculations of aluminum wire-array implosions.<sup>2,3</sup> In these calculations, the thermalization behavior of the plasma on axis was investigated under idealized plasma initial conditions. Initially uniform and cool shells ( $\cong 15$  eV) of plasma that were located, on average, at a radius of 1 cm were accelerated by a prescribed linearly rising current. The current was terminated prior to plasma assembly when the outer radius of the implosion reached 1.4 mm in approximate conformity with experimentally observed z-pinch radii on axis. The calculations followed the plasma dynamics through thermalization with the total current set to zero so that there was no phase four to the dynamics. During phase three, a pulse of kilovolt x-rays was generated because the aluminum plasma was able to ionize rapidly into the K shell, i.e., into the hydrogen-like and helium-like ionization stages. In these early calculations, the implosions well approximated those of a slug model and energy input was predominantly kinetic. They predicted the K-shell yield of aluminum as a function of the initial wire array mass and of the energy imparted to each ion during the implosion.

The first comparisons of these predictions with experimental measurements were carried out at Physics International Inc. (PI) on their Double Eagle facility. They revealed three differences with the calculations.<sup>4</sup> One, more than kinetic energy was contributing to the kilovolt emission. Two, emissions from the core of the plasma played a more important role in the experiments than in the calculations. And three, the ion densities on axis that were inferred from experimental x-ray data were two or more orders of magnitude smaller than the ion densities that had been calculated.

Other issues were suggested when the yield behavior of aluminum was later investigated at Sandia National Laboratories (SNL) on their Saturn facility and at the Phoenix facility of the Naval Surface Warfare Center (NSWC). An analysis of the Saturn and Double Eagle circuits and their respective K-shell yield data suggested there was a much greater overlap of the phase one and two dynamics on Saturn than on Double Eagle and that this overlap had had a deleterious effect on the Saturn yields.<sup>5</sup> The yield behavior also suggested that there was less post-implosion energy input to the pinch in Saturn than in Double Eagle because the Saturn implosions occurred later in the current pulse than the Double Eagle implosions.<sup>1</sup>

These discrepancies between predicted and measured yields led to a reexamination of the calculations and experiments and of the issues that need to be addressed in making these comparisons. It was found<sup>6</sup> phenomenologically, for example, that by an ad hoc increase of the magnitudes of the plasma viscosity, heat conductivity, and electrical resistivity, it was possible to find a set of multipliers to these quantities that produced approximately the same calculated ion densities, electron temperatures, and K-shell yields on axis as had been seen experimentally. One possible explanation for this result is that subgrid-scale corrections to the magnetic resistivity, thermal diffusivity, and viscosity are needed in 1-D MHD simulations.<sup>7</sup> They change the way energy is delivered to the plasma, and these changes are dependent on the initial conditions of the calculations, i.e., different amounts of compressional heating, ohmic heating, and kinetic energy are generated depending on the initial distribution of plasma.

The calculations described in Ref. (6), which we denote as "soft-implosion" calculations, achieve three objectives. One, they predict K-shell yields (see Fig. (6)) that are quantitatively similar to those that were originally predicted by the hard-implosion calculations of Ref. (2) (see Figs. (6) and (7)). The calculated yields are also less than the largest of the measured yields (as expected since the current is terminated prematurely in the calculations). Two, they predict longer x-ray pulsewidths and smaller x-ray powers than hard-implosion calculations do, and the soft-implosion powers are in general agreement with experiment. Three, and also in accord with experiment, ion densities on axis are two or more orders of magnitude smaller than those predicted by the hard-implosion calculations. By taking the multipliers to the artificial viscosity, heat conductivity, and electrical resistivity to be independent of z-pinch conditions, we are able to derive yield contours, as we shall see shortly, that provide an alternative perspective to the yield contours derived in Ref. (2).

The important point is that, when comparing z-pinch calculations (whether hard or soft implosion calculations) with experiment, it must be known when assumptions about the initial and subsequent conditions of the pinch dynamics are being made that are not borne out by the experiments. Otherwise, erroneous conclusions about x-ray yield scaling can and will be drawn. For example, all 1-D MHD calculations assume that the plasma is initially cylindrically symmetric and tightly concentrated near the radius of the initial array. They further assume that current flows through the plasma with cylindrical symmetry,<sup>8</sup> that the  $\mathbf{j} \times \mathbf{B}$  forces act with the same symmetry on all of the mass, and that the implosion maintains its symmetry and stability on average throughout the implosion. These assumptions can be seriously violated in the experiments, making comparisons heuristic at best. When they are violated, they have serious negative consequences on x-ray output.

One should conclude, therefore, that while z-pinch theory is needed both to guide experiments

and to interpret experimental findings, z-pinch experiments are needed to define the initial conditions and assumptions under which different theoretical calculations are carried out. In this section, comparisons of several facets of z-pinch theory and experiment are made with this point of view in mind. First, we will indicate how the "hard implosion" yield predictions that were made in Ref. (2) are changed when the enhancements to the electrical resistivity, heat conductivity, and viscosity of Ref. (6) are employed to soften the implosion, i.e., to reduce the ion densities that are attained on axis. These new "soft implosion" yield predictions and the analysis that was used to obtain them suggest a correlation between the load/generator coupling and the x-ray emission that takes place, which needs to be investigated experimentally. Next, two new sets of Double Eagle and Phoenix aluminum experiments are briefly described. They were designed to increase x-ray yields and to provide additional information about the dependence of K-shell yields on load mass and generator coupling. The Phoenix experiments are yet to be carried out, and only a subset of the Double Eagle experiments were performed this year, but with remarkably good results. A comparison of these results is then made to some new and old theoretical data. The Double Eagle data, old and new, together show that compressional heating may be an important component of wire array dynamics, while the theoretical data show that compressional heating significantly alters the yield behavior. Finally, the theoretical significance of these comparisons is discussed.

## B. Soft Implosion Yield Scaling

In equilibrium, a plasma must contain a minimum amount of energy,  $E_{min}$ , per ion in order to radiate from the K shell.<sup>2</sup> From a dynamics point of view, this energy must be delivered to and stored in the plasma before disassembly, and it must be supplied rapidly so that it is not dissipated or radiated away while the plasma is being heated. The thermalization of implosion kinetic energy during z-pinch assembly has been under investigation as the most promising mechanism for generating thermal energy in a pinch fast enough to fulfill this power requirement. However, it is not always the case that  $\mathbf{j} \times \mathbf{B}$  forces generate kinetic energy exclusively during implosion. Varying amounts of kinetic energy will be generated depending on the amount of inner (core) plasma that the outer (shell) plasma implodes upon and, therefore, on the amount of back-pressure that opposes the implosion.

Recent pinch experiments at PI, using aluminum wires coated with various amounts of magnesium,<sup>9</sup> have shown that sparse wire arrays do not implode as 0-D slug models predict;<sup>10</sup> namely, the entire wire mass does not implode with the same accelerations and velocities. Rather, magnesium plasma was observed to blow off first and to be driven in by  $\mathbf{j} \times \mathbf{B}$  forces in advance of the aluminum plasma. A core of magnesium plasma forms surrounded by a shell of lower temperature aluminum plasma. In this instance, compressional heating can be expected to play an important role in the phase two dynamics of aluminum in addition to kinetic energy generation.

An initial effort to quantify the effects that a fixed percentage of compressional heating during phase two has on the phase three dynamics is described in this subsection. A series of 1-D MHD calculations were made. They are identical in all but two ways to the calculations of Refs. (2) and (3) described above. First of all, in these calculations, multiplicative factors of 30, 40, and 20 were employed for the heat conductivity, artificial viscosity, and electrical resistivity respectively<sup>6</sup> in order to soften the implosions on axis. Secondly, roughly 20% of the total load mass was located in the core of the plasma as opposed to 8% in the previous calculations. The core was defined as the innermost seven of the fifteen cells used in the calculations. Each core cell contained 1/2 the

mass of the next outer cell, and the seventh core cell, adjoining the plasma shell, had the same mass as each cell within the shell.

Because of the enhanced conductivity, viscosity, and resistivity and because of the larger ratio of core to shell plasma, the kinetic energy generated during implosion in these calculations was only two-thirds of the total energy coupled to the plasma by the current prior to its termination. As before, calculations were carried out in which different amounts of load mass received given amounts of input of energy,  $E_{inp}$ , per ion, defined by a dimensionless parameter,<sup>11</sup>  $\eta^* \equiv E_{inp}/E_{min}$ . In the calculations of Refs. (2) and (3), more than 95% of the energy delivered to the plasma was kinetic, and the dimensionless energy per ion,  $\eta \equiv K_i/E_{min}$ , was used to define them. In the present calculations, the criterion,  $\eta > 1$ , for bulk plasma K-shell emission translates into the criterion,  $\eta^* > 1.5$ .

An example of the K-shell yield behavior found for soft implosions is shown in Fig. (1). The yields are for aluminum, and they are plotted as a function of load mass,  $m$ , for a fixed value of  $\eta^* = 6$ . Two different power law fits to the calculated data points are drawn in this figure. The two dashed lines are least squares fits of the form used in the previous analysis (Refs. (2) and (6)). The data are fitted to the curve,

$$y_K = a(\eta^*)m^2,$$

for small mass loads. For large masses, they are fitted to

$$y_K = b(\eta^*)m.$$

The two curves intersect at a point, denoted the mass breakpoint, which depends on  $\eta^*$ :

$$m = m_{BP}(\eta^*) = b/a.$$

A more accurate fitting procedure can be employed, however, that utilizes three power law least squares fits. It is represented by the solid lines in Fig. (1). In each segment, the yield data is approximated by

$$y_K = a_i(\eta^*)m^{\alpha_i(\eta^*)} \quad i = 1, 2, 3,$$

In this approximation, both the coefficient and the exponent are functions of  $\eta^*$ . The intersection of these curves now defines two breakpoints given by:

$$m = m_1(\eta^*) = a_1^{1/(\alpha_2 - \alpha_1)} a_2^{1/(\alpha_1 - \alpha_2)}$$

and

$$m = m_2(\eta^*) = a_2^{1/(\alpha_3 - \alpha_2)} a_3^{1/(\alpha_2 - \alpha_3)}.$$

In Fig. (1),  $\alpha_1 \cong 2$ ,  $\alpha_2 \cong 1.4$ , and  $\alpha_3 \cong 0.45$ , i.e., in this case, the yield more accurately scales sublinearly with mass for large masses  $< 10$  mg/cm.

These two scaling approximations make very different predictions about the efficiency,  $e_K$ , of converting input energy to a z-pinch into K-shell x-rays. This difference is conveniently represented in  $m - v_f$  space, where  $v_f$  is the maximum implosion velocity achievable if all of the input energy per ion were kinetic:  $(1/2)m_i v_f^2 \equiv E_{inp}$ , where  $m_i$  is the mass of an aluminum ion. In the



calculations of Ref. (2),  $e_K$  was found to be larger than 30% throughout the region defined by  $\eta > 1$  and  $m > m_{BP}$ . This is the defining feature of the shaded region depicted in Fig. (2). A somewhat different picture of  $e_K$  behavior is predicted by the  $\eta^*$  set of soft implosion yield data. For each value of  $\eta^*$  lying in the interval,  $1.5 \leq \eta^* \leq 10$ , three power law least squares fits can be made similar to those shown in Fig. (1). They produce the conversion efficiency contours shown in Fig. (3), which are drawn relative to the breakpoint curves,  $m_1$  and  $m_2$ .

The above analysis shows there will be no unique way to approximate the behavior of experimental yields unless more is known about the conditions under which the experimental plasmas evolve or unless more is done to control these conditions. Reliable x-ray diagnostics will need to be developed in order to infer the core plasma conditions that are generated on axis in addition to surface conditions. These inferences would provide valuable ways to benchmark code calculations by providing data on the relative amounts of core and shell plasma and, therefore, on the relative amounts of compression heating and kinetic energy generation.

### C. Theory/Experiment Comparisons

Several correlations were found in Ref. (1) between the measured and predicted K-shell yields. On Double Eagle, the high efficiencies for converting kinetic energy to kilovolt x rays correlated with the early assembly of the plasmas relative to the time to peak current in a short-circuit load. On Phoenix and Saturn, the increase or decrease in yield with  $v_f$  for fixed  $m$  appeared to be correlated with the size of  $m$  relative to  $m_{BP}(\eta)$ , i.e., when  $m > m_{BP}$ , the yield increased; otherwise, it decreased. However, considerably more data is needed to confirm this behavior.

The recent experimental findings with magnesium coated aluminum wire loads<sup>9</sup> discussed in Sec. I suggest a possible explanation for the Double Eagle results. If the outer surfaces of the wires are driven to the axis in advance of the wire core, then these implosions differ markedly from those of a thin, essentially hollow, plasma shell, which the calculations of Ref. (2) assume. The implosions might be expected to behave more like those of the calculations described above, in which a non-negligible amount of energy goes into compressional heating. Alternatively, it is speculated that a significant amount of energy is delivered to the plasma through anomalous Ohmic heating during the phase three dynamics. This effect is not, as yet, modeled by the calculations. In order to assess these alternatives, a new set of Double Eagle aluminum experiments were planned this year. The shot matrix for these experiments is presented in Table I. As in the earlier Double Eagle, Saturn, and Phoenix experiments, the length of the arrays chosen for these new experiments was 2 cm.

There are several differences between these and the previous Double Eagle experiments.<sup>4</sup> First of all, larger diameter arrays are used in the new experiments, and they are composed of a larger number of smaller diameter wires than were used before. Hence, implosion times are longer than before and more kinetic energy will be generated. By design, the implosion times in the new experiments have a relation to the peak of the short-circuit current profile of Double Eagle that is similar to the relation between these quantities in the Phoenix experiments of Ref. (1). Consequently, it was anticipated that their yield behavior would be similar to that observed on Phoenix barring the presence of any implosion asymmetries that might be introduced into the Double Eagle experiments by the large initial array diameters and by the long implosion paths. In other words, it was speculated in Ref. (1) that Double Eagle produced much higher conversion

**Table I. Double Eagle Al PRS Experiments**

Shot #	Wire Diam (mil)	Wire #	Wire Mass ( $\mu\text{g/cm}$ )	Array Diam (mm)	$\eta$	K.E. kJ
1.	0.7	18	121	40	7.6	79
2.	1.0	18	246	25.5	2.8	58
3.	1.5	24	739	16.5	0.75	44
4.	1.5	24	739	24	1.0	64.5
5.	1.2	24	473	18.5	1.2	46.5
6.	1.0	18	246	35	3.75	77
7.	1.2	24	473	30	1.8	73
8.	1.0	24	328	22	1.9	52
9.	1.0	24	328	36.5	2.85	80
10.	0.8	24	210	27.5	3.4	61
11.	0.8	24	210	41	4.7	85
12.	0.7	24	161	31.5	4.75	66
13.	0.7	24	161	38	5.7	80
14.	0.6	24	118	37	7.1	71.5

efficiencies than Phoenix because the implosions had occurred much earlier in the current pulse on Double Eagle than on Phoenix and that a much larger input of energy during the phase three dynamics had occurred in the earlier Double Eagle experiments than on Phoenix.

A similar set of experiments, designed to locate the mass breakpoint curve, was planned for Phoenix. In this case, a different strategy for fixing the mass-per-unit-length,  $m$ , while varying  $\eta$  (i.e.,  $v_f$ ) is used. The same number of fixed-sized wires are mounted at the same array diameter and the length of the array is varied. As the length increases, the inductance of the load increases, and the coupling to the generator is reduced. This reduction, in turn, reduces the final implosion velocities that are achievable. The shot matrix for these experiments is presented in Table II.

The intent of these experiments is to probe near the predicted location of the mass breakpoint curve,  $m = m_{BP}(\eta^*)$ . Two of the experiments that were carried out earlier,<sup>1</sup> using 2 cm length wires, were selected as a baseline. One lay above the mass breakpoint curve, and one, adjacent to it. As the length of the array increases, therefore, the 2 cm length shot lying above the  $m = m_{BP}$  curve should approach it, while the shot lying next to this curve will move away, thereby decreasing the K-shell yield per cm. This behavior is illustrated in Fig. (4).

Several questions arose in Ref. (1) concerning the relationship of the measured yields to the different conditions that were present in each of the experiments. On Double Eagle, for example, much higher efficiencies for converting kinetic energy (or input energy) into kilovolt x rays were observed than on Saturn or Phoenix. This behavior appeared to be correlated to the early assemblies of the plasmas on axis in the Double Eagle experiments relative to the time to peak current into

**Table II. Phoenix Al PRS Experiments**

Shot #	Wire Diam (mil)	Wire #	Wire Mass ( $\mu\text{g/cm}$ )	Array Diam (mm)	Array Length (cm)
1.	0.8	16	140	22	2.0
2.	0.8	16	140	22	2.5
3.	0.8	16	140	22	3.0
4.	0.8	16	140	22	3.5
5.	0.8	16	140	22	4.0
6.	0.8	16	140	22	5.0
7.	0.8	16	140	22	6.0
8.	0.8	16	140	22	7.0
9.	0.7	16	107	26	2.0
10.	0.7	16	107	26	3.0
11.	0.7	16	107	26	4.0
12.	0.7	16	107	26	5.0
13.	0.7	16	107	26	6.0
14.	0.7	16	107	26	7.0

a short-circuit load. On Saturn, on the other hand, conversion efficiencies were much lower than expected, and this behavior appeared to be correlated to the short current risetime of Saturn and to the large load masses and large diameter wires that were used in the experiments. Whether or not these differences in Double Eagle and Saturn experimental conditions are responsible for the differences in yield behavior is unclear. Other influences may be involved, such as those observed in the recent experiments with magnesium coated aluminum wire loads<sup>9</sup> that were discussed in Section I.

Because of resource limitations, only 6 of the Double Eagle experiments in Table I and none of the Phoenix experiments in Table II could be conducted this year. The shot matrix for the six experiments that were undertaken is shown in Table III.

There are several important differences between these and the previous Double Eagle experiments,<sup>4</sup> which are listed in Table IV. First of all as mentioned above, larger diameter arrays were used in the Table III experiments, and these arrays were composed of a larger number of smaller diameter wires than were used before. Hence, implosion times were longer and more kinetic energy was generated in the Table III shots than in the Table IV shots. In addition, the driving voltage in the new experiments was 10% greater than the voltage that was used to drive the Table IV experiments, which also resulted in a larger input of energy than would have been present otherwise. By design, therefore, they were made to more closely resemble the Phoenix experiments described in Ref. (1). In other words, the x-ray conversion efficiencies of the Table III experiments were expected to be more like those observed in the Phoenix experiments than those



**Table III. New Double Eagle Al Z-pinch Experiments**

Wire Diam (mil)	Array Mass ( $\mu\text{g/cm}$ )	Array Diam (cm)	$\eta$	Number of wires	Kinetic Energy (kJ)	K-shell Yield (kJ)	Conversion Efficiency (%)
0.7	161	3.8	5.7	24	80	31.7	40
0.7	161	3.2	4.75	24	66	34.4	52
0.8	210	4.0	4.7	24	85	31.3	37
0.8	210	2.75	3.4	24	61	40.0	66
1.0	246	2.55	2.8	18	58	55.4	95.5
1.0	328	2.2	1.9	24	52	42.2	81

observed in the Table IV experiments.

**Table IV. Old Double Eagle Al Z-pinch Experiments**

Wire Diam (mil)	Array Mass ( $\mu\text{g/cm}$ )	Array Diam (cm)	$\eta$	Number of wires	Kinetic Energy (kJ)	K-shell Yield (kJ)	Conversion Efficiency (%)
0.7	80	2.5	6.2	12	43	7.5	17
0.8	105	2.0	3.7	12	33.5	21	63
1.0	164	1.5	1.9	12	27	26	96
1.3	277	1.25	1.1	12	26	30	115
1.7	474	0.9	0.42	12	17	10	59

However, this expectation was not fulfilled. The yields in the new Double Eagle experiments, which are displayed in Fig. (5) as a function of the initial array diameter, were not limited by the shift in the implosion time relative to the current pulse, even though implosion asymmetries were more likely in these experiments by virtue of the generally larger initial array diameters and the longer implosion paths than were present in the Phoenix experiments. Double Eagle achieved roughly the same high conversion efficiencies of (effective) kinetic energy into K-shell emissions in the new experiments as had been achieved in the old. In both sets of experiments, much larger efficiencies occurred than in either the Phoenix or Saturn experiments. Note in Fig. (5) that two experiments were conducted and two yield measurements made for each of the Table III shots.<sup>12</sup> Because z-pinch experiments can fail or degrade for many reasons, only the highest of the two measured yields was listed in Table III. The x-ray conversion efficiencies in Table III are ratios of the maximum measured yields to the (0-D) computed kinetic energies, which are also listed in Table III. Each of these conversion efficiencies is significantly larger than the ones that were

inferred in the Phoenix and Saturn experiments.

Figures (6) and (7) provide comparisons in  $m - v_f$  space of the measured yields listed in Tables III and IV to the predicted hard- and soft-implosion yields respectively. Each shot in Tables III and IV is represented by a point in this space, and the yields per centimeter for the shots are listed next to each point. Yield contours in these figures were computed from the current-off calculations described above in this section and in Refs. (2) and (3). Note, there is qualitative agreement between the calculated yield contours and the experimental yields. Both trend upwards in roughly the same proportion as the load mass trends upwards. The new Double Eagle experiments, denoted by circles, tend to track the 10 kJ/cm contours for both the hard- and the soft-implosion calculations. The old experiments, on the other hand, denoted by triangles, follow the 3 kJ/cm contour for the soft implosions, but follow the 5 kJ/cm contour only in the efficient emission region of the hard implosions. Generally, a greater fall-off in yield is predicted at high  $\eta$  for hard than for soft implosions.<sup>11</sup>

As seen in Fig. (5), the two sets of Double Eagle experiments are qualitatively similar in another respect. Both exhibit a maximum in yield as a function of array diameter. The locations of these maxima are apparently dependent on the average amount of kinetic energy that is imparted to the loads in these similar sets of experiments. Each yield maximum is associated with a corresponding maximum in the x-ray conversion efficiency. At low energy, the maximum occurred at the  $\eta = 1$  boundary, and it shifted to higher  $\eta$  as the energy input was increased. In contrast to the Saturn and Phoenix data, however, yields in both these Double Eagle experiments reached maxima significantly below the  $m = m_{BP}(\eta)$  boundary, where  $m^2$  to  $m$  scaling theory predicts that they would be. One might conjecture that this yield behavior is an artifact of the large diameter experiments, for, as one increases the diameter of an array, one also increases the effect of asymmetries, which occur because of differences in the  $\mathbf{j} \times \mathbf{B}$  forces that act on the wires. Asymmetries are expected to soften the implosion and lower the x-ray emission. This effect is apparent in the two  $\eta \cong 5.1$  and  $\eta \cong 4.8$  shots. The larger, 210  $\mu\text{g/cm}$ , load should have produced a larger yield than the 161  $\mu\text{g/cm}$  load. However, it had a larger initial array diameter and produced a smaller measured yield than the 161  $\mu\text{g/cm}$  implosion. The effect of implosion asymmetry on plasma assembly and x-ray emission will be tested in the near future at Double Eagle by staggering the initial locations of the wires relative to the return current posts in order to compensate for and offset the otherwise unequal  $\mathbf{j} \times \mathbf{B}$  forces that can act on circular arrays of wires. Further analysis of time-resolved pinhole images from the present shot matrix will also allow us to quantify the role of implosion asymmetries.

Two qualitative differences between the yield curves in Figs. (6) and (7) should be noted. At low  $\eta$ , the soft-implosion yield contours fall away towards larger mass more rapidly than the hard-implosion contours do, while the reverse is true at high  $\eta$  ( $\eta > 5$ ). Because of this behavior, soft-implosion modeling appears not to predict the high  $\eta$  data as well as hard-implosion modeling does, while the reverse is true at low  $\eta$ . At issue in these two cases is the rate at which a given mass of plasma can be totally ionized at high  $\eta$  or the degree to which it can be imploded as a shell at low  $\eta$ .

#### D. Summary and Conclusions

By taking the multipliers to the artificial viscosity, heat conductivity, and electrical resistivity to be independent of z-pinch conditions, we were able to derive the yield contours shown in Fig. (7).

However, these contours were calculated at the loss of the mass breakpoint curve that connects  $m^2$  with  $m$  scaling, and this curve was a central feature of the experimental/theoretical comparisons that were made in Ref. (1). The K-shell yields that were measured in both the Saturn and Phoenix experiments reached their peak values when  $m = m_{BP}$ . The location of  $m_{BP}$  as a function of  $\eta$  (or  $\eta^*$ ) was determined in Refs. (2) and (3) from a hybrid use of both hard- and soft-implosion calculations. In this paper, however, we indicated that a better fit to the calculated soft-implosion yields could be obtained by using three power law curves rather than the two,  $m^2$  and  $m$ , power laws.

For a fixed  $\eta > 1$ , the kinetic energy input scales with  $m$  in slug model implosions; thus, x-ray yields will scale linearly with mass if and only if a pinch is capable of efficiently converting kinetic energy into x rays and kinetic energy is the principal energy input. In soft-implosion calculations, where the current is terminated early in the phase three dynamics, efficient conversion is a limited capability as Fig. (3) indicates. This limitation was not evident in hard-implosion calculations (see Fig. (2)), nor might it be present in large mass experiments if the current were able to maintain plasma confinement on axis and continue to effectively deliver energy to the plasma. In the present state of z-pinch theory and experiment, these remain open questions.

Tentatively, one could draw the following conclusions from the Double Eagle data. The fall-off in yield with  $\eta$  at low  $\eta > 1$  (also seen in the Saturn and Phoenix experiments<sup>1</sup>) may be due, in part, to the early presence of plasma on axis (as seen in the Double Eagle mixture experiments) and to the incomplete explosion of the wires. However, the latter reason is more important in the Saturn and Phoenix than in the Double Eagle experiments. When a plasma shell implodes on a plasma core, there is less kinetic energy generation, more compressional heating, and more core emission and surface absorption. The fall-off in yield seen at high  $\eta$  in the Double Eagle experiments may be due, in part, to unequal forces acting on the wires and to poor implosion symmetry. The high x-ray conversion efficiencies seen on Double Eagle are still unexplained, but are, no doubt, in part attributable to comparing current-off calculations with current-on experiments. However, the origin of these high conversion efficiencies is enigmatic, at the moment, because they have not been seen, as yet, on either Saturn or Phoenix. This observation might lead one to suspect that the origin is machine related (i.e., power flow or implosion time related) or that it is experimental design related (i.e., related to the choice of wire and diode parameters or related to how well the generator has been characterized). Hopefully, future, well characterized, experiments on Saturn, Phoenix, or other generators may help to clarify this issue.

## REFERENCES

1. K. G. Whitney, J. W. Thornhill, J. L. Giuliani, Jr., J. Davis, L. A. Miles, E. E. Nolting, V. L. Kenyon, W. A. Speicer, J. A. Draper, C. R. Parsons, P. Dang, R. B. Spielman, T. J. Nash, J. S. McGurn, L. E. Ruggles, C. Deeney, R. R. Prasad, and L. Warren, Phys. Rev. E **50**, 2166 (1994).
2. K. G. Whitney, J. W. Thornhill, J. P. Apruzese, and J. Davis, J. Appl. Phys. **67**, 1725 (1990).
3. J. W. Thornhill, K. G. Whitney, and J. Davis, J. Quant. Spectrosc. Radiat. Transfer **44**, 251 (1990).
4. C. Deeney, T. Nash, R. R. Prasad, L. Warren, K. G. Whitney, J. W. Thornhill, and M. C. Coulter, Phys. Rev. A **44**, 6762 (1991).

5. K. G. Whitney, J. W. Thornhill, R. B. Spielman, T. J. Nash, J. S. McGurn, L. E. Ruggles, and M. C. Coulter, in "Proceedings of the Third International Conference on Dense Z-pinches, London, 1993", edited by M. Haines and A. Knight, AIP Conference Proceedings 299, p. 429.
6. J. W. Thornhill, K. G. Whitney, C. Deeney, and P. D. LePell, *Phys. Plasmas* **1**, 321 (1994).
7. M. L. Theobald, P. A. Fox, and S. Sofia, *Phys. Plasmas* **1**, 3016 (1994).
8. D. H. Kalantar and D. A. Hammer, *Phys. Rev. Lett.* **71**, 3806 (1993).
9. C. Deeney, P. D. LePell, B. H. Failor, S. L. Wong, J. P. Apruzese, K. G. Whitney, J. W. Thornhill, J. Davis, E. Yadlowsky, R. Hazelton, T. Nash, and N. Loter, "Increased Kilovolt X-ray Yields from Z-pinches by Mixing Elements of Similar Atomic Numbers", submitted to *Phys. Rev. E*.
10. J. Katzenstein, *J. Appl. Phys.* **52**, 676 (1981).
11. K. G. Whitney, J. W. Thornhill, C. Deeney, P. D. LePell, and M. C. Coulter, "Proceedings of the 9th International Conference on High-Powered Particle Beams, Washington DC, 1992", edited by D. Mosher and G. Cooperstein, p. 2044. Copies may be ordered from NTIS, Springfield, VA, Document No. PB92-206168.
12. The total K-shell yields listed in Table III were not measured directly. The view of each of the two calorimeters that were used to measure the kilovolt emissions was obstructed, so that they saw only from 1/3 to 1/2 of the total, 2 cm length, pinch. The yields per cm were inferred from these measurements, and the total yield was obtained by multiplying the yields per cm by 2.

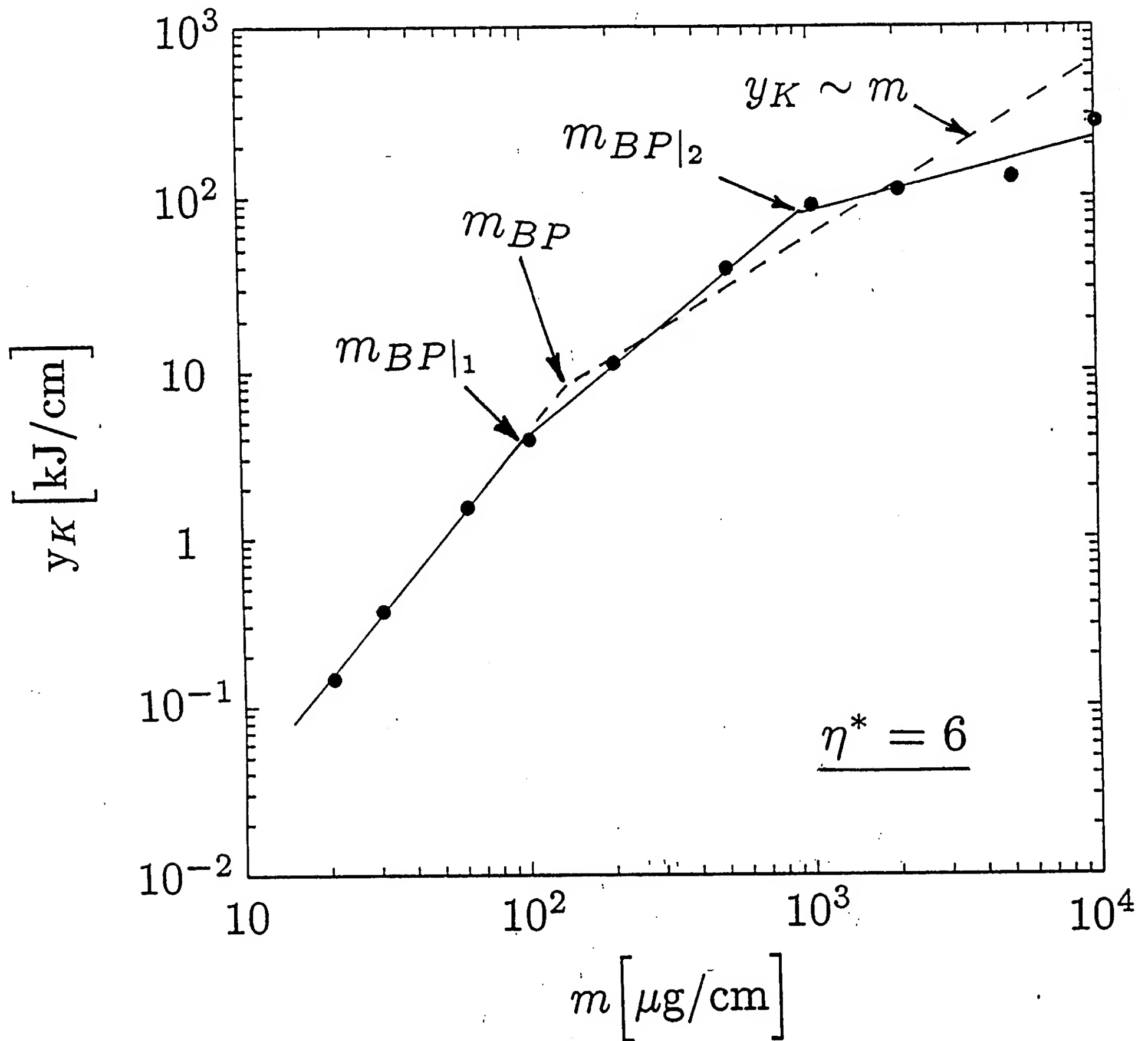


**Figure 1.** Two power law fits to ten calculated K-shell yields at  $\eta^* = 6$  are shown. The dashed curve represents an  $m^2$  to  $m$  curve fit. The solid curve is a more accurate fit obtained from the curves,  $3.33 \times 10^{-4} m^{2.04}$ ,  $7.76 \times 10^{-3} m^{1.36}$ , and  $3.96 m^{0.438}$ . The intersections of the power law curves define the mass breakpoints,  $m_{BP}$ ,  $m_{BP|1}$ , and  $m_{BP|2}$  as shown.

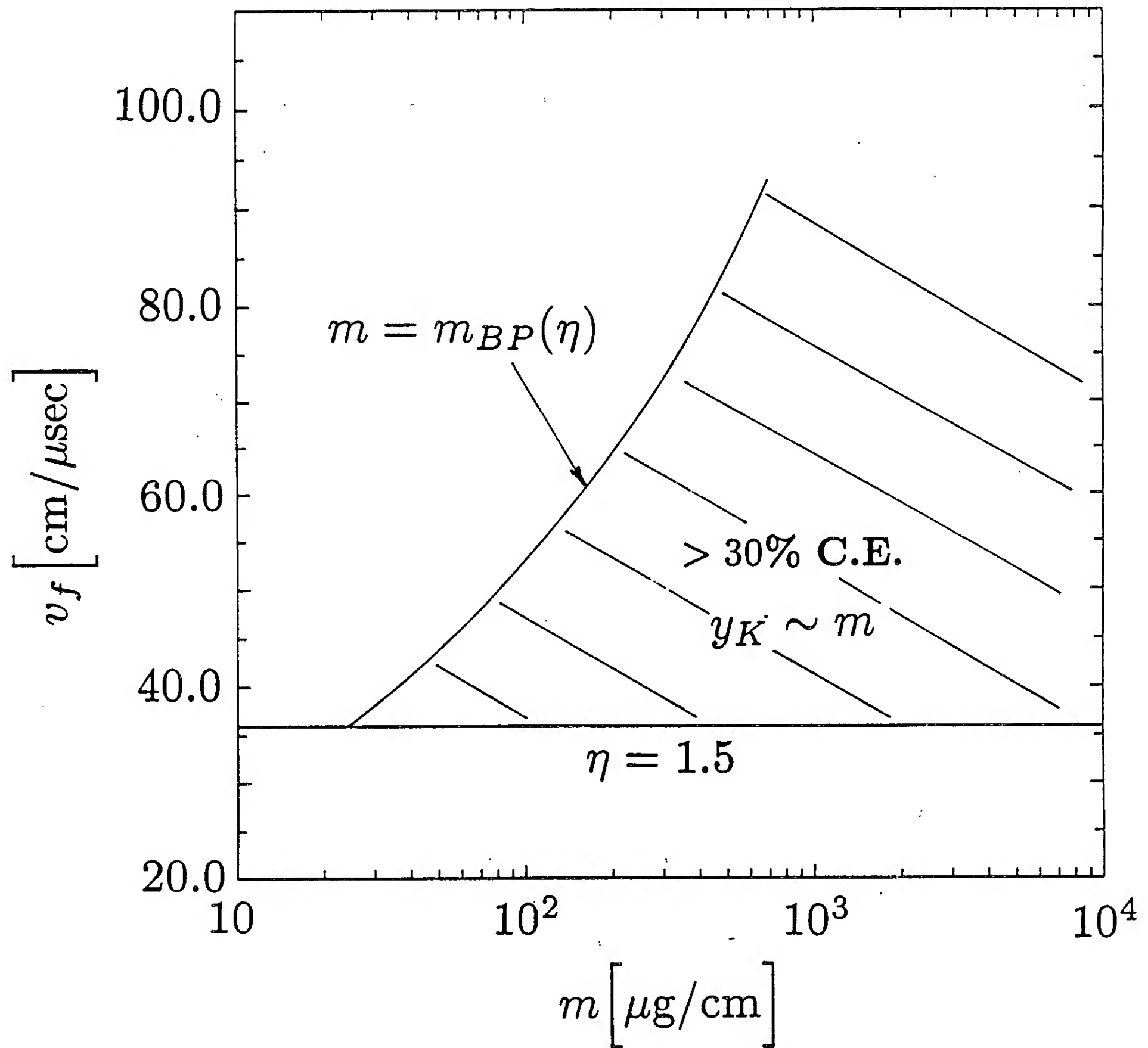


**Figure 2.** The mass breakpoint,  $m_{BP}$ , and the  $\eta = 1.5$  curves define a region in  $m - v_f$  space, drawn cross-hatched, where an efficient conversion of input energy into K-shell x rays in aluminum occurs. Conversion efficiencies greater than 30% are predicted.

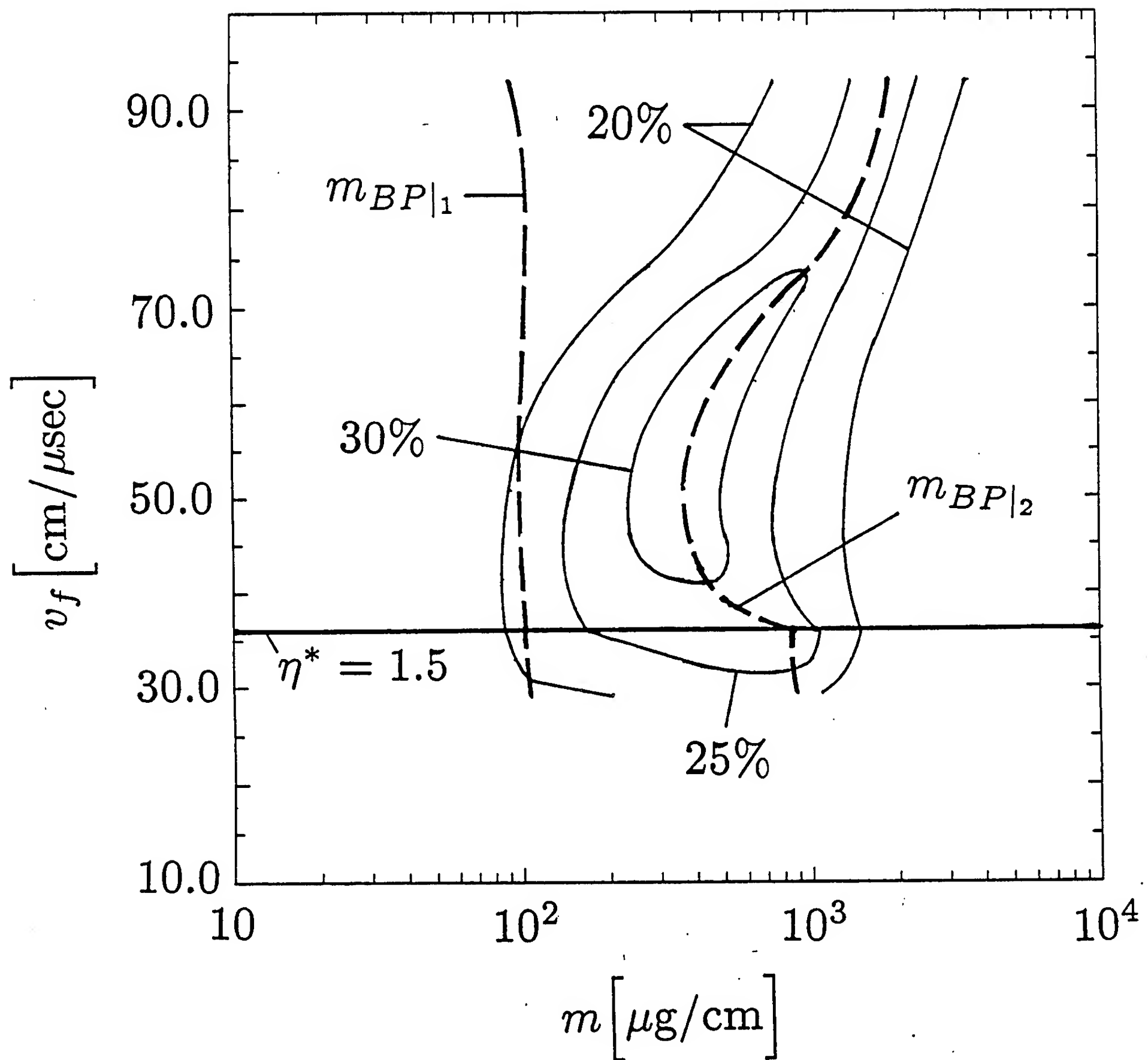


**Figure 3.** Conversion efficiency contours of input energy to K-shell x rays are drawn for a set of soft-implosion, current-off calculations. These contours are drawn relative to the mass breakpoint curves,  $m_{BP|1}$  and  $m_{BP|2}$ , and the  $\eta^* = 1.5$  curves.



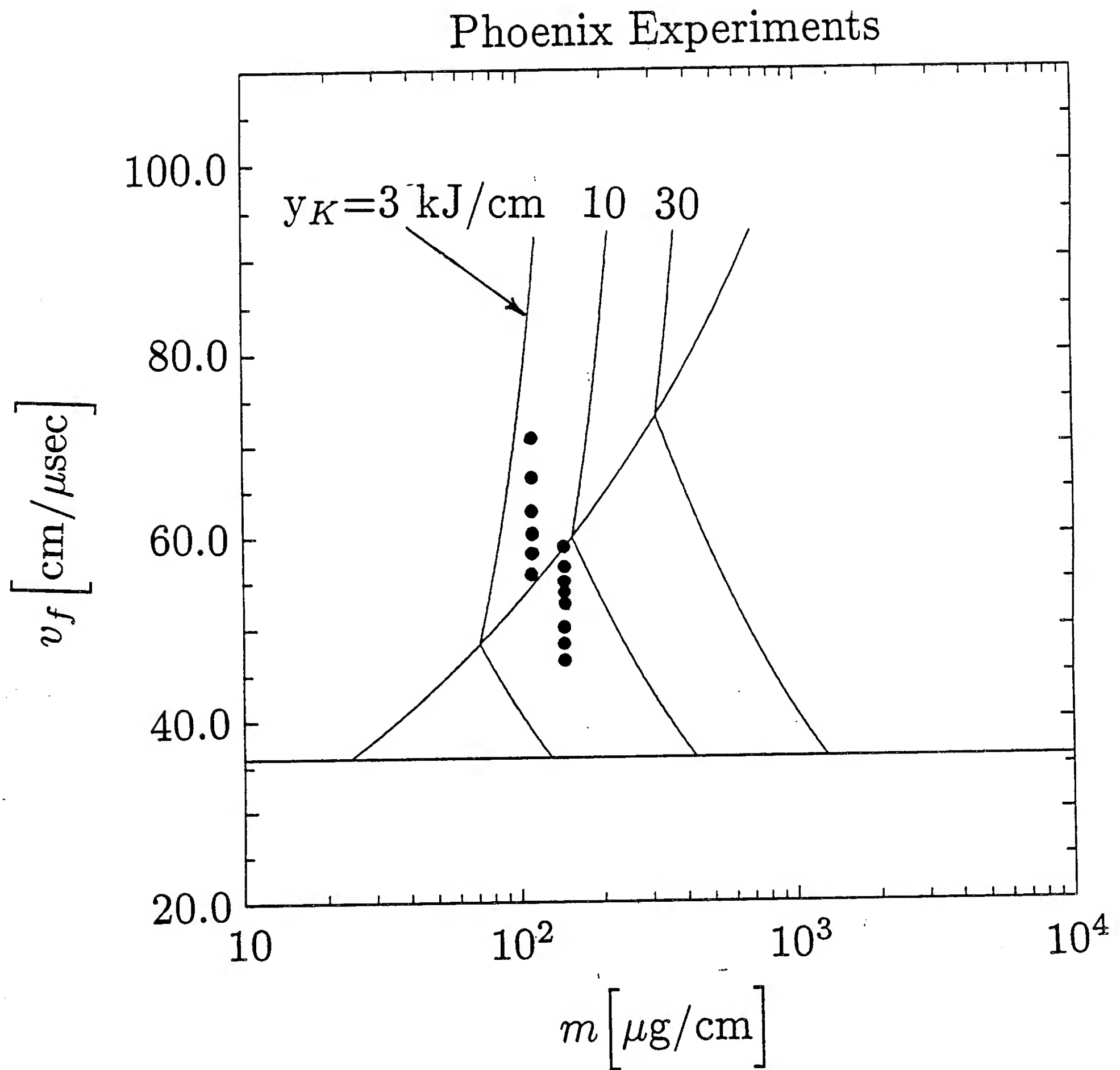


**Figure 4.** Each of the Phoenix aluminum experiments is located as a point in  $m - v_f$  space relative to the yield contours for  $m^2$  to  $m$  yield scaling.

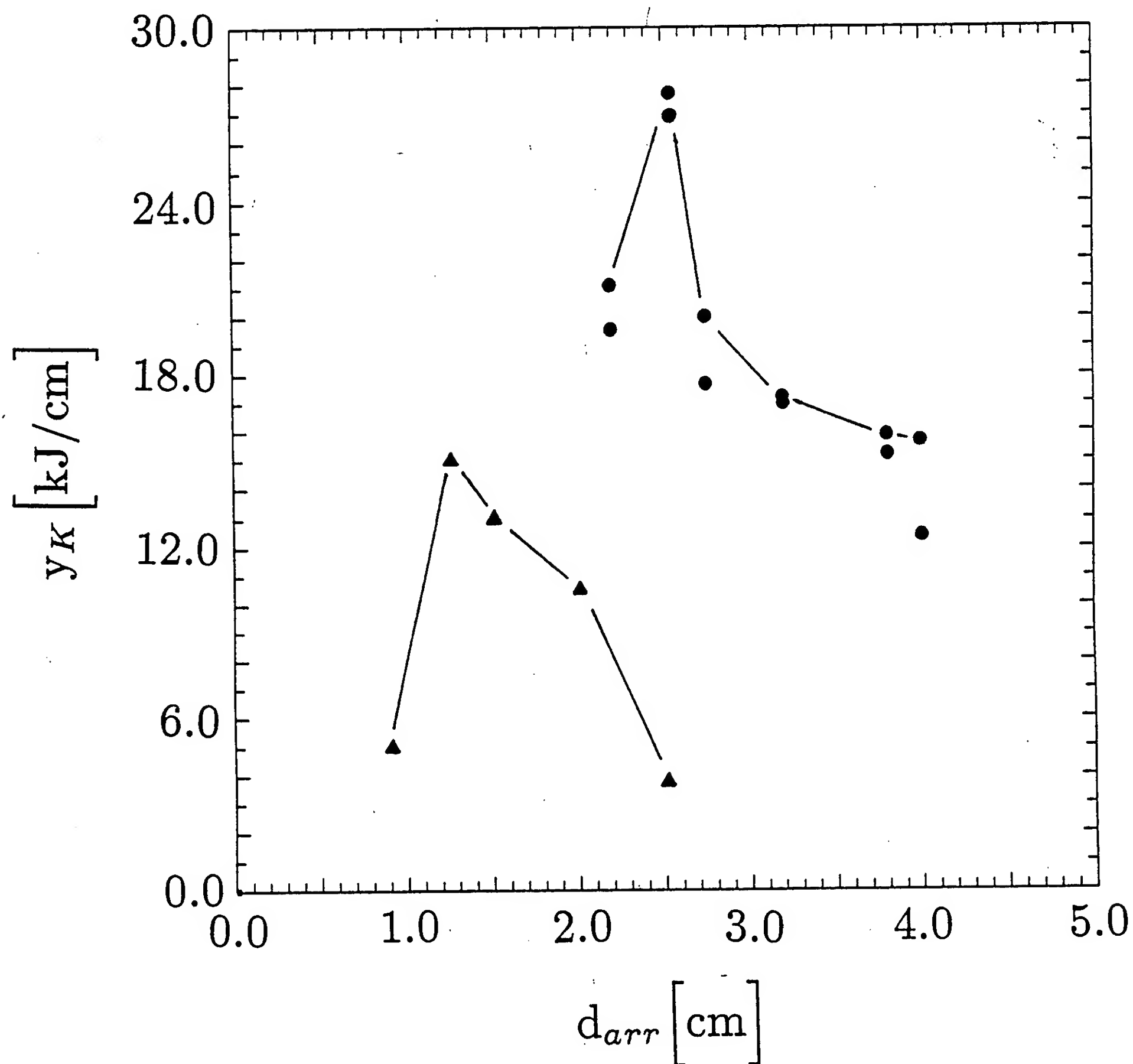


**Figure 5.** The K-shell yields per cm that were measured in two sets of Double Eagle aluminum experiments are plotted as a function of the initial array diameter. The triangles are the yields listed in Table II and the circles are the yields per cm that were measured in the Table I experiments. The largest of the two yields that were measured at each diameter are listed in Table I.

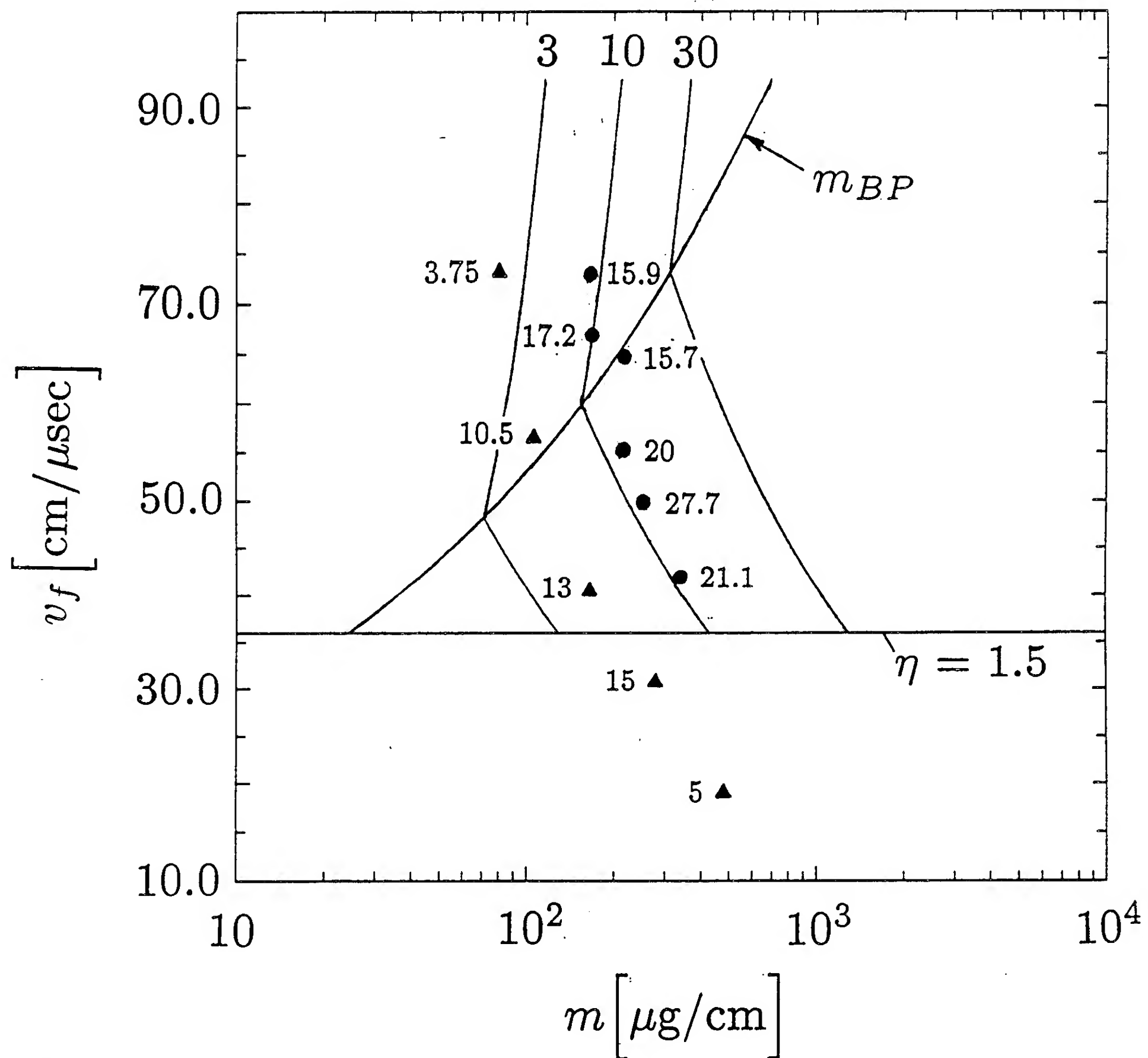


**Figure 6.** Each of the Double Eagle aluminum experiments is located as a point in  $m - v_f$  space relative to the yield contours for  $m^2$  to  $m$  yield scaling. The six circles locate the Table I experiments, and the five triangles, the Table II experiments. The numbers next to these points are the measured K-shell yields per cm. The yield contours of 3, 10, and 30 kJ/cm that are shown were calculated assuming a 35% x-ray conversion efficiency (see Ref. (2)).

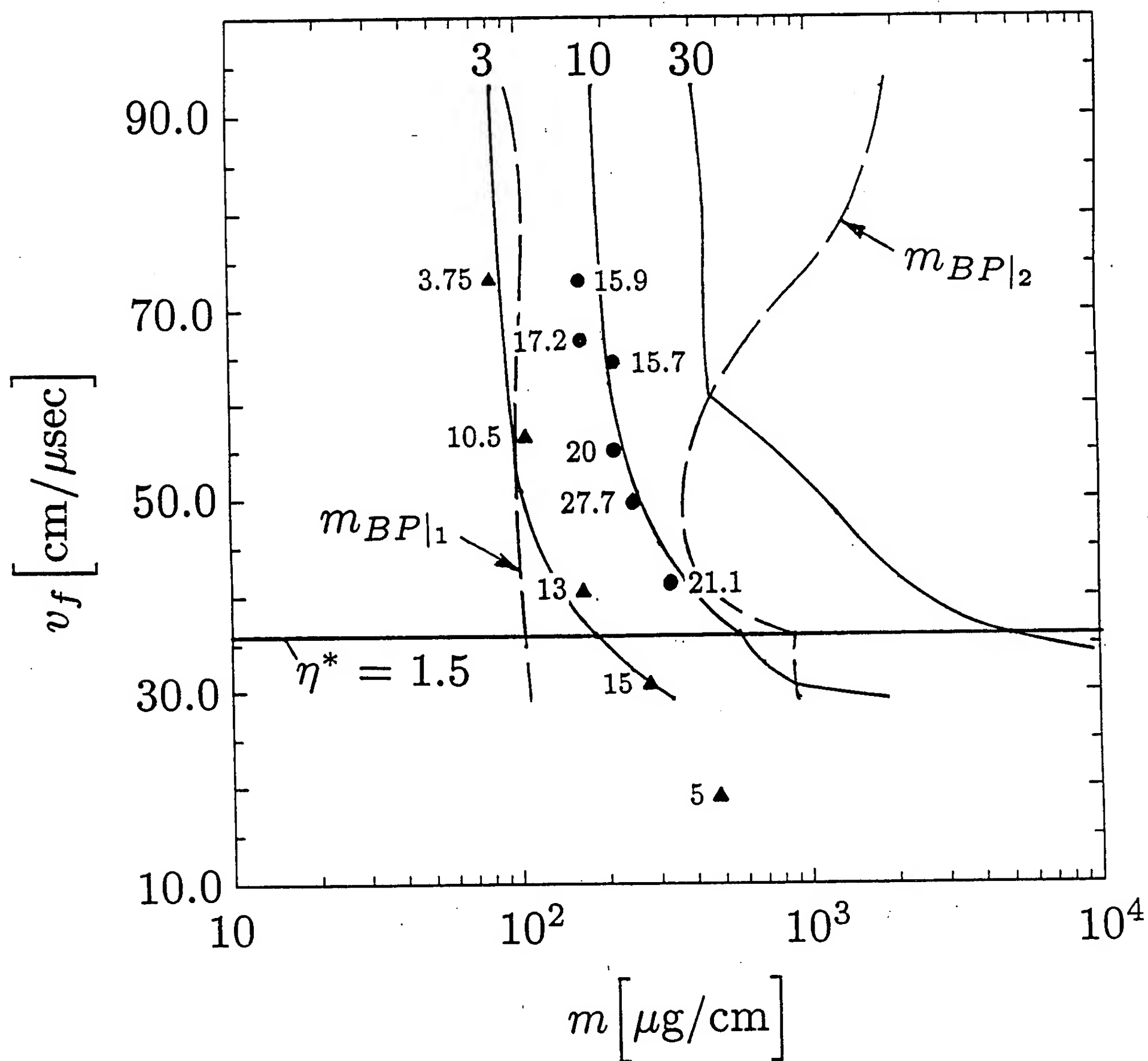


**Figure 7.** Each of the Double Eagle aluminum experiments is located in  $m - v_f$  space relative to yield contours that are derived from a set of soft-implosion calculations using six parameter power law fits. The six circles are the Table I experiments, and the five triangles, the Table II experiments. The numbers next to the triangles and circles are the measured K-shell yields per cm. The yield contours are for 3, 10, and 30 kJ/cm.

### III. IMPORTANT INFERENCES DERIVED FROM A THEORETICAL DATA ANALYSIS OF THE SATURN ALUMINUM PRS EXPERIMENTS

In this section, we briefly summarize the analysis of data from a set of aluminum wire-array implosions conducted on the Saturn PRS at Sandia National Laboratory.<sup>1,2</sup> A more complete description of this analysis will be published shortly in an NRL Memorandum Report. The Saturn experiments were conducted to explore the validity of theoretical implosion models by investigating the variation of the keV x-ray yield as a tradeoff is made between the amount of mass imploded and the maximum velocity achieved in the implosion. In the series of experimental shots, the array mass per unit length and the initial array radius were varied in a way designed to keep the total kinetic energy in the implosion roughly constant. Thus, the variations in radiative yield will reflect how efficiently this kinetic energy is converted to keV radiation.

In the experiments, both total and keV radiative yields show a discernible trend as a function of either array mass or initial radius. One goal of the present analysis is to explain this trend by gaining greater understanding of the average plasma conditions during the thermalization of the plasma on axis. Two important factors which predict keV output in the present experiments are the average kinetic energy at stagnation and the fraction of the imploding mass involved in the radiation.

The importance to K-shell radiation of having the proper ion kinetic energy at stagnation has become well recognized.<sup>3</sup> The kinetic energy  $K_i$  must be large enough but not too large; the implosion must ionize the imploding mass and heat the electrons sufficiently to radiate, but should not cause other processes (stripping, runaway generation) to dominate. If the parameter  $\eta$  is defined as<sup>3</sup>

$$\eta = K_i / E_{min}, \quad (1)$$

where  $E_{min}$  is the energy needed to reach the K-shell (for aluminum,  $E_{min} \approx 12$  keV), then we expect greatest K-shell radiation for  $\eta > 1$ , but not for  $\eta \gg 1$ . This theory is well supported in the present experiments.

The degree of mass participation in the radiative process strongly influences the total keV output.<sup>2</sup> In the present experiments, we found considerable variation from shot to shot in the fraction of the imploding mass involved in K-shell radiation (from 0.04% to 78%). These values correlated well with the K-shell radiative power.

Experimental observations from the Saturn runs consisted of

1. Filtered PCD output records as a function of time;
2. Time-integrated keV spectra;
3. Pinhole photographs, both time-integrated and at time intervals.

The systematic analysis given here uses a procedure developed earlier at NRL.<sup>4</sup> Using this

procedure, we can infer, from x-ray photodiode, spectroscopic and pinhole measurements, the average radiated power, the average ion density and plasma temperature, and the average fraction of total mass that was involved in x-ray radiation.

In the remainder of this section, parameters for the experimental runs are presented, measurements from the data are summarized and trends are identified.

The shot parameters for the experiments are given in Table I. Two sets of 6 shots were made, one set using larger initial array diameters (and anode diameter) than the other. The implosion time and the kinetic energy at stagnation can be estimated from these parameters by using a slug model of the implosion.<sup>5</sup> This can be done using a simple linearly rising current model,<sup>3</sup> or, for greater accuracy, the current pulse can be generated from a circuit model driven by a time-dependent voltage source appropriate for Saturn.<sup>1</sup> The stagnation point is reached in the model when the pinch radius shrinks to some fraction  $x_f$  of its initial value. Implosion times for these shots range with the simple model from about 50 ns at low mass to 90 ns at high mass; with the circuit model, these times would be slightly shorter.

**Table I.** Shot parameters

Shot No.	Array dia (cm)	Mass ( $\mu\text{g/cm}$ )	$I_{\text{peak}}$ (MA)	Total yield (kJ)	keV yield (kJ)	$\eta_{0.2}$	$\eta$
<i>Set 1: Anode diameter 2.80 cm</i>							
1483	1.71	328	8.9	224	76.0	6.9	6.0
1484	1.59	473	8.7	242	38.1	5.7	4.2
1487	1.46	739	9.0	291	30.0	3.1	2.7
1488	1.40	949	9.4	224	20.0	2.7	2.2
1489	1.34	1313	8.8	270	13.2	1.8	1.6
1498	1.28	2052	9.8	228	4.9	1.3	0.95
<i>Set 2: Anode diameter 4.80 cm</i>							
1492	3.04	118	9.1	172	8.0	20	22
1493	2.81	161	9.6	170	12.2	16	17
1494	2.73	185	9.4	196	22.4	14	15
1495	2.42	328	9.7	331	63.3	8.2	8.3
1496	2.29	473	9.7	364	61.2	5.7	5.6
1497	2.20	739	9.9	338	30.1	3.8	3.5

The accuracy of the simple model in determining implosion energy can be assessed by comparing the tabulated values of the energy parameter  $\eta$ , obtained using the more accurate Saturn circuit model, and of  $\eta_{0.2}$ , the same parameter computed from the linear current model with  $x_f = 0.2$ . The difference is generally under 10%. The total energy in the implosion is proportional to the mass density times the energy per particle, or  $m\eta$ ; the experimental design of holding this

constant is reflected in the invariance of this product. The successful achievement of this goal can be seen in the near constancy of the maximum current  $I_{peak}$ , since the total implosion energy is proportional to  $I_{peak}^2$ .

Time-integrated spectra from each shot were examined to determine the prominent lines and the energy radiated in each line. The important K-shell lines are listed in Table II, and can be clearly seen in the spectra of almost all of the experimental shots. While spectral broadening and properties of satellite lines could in principle be used to obtain information on plasma conditions, experimental conditions dictate the line energy as the most reliable spectral diagnostic. We use the ratio of the energy emitted into the two most prominent lines (He $\alpha$  and Ly $\alpha$ ) to eliminate systematic errors in calibration, measurements of the continuum, and line identification.

**Table II.** Energies of important Al K-shell lines and edges

Line	Energy (eV)	Wavelength (Å)
He IC	1588	7.81
He $\alpha$	1598	7.76
Ly $\alpha$	1728	7.17
He $\beta$	1869	6.64
He $\gamma$	1964	6.31
He $\delta$	2006	6.18
He edge	2086	5.94
Ly $\beta$	2048	6.05
Ly $\gamma$	2160	5.74
Ly $\delta$	2212	5.61
H edge	2304	5.38

The energy radiated in each line was found by computer-analyzing the digitized spectra, in the range between 1.5 keV and 2.5 keV (this energy range typically included 50–60% of the total energy in the obtained spectra). Some results from this analysis are shown in Table III. The second column shows the fraction of the energy that was emitted in line radiation. Later columns show the energy fraction that was emitted in each of the lines whose energies are listed in Table II; these should sum roughly to the total in the second column. Satellites are generally included with the line totals. Line ratios can be found by simply taking the ratio of the column figures for the desired lines; for the present analysis, we used the ratio of Ly  $\alpha$  to He  $\alpha$  lines, since these were always the most prominent.

The main goal in analysis of the time-integrated pinhole data was to determine the width of the keV radiating region. Two time-integrated photographs were taken, one high-gain and one low-gain, as well as 10 fixed-time snapshots, taken at intervals of 3 ns for a 1 ns exposure time.



**Table III.** Fraction of keV radiated energy in atomic lines

Shot No.	Fraction in Lines	Fraction of restricted spectrum energy							
		He $\alpha$	Ly $\alpha$	He $\beta$	He $\gamma$	He $\delta$	Ly $\beta$	Ly $\gamma$	Ly $\delta$
1483	0.618	0.164	0.242	0.035	0.017	0.017	0.092	0.024	0.015
1484	0.593	0.202	0.253	0.034	0.017	0.017	0.028	0.013	0.009
1487	0.614	0.199	0.276	0.034	0.016	0.018	0.028	0.015	0.009
1488	0.647	0.226	0.298	0.031	0.016	0.013	0.028	0.013	0.006
1489	0.666	0.241	0.306	0.033	0.015	0.014	0.026	0.012	0.005
1492	0.709	0.291	0.357	0.056					
1493	0.560	0.188	0.238	0.034	0.011	0.006	0.053	0.018	0.007
1494	0.821	0.238	0.375	0.050	0.016	0.017	0.079	0.028	0.011
1495	0.522	0.187	0.256	0.038	0.017	0.018			
1496	0.547	0.200	0.211	0.027	0.016	0.016	0.031	0.016	0.009
1497	0.543	0.232	0.232	0.035	0.017	0.015			
1498	0.712	0.269	0.338	0.028	0.012	0.008	0.023	0.010	0.003

Data acquisition was electronic, and corrections were made for the detector response before data analysis was begun.

The high-gain, time-integrated photograph was used for the present analysis. This image was entered into the computer, and an algorithm was developed to obtain an average value of the pinch width that correlated well with visual observation, even for irregular implosions and faint images. No densitometry-type calibration was made, because the degree of arbitrariness inherent in the determination of pinch radius for any one shot made such precision unnecessary. However, because the same determination procedure was consistently followed for all shots in a given run, the pinhole analysis will accurately identify the trends in the data.

The size for each shot of the radiating region, derived from the pinhole photograph measurements, is plotted in Fig. (1), as a function of both mass and array diameter. Generally, the radiating region contracts as the mass increases and the initial array diameter decreases. The exceptions to this rule are the two low-mass, large-diameter shots (1492 and 1493), where in any event the pinhole images were so faint as to make the diameter measurements suspect.

Data interpretation followed the procedure of Coulter, Whitney and Thornhill.<sup>4</sup> Basically, this procedure is to compare measurements from the data with theoretical predictions of those quantities for a range of average plasma densities and temperatures. Contours can be drawn in density and temperature for the observed power per unit length as well as for the observed line ratios. The place where these contours intersect marks the inferred average plasma density and temperature.

The theoretical calculations were performed for a uniformly dense, isothermal plasma of the measured diameter and 2 cm in length, which was in collisional-radiative equilibrium (CRE).<sup>6</sup> Variation in opacity with size of the emission region was included in the calculation. These calculations are expressed as contour plots, with a contour showing the electron temperature and

ion density that gives rise to a given keV power per unit length. The experimental power per unit length was obtained using the yield from Table I and the measured pulsewidth; this selects one of the theoretical contours. Next, a CRE<sup>7</sup> calculation of the ratio, Ly $\alpha$  power to He $\alpha$  (plus intercombination line) power, was carried out, and contours in temperature and density for this ratio were obtained. The experimental line ratio, obtained from Table III, selects the appropriate contour in this plot. The intersection of the two selected contours marks the average plasma temperature and density, and is the result of the analysis.

Once the average density has been determined, the fraction of the mass involved in keV radiation can be estimated by comparing the mass in the radiating region (whose extent has been measured) with the total mass in the wire array. The fraction obtained in this manner might be inaccurate because of deviations from cylindrical symmetry (tending to make the calculation an overestimate) or because of radial density variations (tending to make it an underestimate). But this fraction does give some idea of the effectiveness of the machine, for the given parameters, in including all available mass in the radiation pulse.

The measurements from the data, and the plasma parameters they imply, are summarized in Table IV. Both the width for the total radiation pulse  $\tau_{total}$  and for the keV radiation pulse  $\tau_{keV}$  are given, with the corresponding average power given by the energy yield (from Table I) divided by the pulsewidth. The line ratio is taken from Table III, with (as in that table) the He $\alpha$  fraction including the intercombination line. The “pinch diameter” listed is the average diameter of the radiating region, as found from the pinhole photograph analysis. The effective eta,  $\eta_{eff}$ , for the implosion is an estimate, based on the linear current model described above and observed stagnation position  $x_f = (\text{pinch radius})/r_0$ . The average ion density, electron temperature, and fraction of the mass radiating in the K shell are obtained from the data measurements as just described.

From Table IV, it is evident that both the total and keV radiated power show a regular variation with mass and array diameter. The keV power is plotted against these parameters in Fig. (2). The variations in power are not explained by variations in the average density and temperature, which are shown in Fig. (3) and Fig. (4). A similar pattern is found, however, in the radiating mass fraction, shown in Fig. (5). The participating mass fraction was evidently a very important factor in determining the keV output power in these runs. The keV power is plotted as a function of mass fraction in Fig. (6); although the relationship is not monotonic, a greater mass fraction generally results in greater power output. The effect of increasing  $\eta$  on the keV power is also shown in Fig. (6). As was expected, the greatest keV output came from the moderate- $\eta$  shots, with maximum output for  $6 < \eta < 8$ . The same trend is seen with the calculated value  $\eta_{eff}$ , except that the keV power maximum occurs at  $\eta_{eff} \approx 10$ .

**Table IV.** Results of data analysis

Shot No.	$\tau_{total}$ (ns)	Total power (TW)	$\tau_{keV}$ (ns)	keV power (TW)	$Ly_{\alpha}/He_{\alpha}$ ratio	Pinch dia (cm)	$\eta_{eff}$	$n_i$ ( $10^{19} \text{ cm}^{-3}$ )	$T_e$ (eV)	K-shell fraction
1483	20	11.20	18	4.22	1.48	0.31	7.3	7.0	600	0.72
1484	25	9.68	22	1.73	1.26	0.21	7.4	7.0	540	0.23
1487	25	11.64	20	1.50	1.39	0.20 <sup>(a)</sup>	3.9 <sup>(a)</sup>	6.1	600	0.12
1488	30	7.47	23	0.87	1.32	0.19	3.2	4.5	620	0.06
1489	51	5.29	31	0.43	1.26	0.19	2.8	2.0	830	0.02
1498	87	2.62	32	0.15	1.25	0.09	2.7	2.7	760	0.004
1492	29	5.93	25	0.32	1.24	0.12	43.2	3.5	700	0.15
1493	26	6.54	27	0.45	1.27	0.24	25.4	1.7	900	0.21
1494	27	7.26	26	0.86	1.58	0.45	15.7	1.2	1150	0.46
1495	22	15.05	19	3.33	1.37	0.41	9.1	4.3	620	0.78
1496	36	10.11	32	1.91	1.06	0.32 <sup>(b)</sup>	7.1	5.0	500	0.38
1497	38	8.89	36	0.84	1.00	0.28	4.9	2.8	600	0.10

<sup>(a)</sup> No pinhole data; value inferred from trend

<sup>(b)</sup> Unreliable data: Actual image is washed out

## Conclusions

In these experiments, the total implosion kinetic energy was held constant, while mass and initial radius were varied over a wide range. A detailed and consistent analysis of the experimental data was conducted to estimate the average plasma parameters during the implosion, and to investigate trends in these that could explain the variation in keV radiated power.

As is shown in Fig. (6), both the average energy per particle, represented by  $\eta$ , and the fraction of the array mass participating in the implosion showed a clear relationship to the keV radiated power. No such simple relationship was found with other plasma parameters. The consideration of mass participation could be particularly important on high-power, short-pulsewidth machines like Saturn.<sup>2</sup> With a short pulsewidth, mass participation could be reduced by incomplete wire vaporization, and initial plasma temperature and density nonuniformities will be more pronounced, affecting current penetration and implosion dynamics. At high power levels, both macro- and micro-instabilities may complicate the implosion dynamics, and L- and M-shell losses could become significant during the implosion.

The results presented here provide information on the "average" state of the plasma during the implosion. Lacking data with significant time and spatial resolution, we could not consider the significant time variations in plasma conditions and radiation; nor could we include the significant gradients in temperature, density, and electric and magnetic fields that occur during the implosion. Still, these self-consistent calculations provide valuable insight into the average plasma conditions during the radiation pulse, and also provide a consistent means of comparing different

PRS implosions. To understand the impact of dynamic variations and spatial gradients, MHD simulations<sup>3</sup> can be used to generate data for known implosion parameters that can be analyzed with the same procedures given here (such an effort is currently underway). As temporally- and spatially-resolved experimental measurements become available, the procedures detailed here can be readily extended to provide rapid analysis of the data.

## References

1. K.G. Whitney, J.W. Thornhill, R.B. Spielman, T.J. Nash, J.S. McGurn, L.E. Ruggles and M.C. Coulter, "Analysis of recent Saturn aluminum PRS experiments," in *Dense Z-pinch*, Third International Conference, London, 1993, ed. by M. Haines and A. Knight, AIP Conf. Proc. No. 299 (AIP, New York), pg. 429 (1994).
2. K.G. Whitney, J.W. Thornhill, J.L. Giuliani, Jr., J. Davis, L.A. Miles, E.E. Nolting, V.L. Kenyon, W.A. Spicer, J.A. Draper, C.R. Parsons, P. Dang, R.B. Spielman, T.J. Nash, J.S. McGurn, L.E. Ruggles, C. Deeney, R.R. Prasad and L. Warren, Phys. Rev. E **50**,2166 (1994).
3. K.G. Whitney, J.W. Thornhill, J.P. Apruzese and J. Davis, J. Appl. Phys. **67**,1725 (1990).
4. M.C. Coulter, K.G. Whitney and J.W. Thornhill, J. Quant. Spectrosc. Radiat. Transfer **44**,443 (1990); M.C. Coulter, K.G. Whitney and N.G. Loter, "Analysis of Maxwell Laboratory Wire Experiments", NRL Memorandum Report 6383 (1988).
5. J. Katzenstein, J. Appl. Phys. **52**,676 (1981).
6. K.G. Whitney and P.C. Kepple, J. Quant. Spectrosc. Radiat. Transfer **27**,281 (1982).
7. J.P. Apruzese, D. Duston and J. Davis, J. Quant. Spectrosc. Radiat. Transfer **36**,339 (1986).

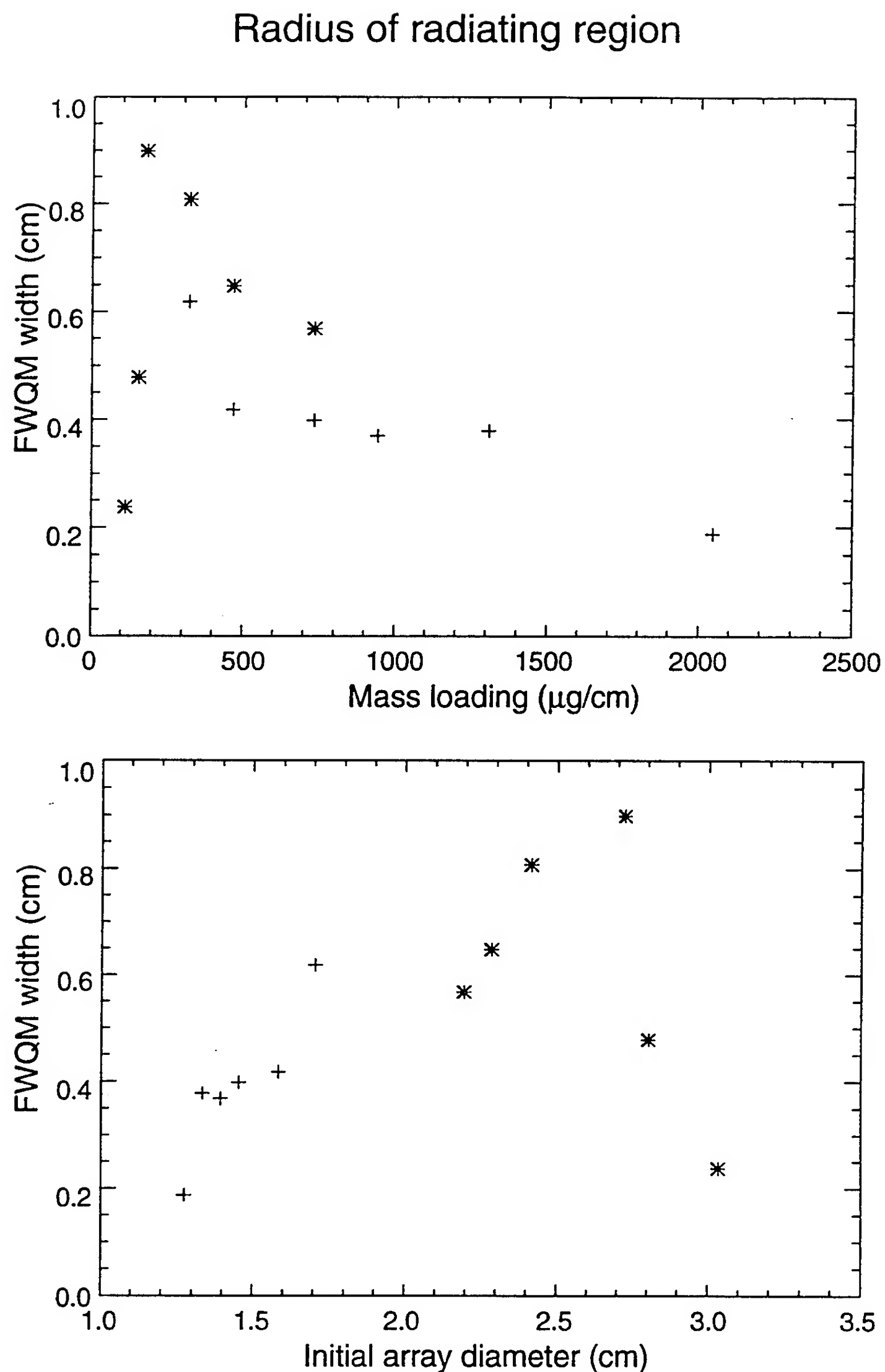


Figure 1. Results of the pinhole photograph analysis. The measured radius of the radiating region, plotted as a function of array linear mass density and of initial array radius. Different symbols were used for each of the two sets of experiments listed in Table I: set 1 measurements are plotted with a plus (+), while those from set 2 are plotted with a star (\*).

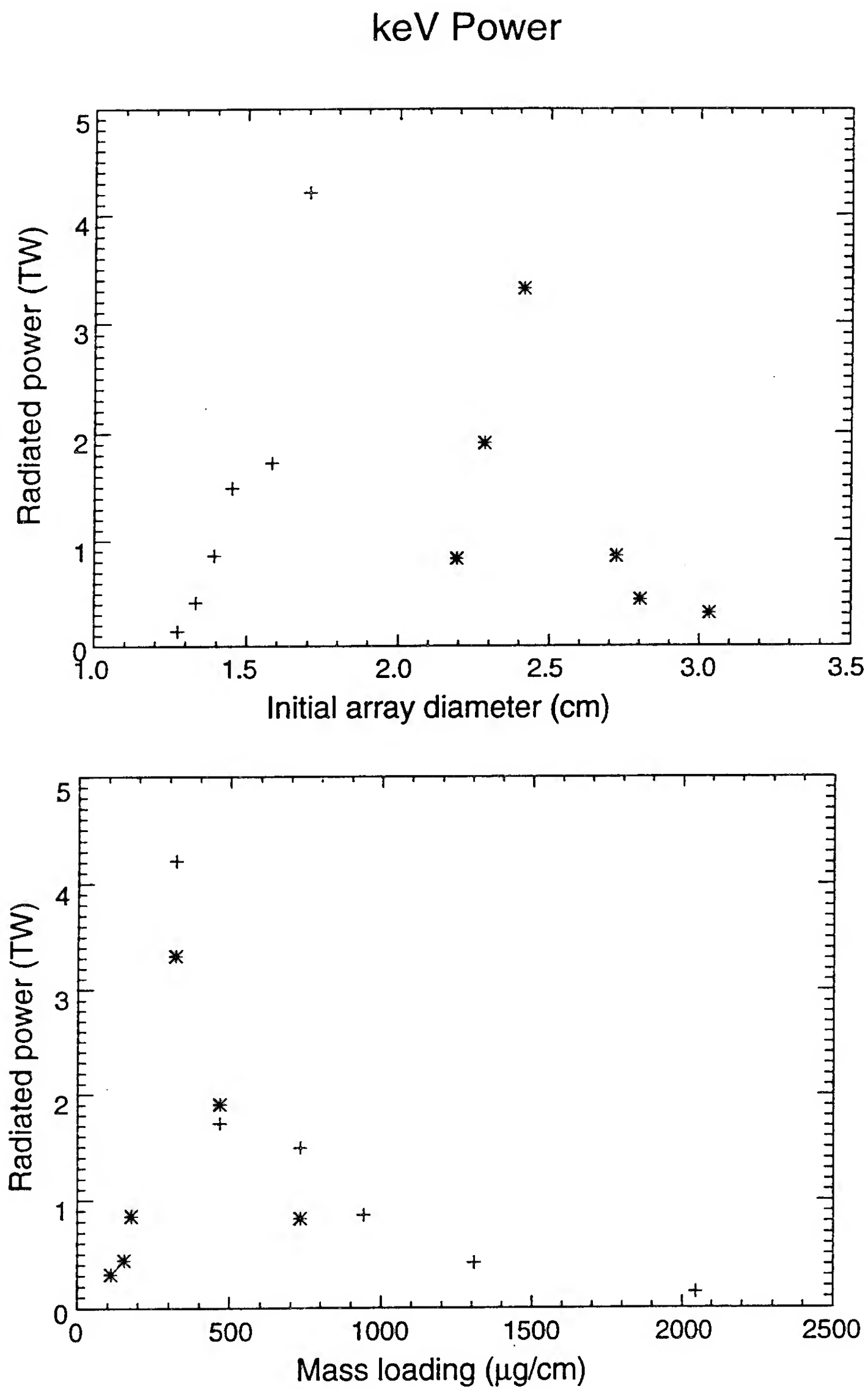


Figure 2. keV radiative power as a function of both array linear mass density and of initial array radius. Different symbols were used for each of the two sets of experiments listed in Table I, as in Fig. (1).



# Ion density

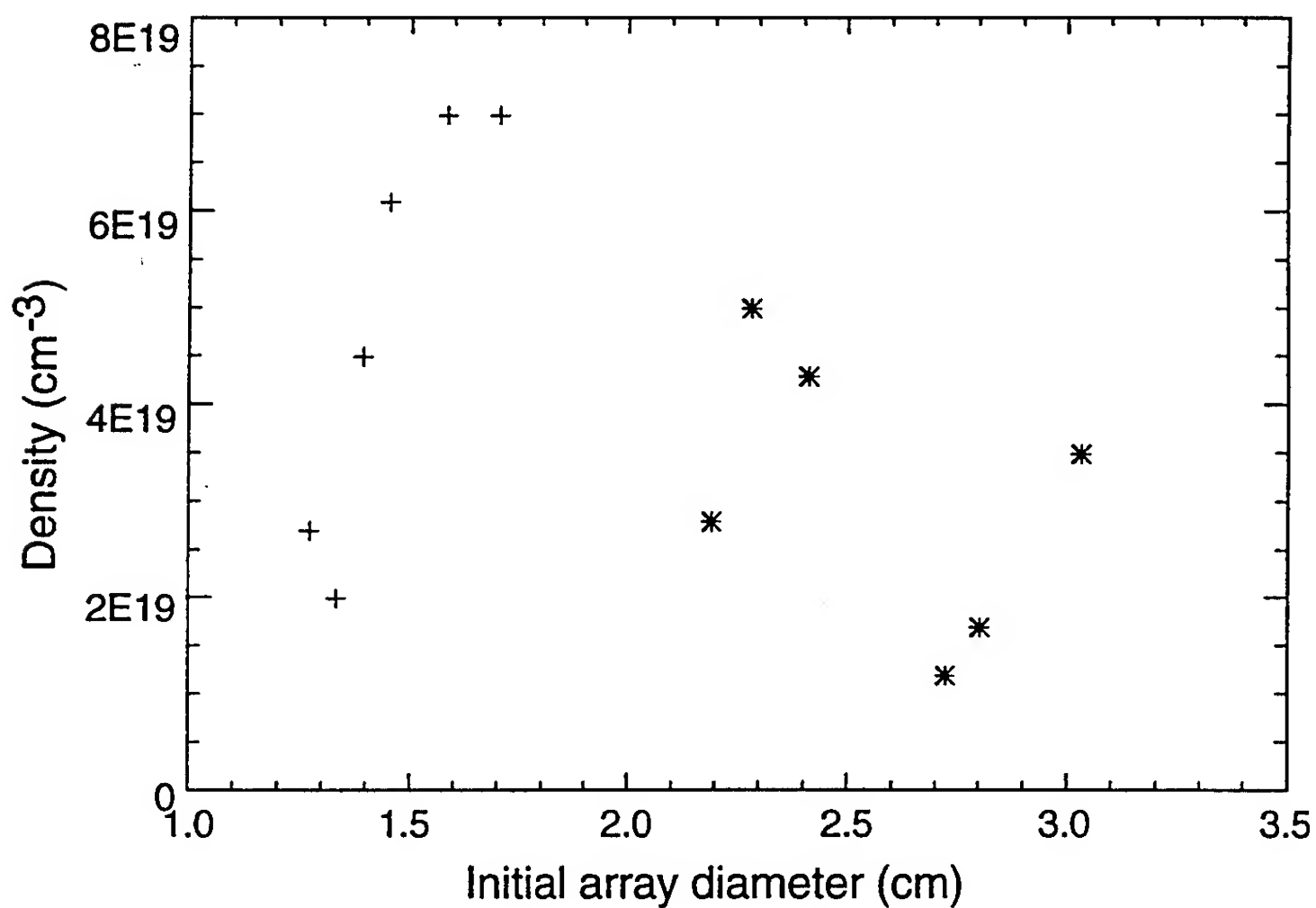
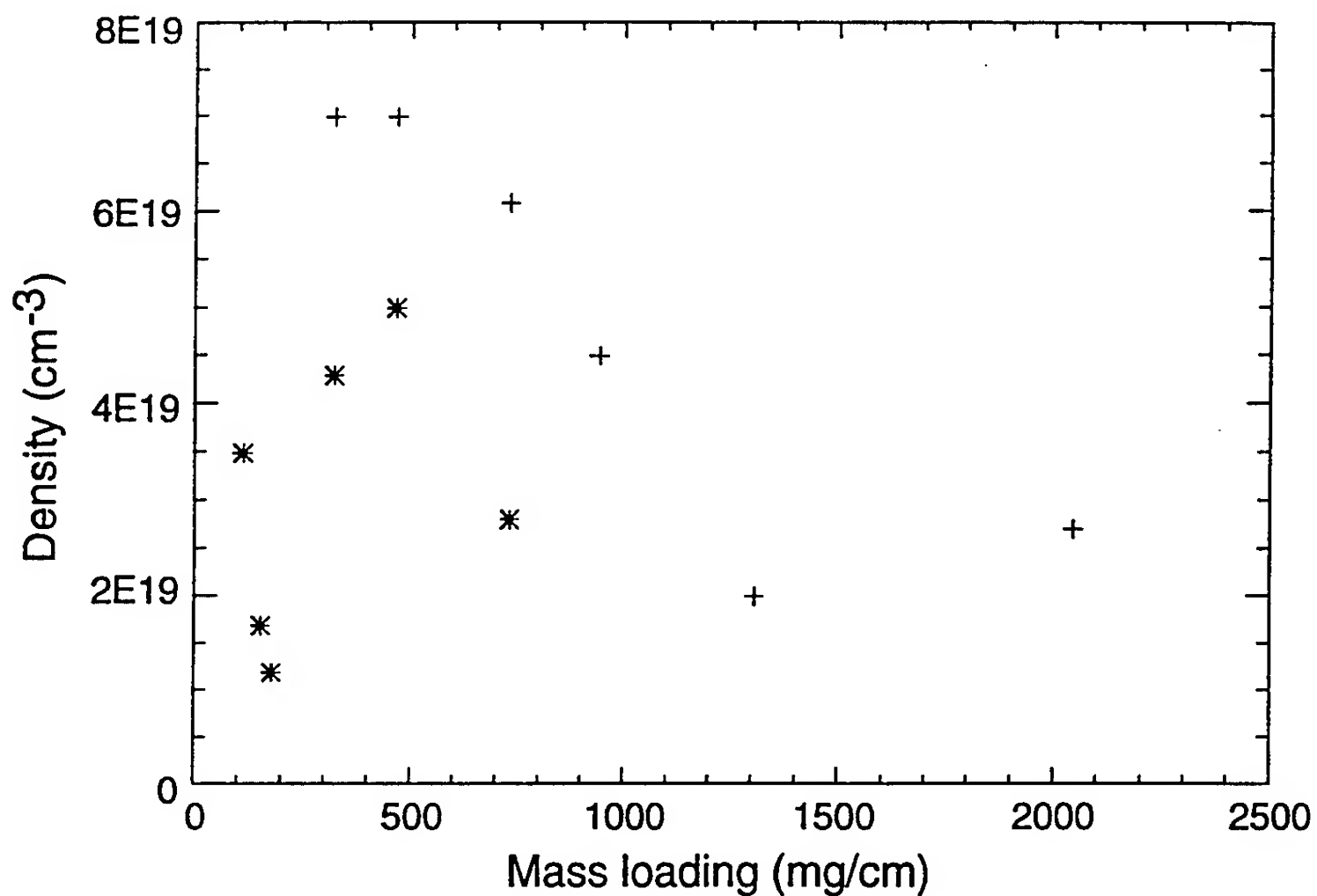


Figure 3. Ion density, inferred from the spectroscopic, pulsewidth and pinhole measurements, plotted as a function of both array linear mass density and of initial array radius. Different symbols were used for each of the two sets of experiments listed in Table I, as in Fig. (1).

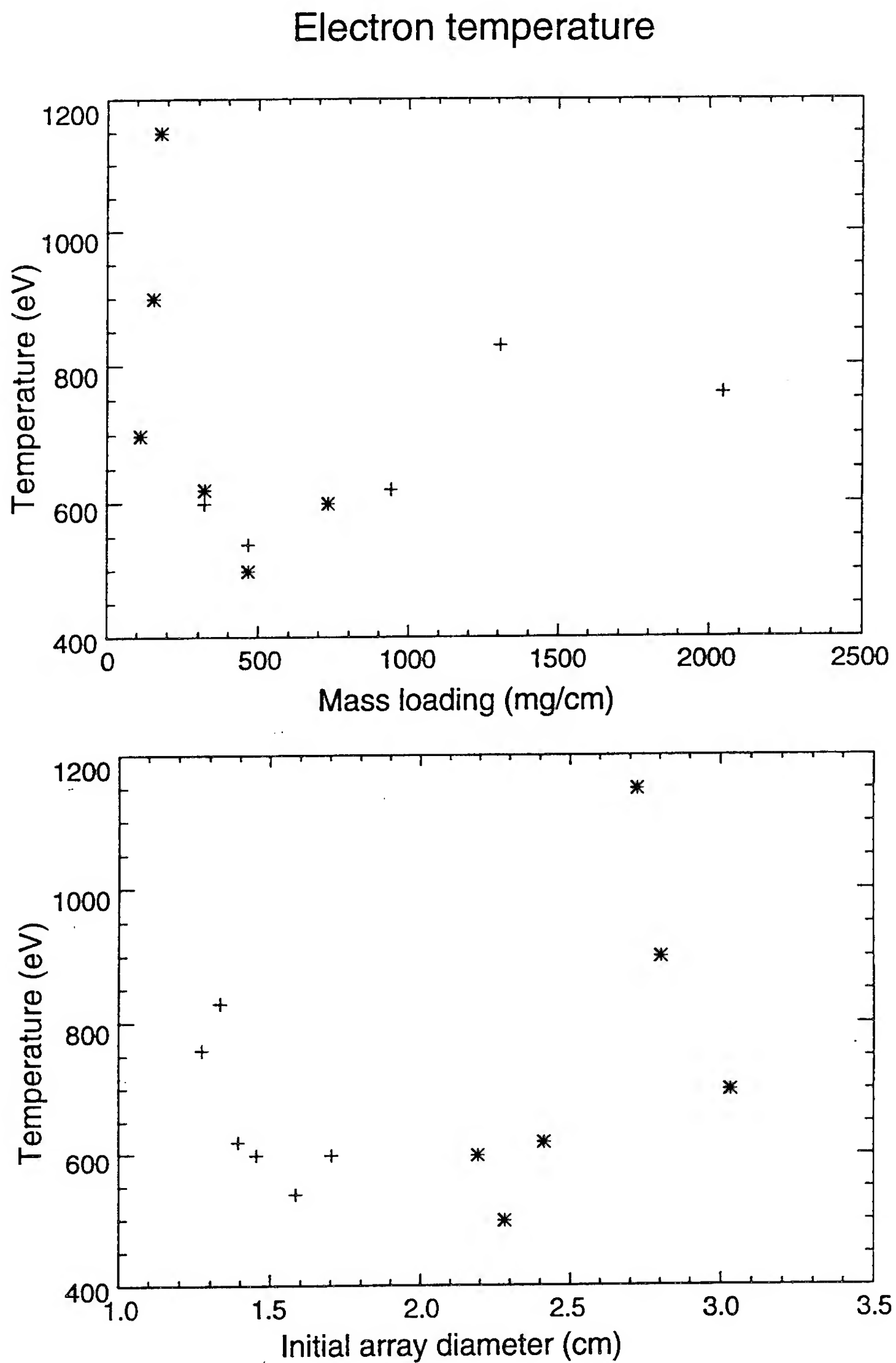


Figure 4. Electron temperature, inferred from the spectroscopic, pulsewidth and pinhole measurements, plotted as a function of both array linear mass density and of initial array radius. Different symbols were used for each of the two sets of experiments listed in Table I, as in Fig. (1).

## K-shell radiating mass fraction

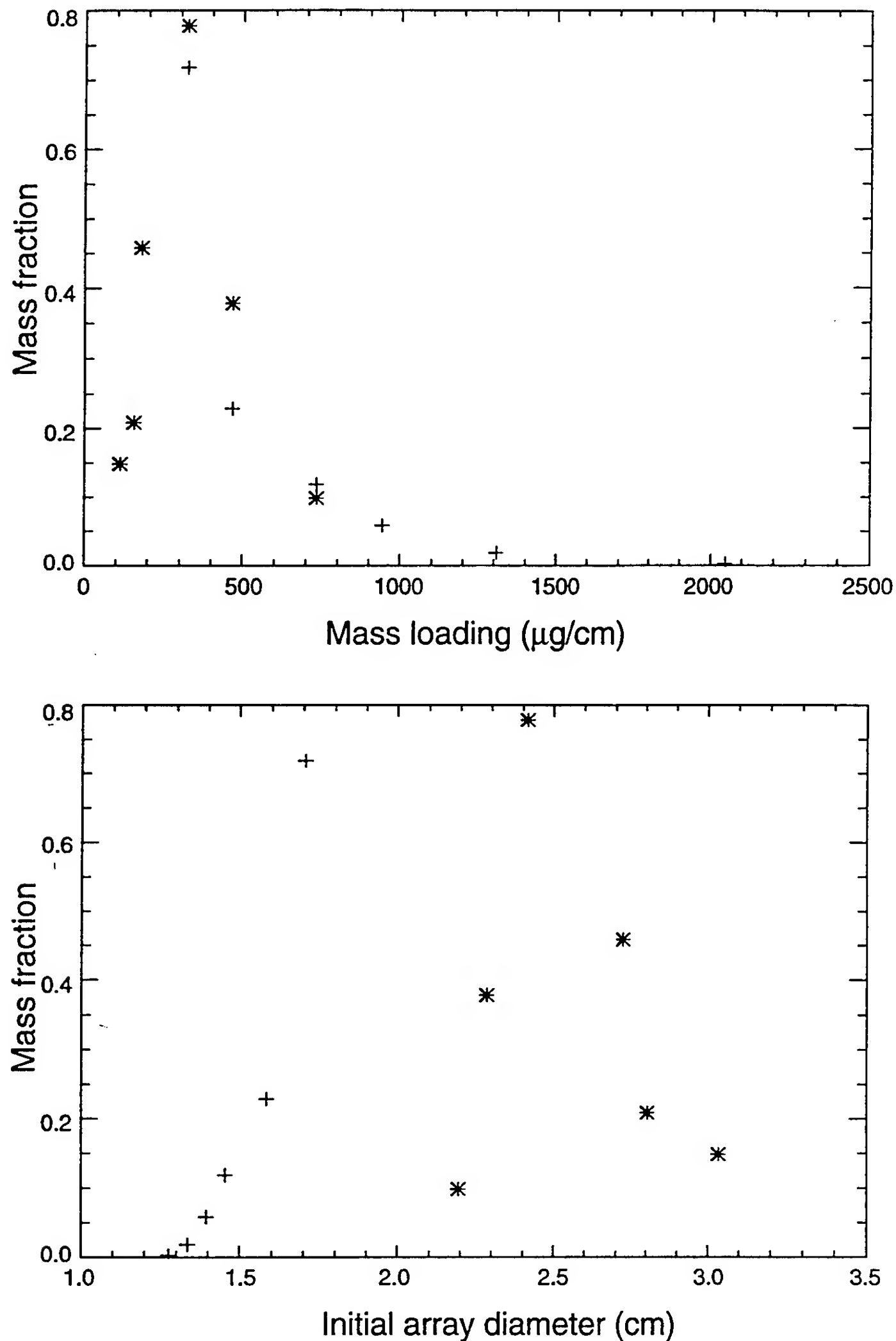


Figure 5. Fraction of the total imploding mass that is located in the radiating region. Computed from the measured pinch radius, the inferred ion density, and the known wire array mass. The mass fraction is plotted as a function of both the initial linear mass density of the array and of initial array radius. Different symbols were used for each of the two sets of experiments listed in Table I, as in Fig. (1).

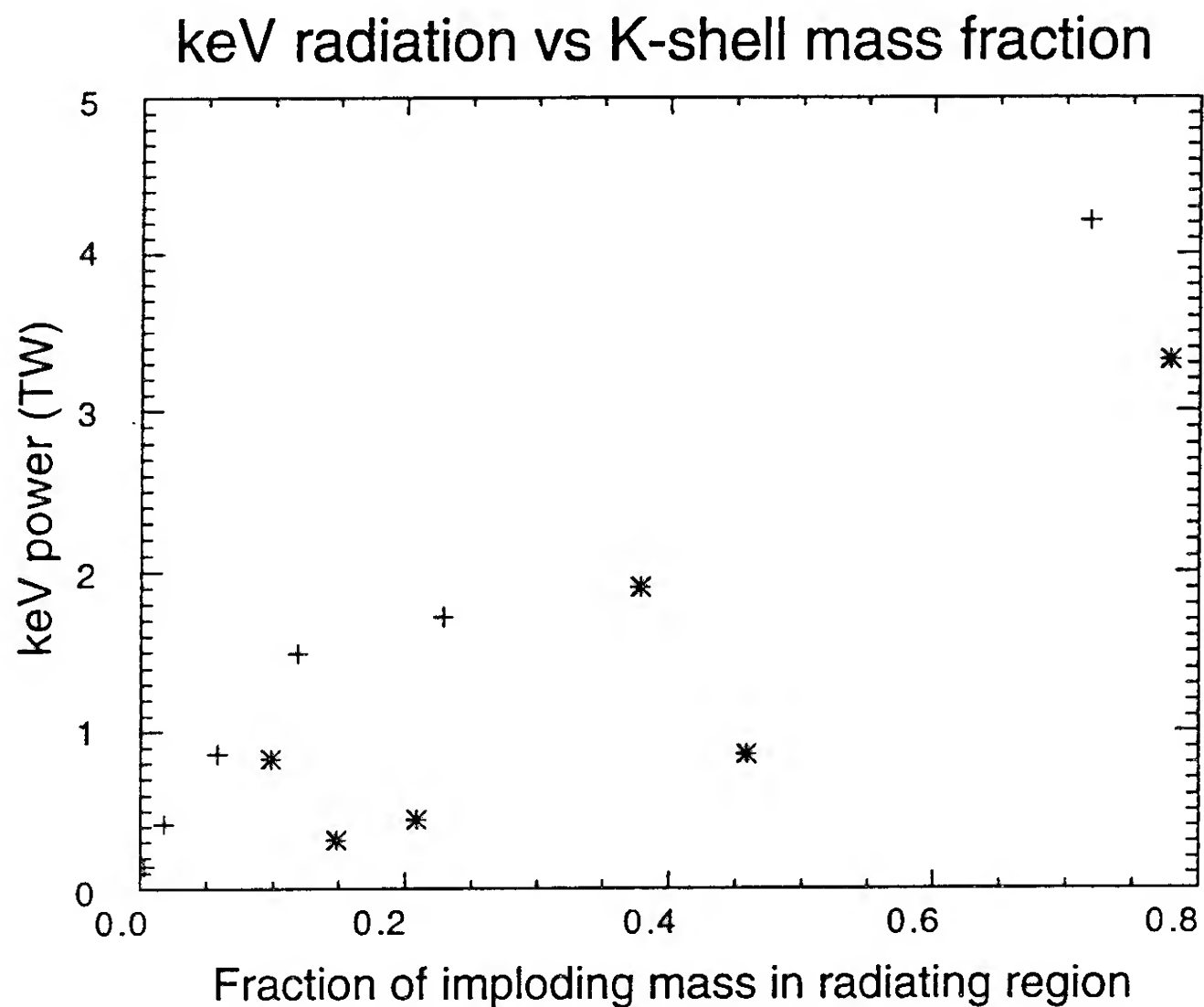
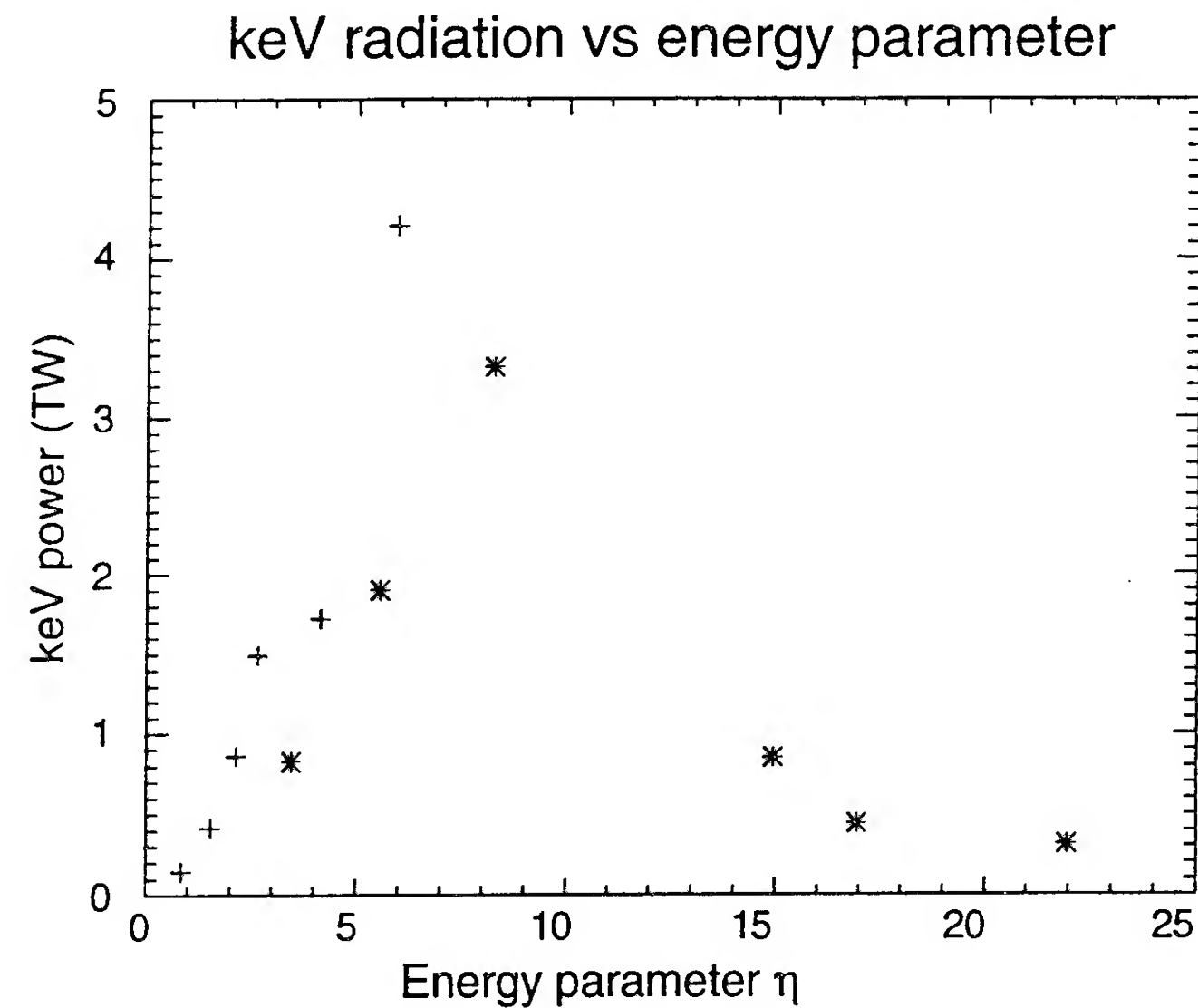


Figure 6. keV radiative power, as a function of both the parameter  $\eta$ , which indicates the average kinetic energy per particle at stagnation; and of the fraction of total mass in the radiating region (plotted in Fig. (5)). Different symbols were used for each of the two sets of experiments listed in Table I, as in Fig. (1).

## IV. INCREASING X-RAY EMISSION IN PRS LOADS THROUGH COMPARISONS OF EXPERIMENT WITH EXPERIMENT

One can draw the following useful inferences from the work described in Sections I-III above:

- All experiments conducted at Double Eagle, Phoenix, and Saturn appear to confirm
  - that the  $\eta > 1$  criterion is valid
  - that maximum emission occurs at or below the mass breakpoint,  $m = m_{BP}(\eta)$ , curve
  - that kilovolt yields increase when  $\eta$  increases in the efficient region of  $m - v_f$  space
  - that x-rays are producible from other energy inputs than kinetic
  - that x-ray conversion efficiencies of  $\sim 100\%$  of kinetic energy inputs are achievable.
- Experiments at Double Eagle, Phoenix, and Saturn also disagree among themselves and suggest the importance to x-ray conversion efficiency of
  - wire size
  - the overlap of wire explosion & implosion dynamics
  - core plasma compression heating
  - wire number and wire location or implosion uniformity.
- Mixing elements of different atomic number is a promising way to both increase x-ray yields and to promote greater simulation fidelity.

At present, there are five basic wire array parameters to use in optimizing the x-ray performance of a given machine: namely, wire size, the initial array diameter, the number of the wires, the location of the wires relative to each other, and the wire composition. In designing PRS loads, one selects wire sizes and wire number to fix the array mass. Wire location and the array mass then determine the maximum implosion velocity and implosion uniformity that can be achieved. Finally, the quality of the x-ray output is determined by both the number and choice of load materials. The data analysis described in Sections I and III has provided several useful insights about the way the choice of wire size and wire composition influence PRS performance. These insights are reviewed in this section and used to propose a new set of Saturn experiments. It is anticipated that these experiments will remedy some of the performance shortcomings that were observed in the original set of 12 Saturn experiments that were carried out in 1992.

The original Saturn experiments spanned the range of values in (load mass)-(implosion velocity) space that is shown in Fig. (1). Nine of the 12 experiments (depicted by the dots) are located on this figure by use of slug model calculations, i.e., in calculations where all of the aluminum wire mass is accelerated to the axis with the same velocities and accelerations as are generated by the  $\mathbf{j} \times \mathbf{B}$  forces of the Saturn circuit model. The calculations were terminated when the array diameter reached the nominal value of the observed plasma size on axis ( $\sim 3$  mm). The numbers that label the points are the yields per centimeter that were observed in the experiments. They are to be compared to the yield contours for 16 and 40 kJ/cm that are drawn on the figure

and that were calculated from scaling laws derived from hard-implosion 1-D MHD calculations (assuming 35% conversion efficiency of kinetic energy into K-shell x rays). Note the fall-off of the observed yields from 38 to 7 kJ/cm in the efficient region where the yields were predicted to remain nearly constant.

This yield behavior can be demonstrated in another way. In Fig. (2), the measured Saturn yields are plotted as a function of the wire diameter used in each of the 12 experiments. As seen in this figure, two subsets of experiments were done, one at small array diameters using large diameter wires and one at large array diameters using small diameter wires. The wire sizes overlapped between 1.0 and 1.5 mil diameters. In both subsets of experiments, the measured yields peaked for 1 mil wires.

A reason for this behavior was suggested in an earlier analysis (K. G. Whitney, et. al., in "Proceedings of the Third International Conference on Dense Z-pinchs, London, 1993", edited by M. Haines and A. Knight, AIP Conference Proceedings 299, p. 429), in which a strong overlap between the explosion and implosion dynamics of large wire diameter arrays (>1 mil wires) on Saturn was noted. The analysis in Section III uncovers the consequence of this overlap, which is shown in Fig. (3); namely, less and less of the initial array mass,  $m_{array}$ , participates in the K-shell emission on axis as the initial wire diameter increases beyond 1 mil. The mass of plasma,  $m_K$ , that is inferred to be radiating on axis is in one-to-one correspondence with the measured yields. This inference was drawn from an analysis that requires the consistent use of four kinds of measured x-ray data:

- time integrated K-series spectra
- XRD traces of the K-shell power output
- time-integrated pinhole pictures of the K-shell emission region
- total K-shell yields

The PI mixture experiments, whose analysis is described in Section I, provide further insight into the wire size problem. These experiments were originally designed to explore the relationship between yields and wire composition or on-axis opacity. It had been predicted (J. P. Apruzese and J. Davis, J. Appl. Phys. **57**, 4349 (1985)) that plasmas composed of two elements with similar atomic numbers would have larger emissions by up to a factor of 2 than plasmas consisting purely of either one or the other element. As seen in Fig. (4), this effect was observed on Double Eagle for wires consisting of magnesium coated onto aluminum (C. Deeney, et. al., "Increased Kilovolt X-ray Yields from Z-pinchs by Mixing Elements of Similar Atomic Numbers", accepted for publication in Phys. Rev. E). In one case where the wires consisted of 20% magnesium and 80% aluminum by weight, the observed K-shell yield was nearly double that for pure aluminum wires. More was involved in this effect than opacity, however, as an analysis of the spectral data showed. This analysis established that the magnesium emissions had occurred at higher temperatures than the aluminum emissions. This effect is illustrated for shot 2814 in Fig. (5). For this shot, magnesium emissions occurred, on average, at an electron temperature of 680 eV, while the aluminum emissions, on average, occurred at an electron temperature of 310 eV.

The opacity analysis had been done for a mixture of elements. The experiments began with a composite of elements that, it was assumed, would mix. However, the data analysis clearly



indicated that they had not. The hotter magnesium plasma implies that the current and  $\mathbf{j} \times \mathbf{B}$  forces had boiled off magnesium and brought it to the axis first. Aluminum had followed and heated the magnesium by compression. This sequence of events was later confirmed through time-resolved spectroscopy. This picture is consistent with the Saturn data analysis and clearly indicates a need to keep Al wire sizes at or below a 1 mil diameter on Saturn in order to get all of the initial wire mass to participate in the implosion and the K-shell emission on axis.

This important conclusion should be verified. For this reason a new matrix of aluminum wire shots for Saturn was designed that should demonstrate significantly enhanced K-shell emission above that seen in the first set of Saturn experiments. This shot matrix is listed in the following table, and it is mapped out in  $m - v_f$  space in Fig. (6). The numbers beside the shots in this figure indicate the number of wires used in the array, either 30 or 42. The earlier Saturn experiments, shown in Fig. (1), used only 24 wires in the arrays. The new experiments in Fig. (6) require more wires to cover the same mass range as in Fig. (1) because of the smaller sized wires.

### Proposed Saturn Thin-wire Aluminum Experiments

array length = 2.0 cm

Wire Diam (mil)	Array Mass ( $\mu\text{g}/\text{cm}$ )	Array Diam (mm)	# Wires	$\eta$	$d_{rc}$ (cm)
1.2	827	18.0	42	2.9	5.0
1.2	827	15.8	42	2.7	5.0
1.2	591	29.0	30	5.25	6.0
1.2	591	20.0	30	4.4	5.0
1.0	575	28.0	42	5.3	6.0
1.0	575	20.5	42	4.8	5.0
0.9	465	27.8	42	6.6	6.0
0.9	465	24.0	42	6.4	5.0
0.9	465	18.6	42	5.1	5.0
1.0	410	24.0	30	7.2	5.0
0.8	368	28.6	42	9.0	5.0
0.8	368	22.2	42	7.4	5.0
0.9	332	26.6	30	9.4	5.0
0.8	263	29.8	30	12.5	5.0

In summary, the data analysis that was carried out this year produced a number of important conclusions. For example,

- Wire size as well as array mass must be controlled per machine in order to maximize the mass participating in the x-ray emission and in order to optimize K-shell yields.

- Wire number can be used to control the amount of precursor plasma that reaches the axis and, therefore, the importance of core plasma in K-shell emission processes.

More specifically,

- Wire sizes should be chosen to optimize mass participation during implosion. For Saturn: Al wire sizes should be  $\leq 1$  mil so that wire explosion precedes array implosion.
- Wire number should be chosen to encourage or discourage core plasma formation. For large diameter implosions, enough wires to form a plasma shell should be used.
- The return current cage should be large enough or the wires should be staggered to minimize  $\mathbf{j} \times \mathbf{B}$  force asymmetries.
- Higher Z plasma cores should be utilized to increase photon yields above 5 keV: either mixed element wires (e.g. Ti/Al wires) or puff-on-wire.

This last conclusion indicates that the following set of PRS load designs represent alternative, complementary approaches to the same problem of increasing x-ray yields at photon energies  $>5$  keV:

- sparse, thick wire, composite wire implosions, e.g., Ti/Al wires
- puff gas on puff gas implosions
- puff gas on wire implosions.

All of these experiments attempt to heat a core plasma to higher temperatures than the surface plasma while eliminating the surface plasma's ability to reabsorb the x-ray emission and, thus, to diminish the K-shell yield.

# YIELD CONTOURS AND SATURN DATA POINTS

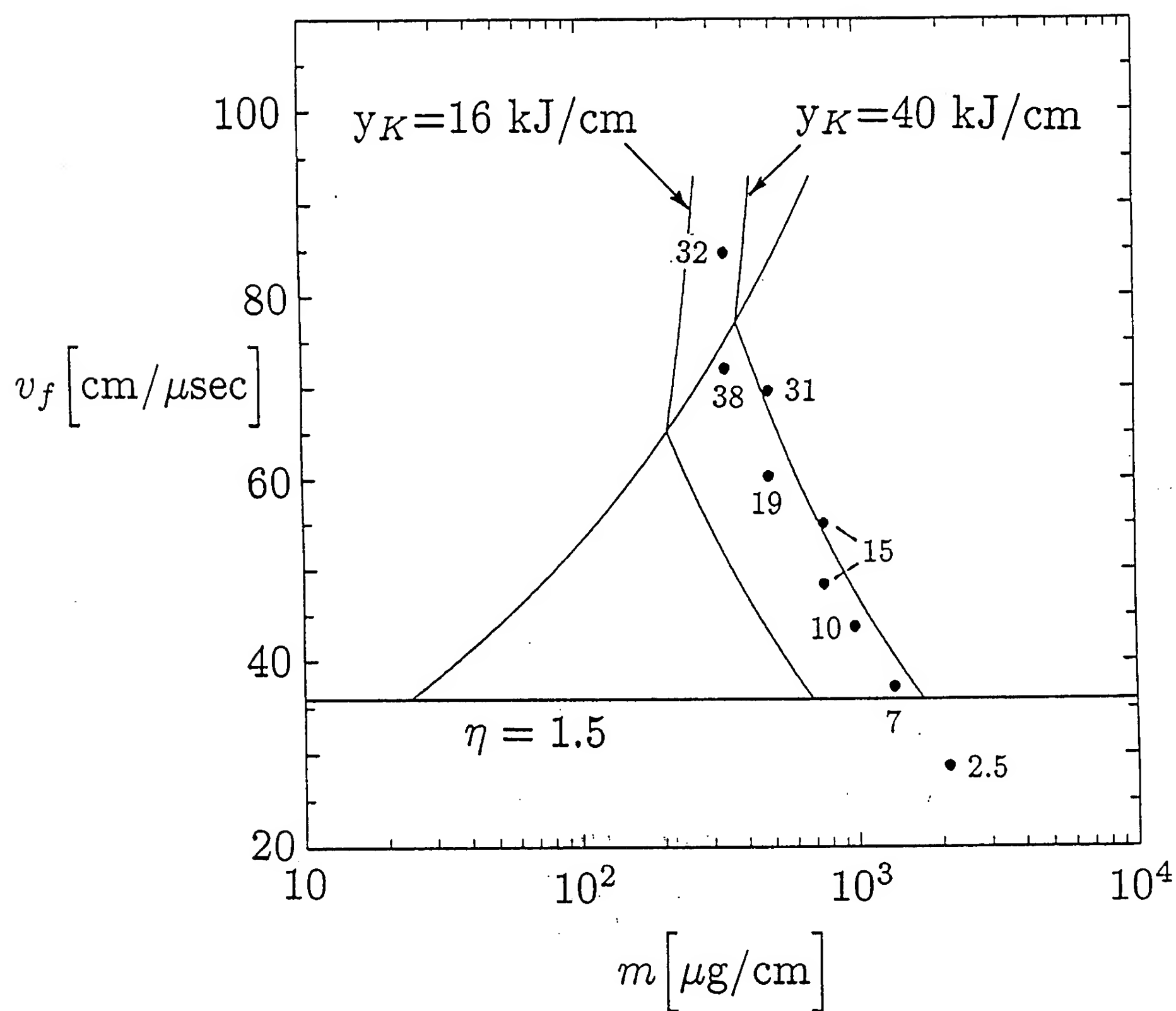


Figure 1

# SATURN K-SHELL YIELDS

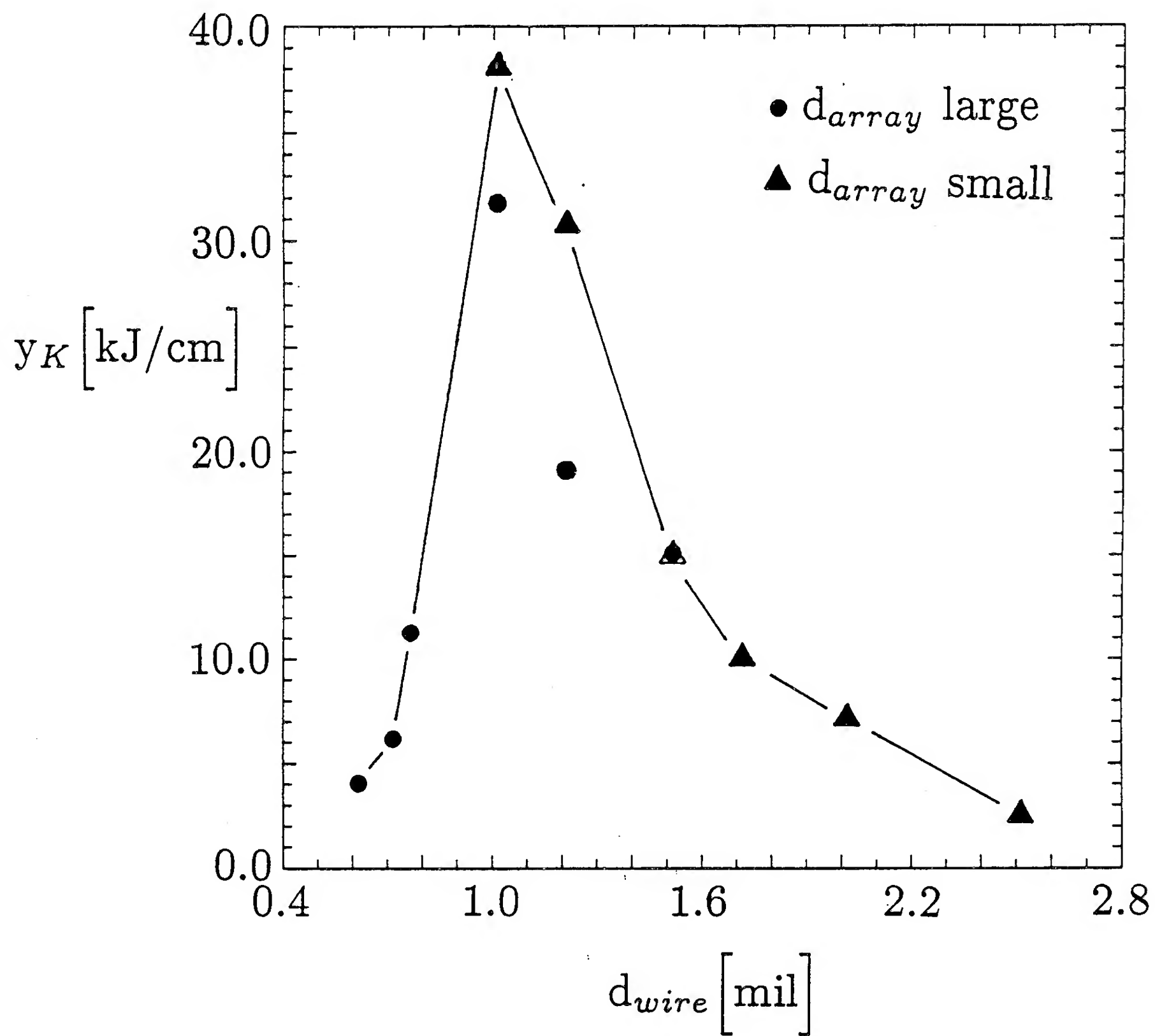


Figure 2

## SATURN K-SHELL MASS FRACTIONS

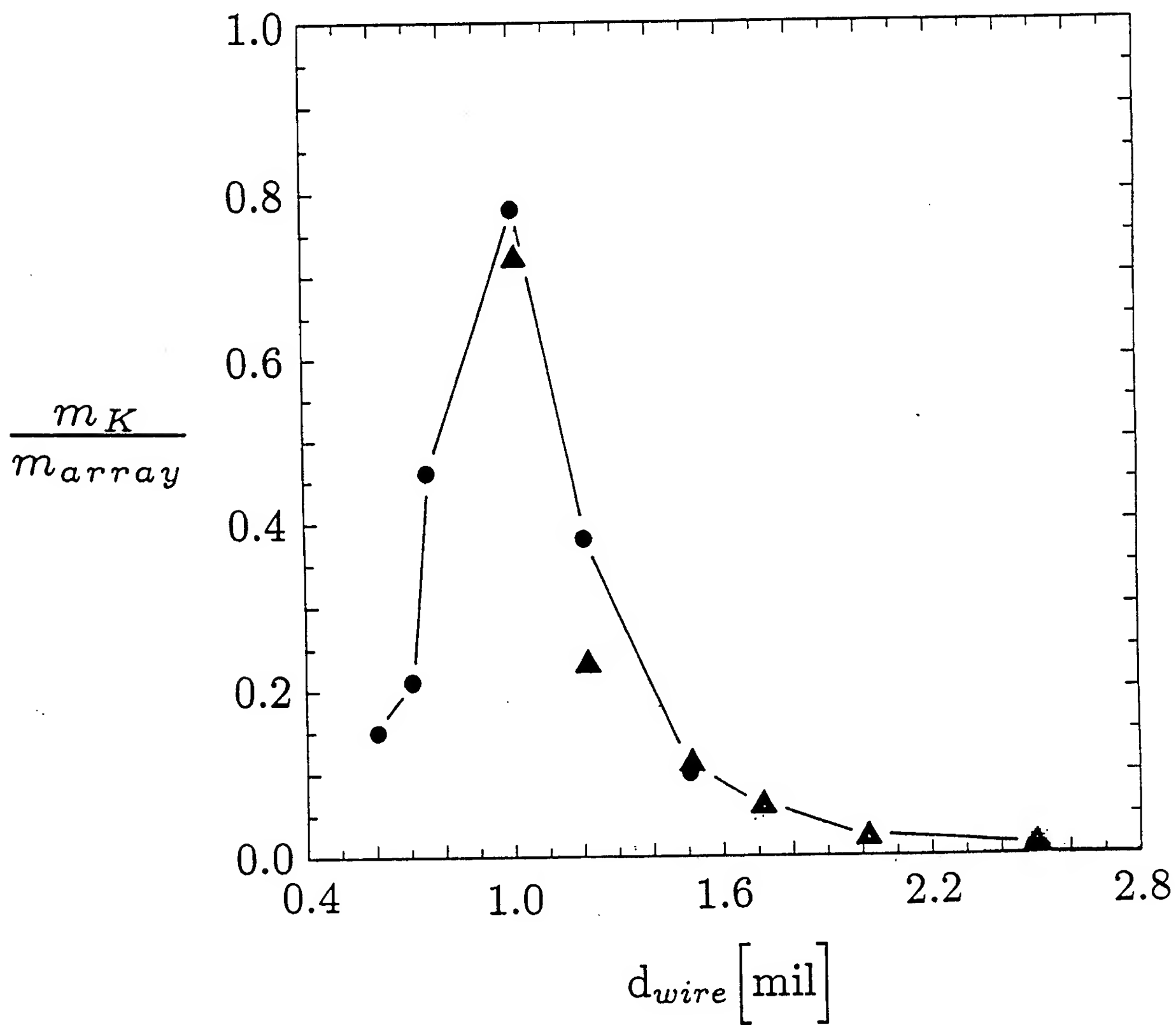


Figure 3

# PI MG/AL MIXTURE EXPERIMENTS

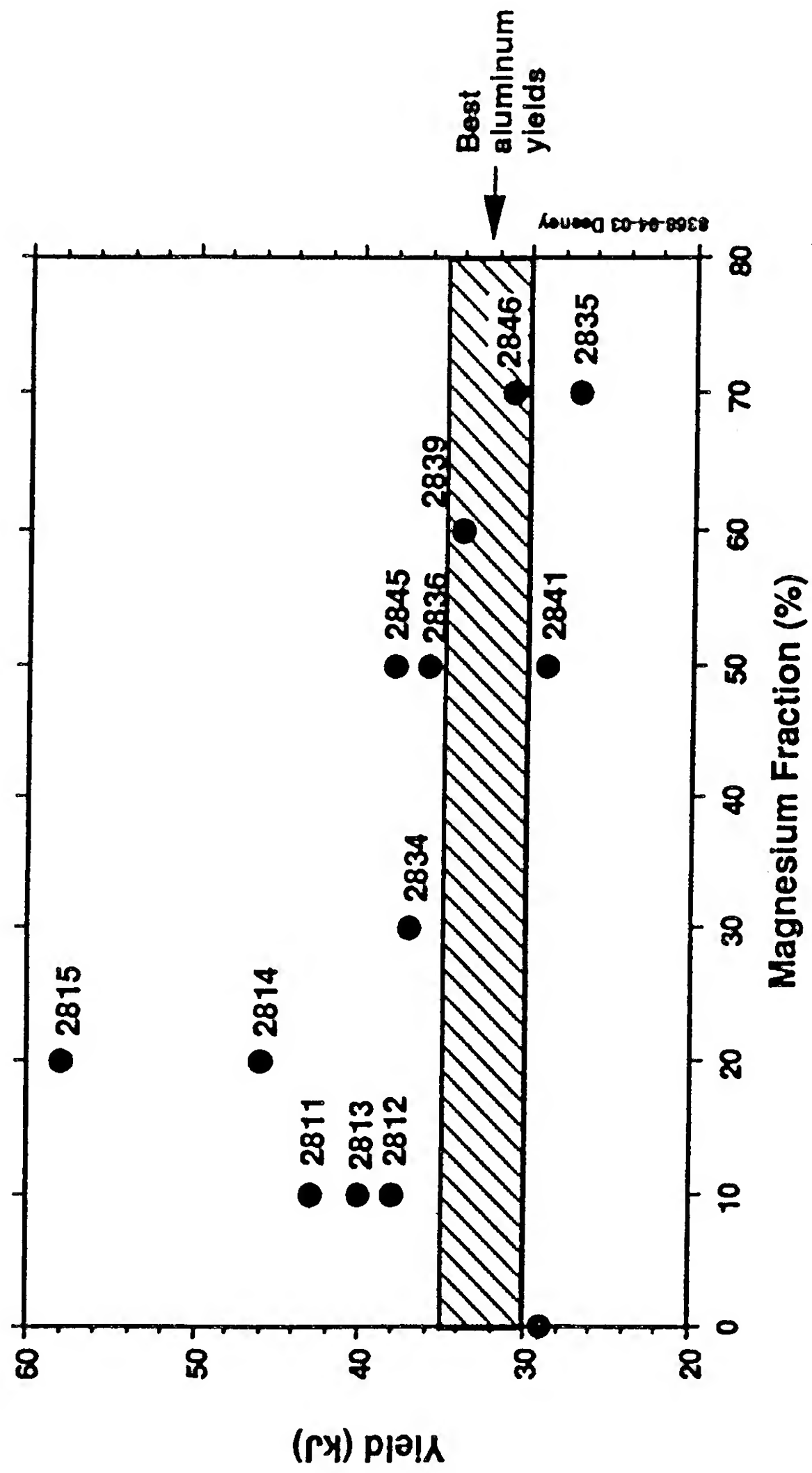


Figure 4



# A THEORETICAL ANALYSIS OF SHOT 2814 (20% MG, 80% AL) SHOWED THAT

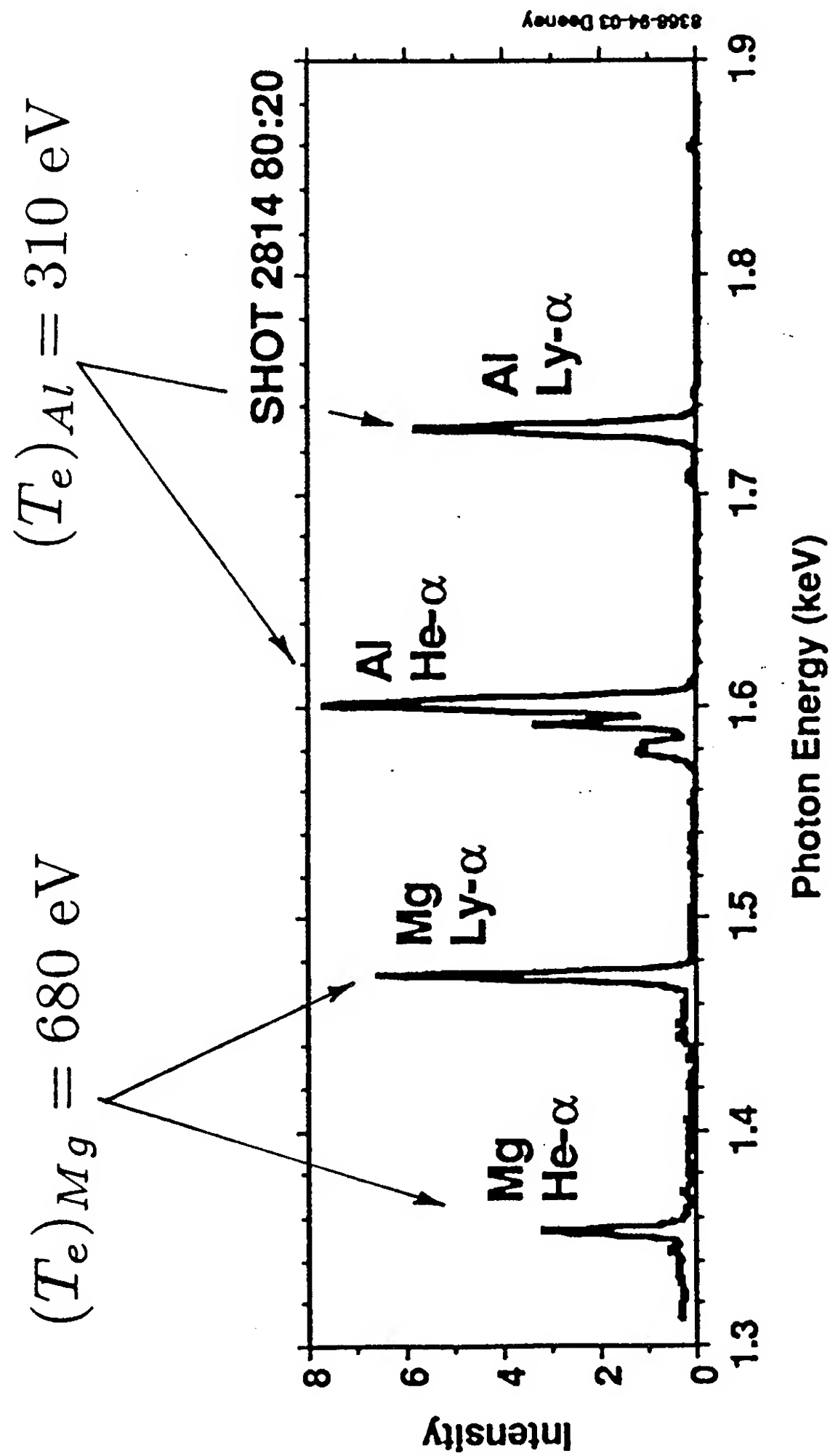


Figure 5

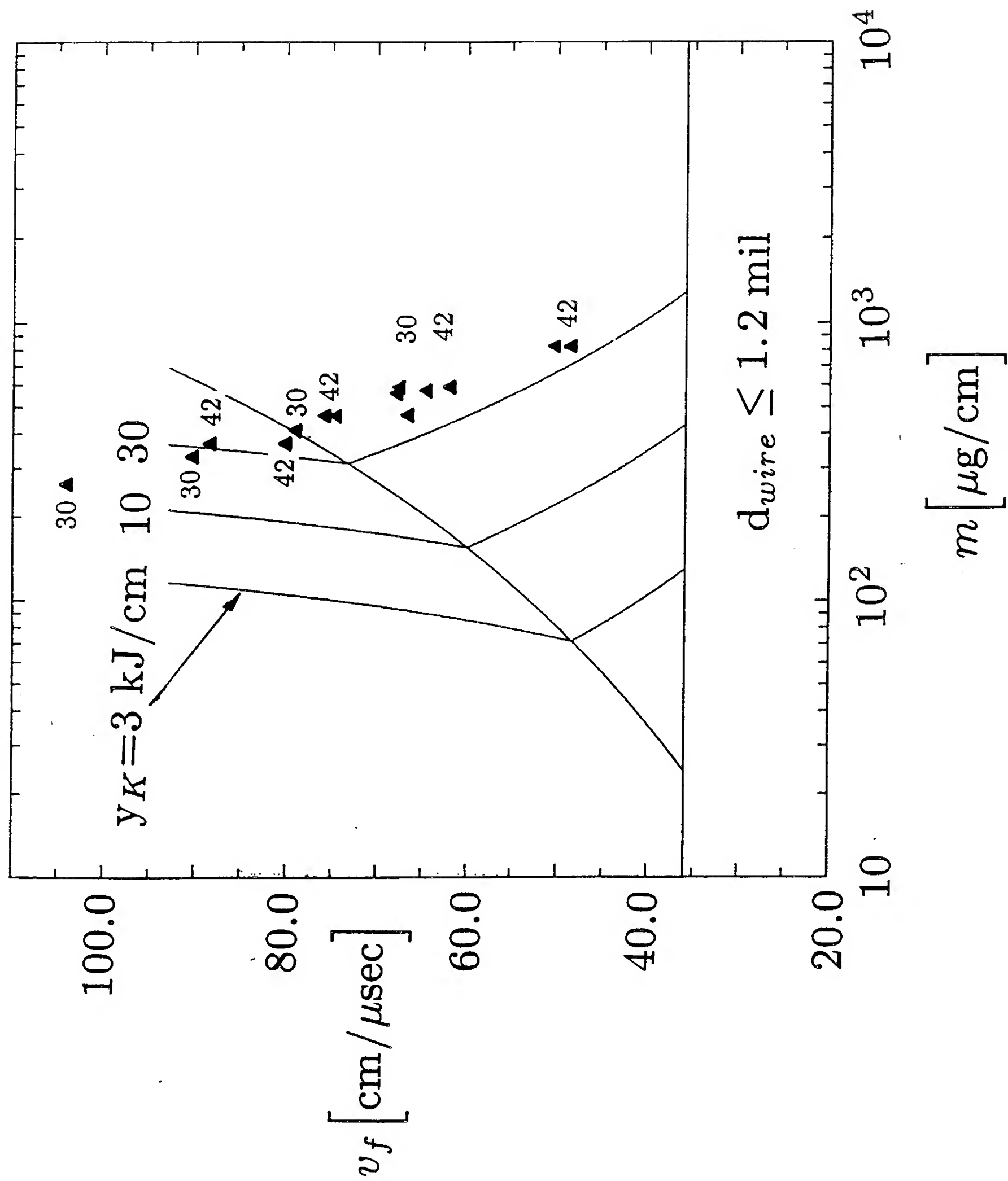


Figure 6

## V. Low $\eta$ Scaling of K-shell Emission with Mass and Z

Because of the large amount of kinetic energy and mass needed for efficient production of K-shell emission from a high Z plasma, high Z experiments performed in the near future will likely take place at low  $\eta$  values. Since there had been no systematic theoretical or experimental investigation of K-shell yield scaling with mass and atomic number Z in the low  $\eta$  regime, an investigation was recently undertaken in preparation for future high Z DNA experiments. In particular aluminum, titanium, and krypton plasmas were studied. The results of this study have identified the following problem areas: low  $\eta$  plasmas apparently remain in an inefficient  $mass^2$  (or  $I^4$ ) scaling regime at much higher masses than predicted by our earlier work which was based on  $\eta > 3$  calculations, more energy than predicted by the JDOST scaling law will apparently be needed to obtain significant amounts of krypton K-shell emission, and time dependent ionization dynamics plays an important role in K-shell scaling at high Z. The ramifications of each of these findings in terms of design of future experiments and DNA's goals are discussed following a presentation of the results.

The 1-D MHD calculations are two temperature, radiative, and they employ time dependent ionization dynamics and enhanced transport coefficients. They are similar to those described in references 1 - 3. All the calculations are begun with the plasma at an average radius of 1.25 cm. 95 % of its mass is concentrated in a 0.05 cm sized shell; the remaining mass is distributed in 6 inner cells inside the shell with a mass density that decreases exponentially towards the axis. This initialization procedure provides the calculations with numerical stability, and it also simulates the backpressure effects of plasma mass that is blown towards the axis by shocks,  $J \times B$  forces, or gas jets.

Because a large parameter range in  $(\eta, mass, Z)$  space is examined, in the interest of lowering computational costs, it is worthwhile to use as few zones as possible. This does not mean that it is reasonable to do a single zone, single temperature, calculation as was done in JDOST. By averaging over all the gradients in a plasma it is impossible to justifiably model K-shell emission when in some calculations (and experiments) that emission is produced only in the hot core of the plasma, which may contain less than 5 % of the total plasma mass. A credible calculation requires at least enough computational zones to reasonably resolve the gradients in temperature and density that occur in the plasma core. It is also necessary to resolve the outer boundary of the pinch because that is where the current flows and penetrates into the plasma. Too coarse a zoning in this region averages over too much of the colder interior plasma; thus, lower electron temperatures are calculated in turn causing too much field penetration and ohmic heating. 15 zones were used in the aluminum and krypton calculations, while 20 zones were used in the titanium calculations - after it was discovered that 15 zones were not adequate to resolve the gradients in the core of the high velocity high Z loads. The krypton calculations while qualitatively correct should be redone using at least 20 zone resolution.

To do a credible calculation of the core physics it is also necessary to include both ion and electron temperatures in the MHD equations rather than use a single temperature model as was done in some of the JDOST scaling studies. If there were no other energy

source terms, the ions and electrons would equilibrate their temperatures typically on sub-nanosecond time scales in the plasma core; however, the ions are preferentially heated by thermalized kinetic energy to hotter temperature than the electrons. This affects the core physics in that internal energy residing in the ions cannot be radiated until it is transferred to the electrons.

Each calculated implosion is driven by a linearly ramped current profile that is terminated when  $\eta^*$  reaches a preset value.  $\eta^*$  is defined as the ratio of the total-energy-coupled-per-ion to  $E_{min}$ , where the total-energy-per-ion consists of the sum of kinetic, internal and radiated energies in the plasma at the time the current is cut-off divided by the number of ions, and  $E_{min}$  is the minimum amount of energy needed to ionize an atom into the K shell.<sup>4</sup> In accord with our past work, we focus upon thermalization of kinetic energy as being the dominant mechanism for K-shell photon generation. However, with the increased plasma backpressure that results from enhanced viscosity and resistive heating, a larger portion of the energy coupled to the plasma is in the form of compressional work and ohmic heating. In order to minimize the effects of this backpressure the calculations are designed so that the specific  $\eta^*$  of interest is achieved in a 0-D calculation when the outer radius of the plasma is at a distance of 0.5 cm from the axis. In the 1-D calculation this results in  $\sim 50\%$  of the plasma energy being kinetic for aluminum with  $\eta^* = 1$  at the time of current termination. For all other high Z or higher  $\eta^*$  calculations made in this study, the proportion of kinetic energy was higher than 50%. For the highest velocity case of krypton at  $\eta^* = 1$  the proportion is 75%. Note, care must be taken when comparing the results of this work with experiments or other calculations because it is easy to imagine pinch configurations, such as those having initial outer radii very close to the axis or uniformly distributed gas loads, that would not achieve as large a proportion of the total energy being kinetic as is modeled here. Alternatively, one can imagine other pinch configurations that achieve higher proportions of kinetic energy.

## Results

Figures 1 and 2 display K-shell yields as a function of mass for aluminum and titanium loads. Each solid line curve corresponds to a fixed value of  $\eta^*$  that is attained just prior to current termination. The curves in these figures show that the mass break points are nearly the same for  $\eta^*$  between 1 and 3. The mass break point,  $M_{bp}$ , is the mass that the K-shell yield curve begins to fall off from a  $mass^2$  behavior. For aluminum the  $M_{bp}$  is approximately 100  $\mu\text{g}/\text{cm}$  at  $\eta^* = 1$ , while it is approximately 1300  $\mu\text{g}/\text{cm}$  for titanium. This is a surprising result since earlier work had predicted,<sup>1</sup> based on extrapolation from high  $\eta$  calculations, that the mass break points would be very sensitive to  $\eta$  and that they would occur at much smaller mass loads than found in these calculations. The mass break points predicted in the earlier work for  $\eta = 1, 2$ , and 3 are respectively 10, 35, and 74  $\mu\text{g}/\text{cm}$  for aluminum, and 105, 375, and 786  $\mu\text{g}/\text{cm}$  for titanium. The physics responsible for this unexpected change in scaling behavior at low  $\eta$  will be discussed in a paper to be submitted for publication early in 1995.

The dashed curves in Figs. 1 and 2 show the K-shell yield as a function of energy delivered to the load and  $\eta^*$ . These curves show a consistent progression of optimal yield

production increasing with  $\eta^*$  as the energy delivered to the load increases. This behavior is in large part due to significant innershell absorption of K-shell photons taking place at the larger mass loads. For titanium masses larger than  $2000 \mu\text{g}/\text{cm}$  and aluminum masses larger than  $500 \mu\text{g}/\text{cm}$ , innershell absorption substantially decreases the efficiency of generating K-shell photons that escape the plasma. This is especially noticeable for the  $\eta^* = 1$  curve for titanium. The optimization of K-shell emission occurring at higher  $\eta^*$  values with increasing energy delivered to the load also agrees with experimental aluminum K-shell yields in that the optimal yields on Saturn occur at much higher  $\eta^*$  values than they do for Double Eagle.

Figure 3 shows the K-shell yield scaling with mass for krypton at  $\eta^* = 1$  as calculated using the model described in the introduction of this paper with and without time dependent collisional-radiative (CR) ionization dynamics, and also as calculated by JDOST scaling laws. The JDOST scaling results show that the yield is scaling with mass (or energy or  $I^2$ ) with 6 % of the input energy emitted as K-shell photons. They are the least credible because they are benchmarked to only a single temperature MHD calculation (with compression ratio of 1/7). For aluminum and titanium, time dependent ionization has little or no effect on the K-shell yields as a function of mass load because densities at stagnation are more than sufficient to insure a rapid ionization to the hydrogenlike and heliumlike states. This is not the case for krypton because the ionization time is much longer, at an electron density of  $10^{21}$  and temperature of 1 KeV, the ionization time is more than an order of magnitude longer for krypton than titanium. As the mass load increases, the density on axis increases and reduces the ionization time. Thus, for the heavier loads the time dependent and time independent results are in closer agreement. The collisional-radiative-equilibrium CRE results show a  $mass^2$  dependence while the time dependent CR results show an even higher power scaling at the lowest mass loads. The mass breakpoint for  $\eta = 1$  according to our earlier work was  $1250 \mu\text{g}/\text{cm}$ .<sup>1</sup>

This study shows that to a reasonable approximation the mass breakpoints in the low  $\eta$  regime are close to the  $\eta = 4 M_{bp}$  predicted by our earlier work. They are 120, 1320, and  $15740 \mu\text{g}/\text{cm}$  for aluminum, titanium, and krypton, respectively. We also find that run-in energy conversion efficiencies are typically 20 % near the breakpoint mass and that for masses below this one is in a  $mass^2$  scaling regime. Based on this knowledge, the minimum energy as a function of atomic number  $Z$  that must be coupled to the load in order to obtain 10 % conversion to K-shell photons with only run-in energy inputs is calculated and displayed in Figure 4 along with similar predictions from the JDOST scaling study.

## Discussion

The conservative low  $\eta$  scaling predictions shown in Figure 4 are more justified than the JDOST predictions because they are obtained from a more complete physics model and also because krypton K-shell yields that are calculated using this model are in reasonable agreement with experimental Saturn yields, i.e. the time dependent calculation predicts no krypton K-shell emission produced by Saturn; whereas, JDOST scaling predicts about  $500 \text{ J}/\text{cm}$ . The point is not to discredit JDOST (our earlier predictions are also too large <sup>1</sup>),



but rather to emphasize the importance of doing as thorough an investigation of the low  $\eta$  scaling regime as possible because energy limitations will force future high Z experiments to be performed in this regime. The low  $\eta$  scaling curve shows that it could require 4 MJ/cm of coupled energy in order to obtain 10 % conversion of run-in energy to krypton K-shell photons (when time dependence of the ionization states is included the estimate is 8 MJ/cm). It will require the construction of more energetic machines in order to deliver this much energy to the load. However, there is also much work that can be done in improved load design that may substantially reduce these projected severe energy requirements. Note, the low  $\eta$  predictions are conservative particularly in the sense that Double Eagle has achieved argon and aluminum K-shell yields that substantially exceed the projections from run-in energy calculations. The mechanisms responsible for the larger Double Eagle yields and how the larger yields produced by these mechanisms scale with Z are important issues that certainly deserve more theoretical and experimental investigation.

All of our past scaling work and experimental evidence have shown that good conversion of kinetic energy into K-shell emission depends on achieving high core ion density and temperatures sufficient to ignite the K-shell. This is the reason that calculations that are based on turbulent behavior show that much more mass and energy is needed to attain these high ion density conditions than similar calculations based on laminar behavior. It is also for this reason that high Z load designs that promote higher ion densities on axis should be pursued. Some of these design considerations include: 1) making the implosion as symmetric as possible by using better nozzles for gas puffs, more wires for arrays, and improved return current geometries, 2) taking advantage of  $mass^2$  scaling by - imploding at low  $\eta$  for high Z experiments on relatively low power machines (aluminum on Gamble II, titanium on Saturn, krypton on Jupiter) - increasing mass per unit length by coupling as much energy into as short a length pinch as reasonable (energy coupling does not fall off linearly with pinch length), 3) investigating puff on wire loads, convergent geometry loads - such as currently being investigating at the Phillips Laboratory for liner implosions, and mixture loads. Central to all of these design considerations is the need for a better knowledge of what takes place in the plasma core and that is something that will only be accomplished by a good relationship between theoretical efforts and well designed experiments.

### References

1. J. W. Thornhill, K. G. Whitney, C. Deeney, and P. D. LePell, Phys. Plasmas 1, 321 (1994).
2. C. Deeney, P. D. LePell, B. H. Failor, J. S. Meachum, S. Wong, J. W. Thornhill, K. G. Whitney, and M. C. Coulter, J. of Appl. Phys. 75, 2781 (1994).
3. K. G. Whitney, J. W. Thornhill, J. P. Apruzese, J. Davis, C. Deeney, P. D. LePell, and B. H. Failor, "Optimization of X-Ray Emission in Z-Pinch Implosions: Theory versus Experiment," submitted to Phys. Plasmas (1995).
4. K. G. Whitney, J. W. Thornhill, J. P. Apruzese, and J. Davis, J. Appl. Phys. 67, 1725 (1990).



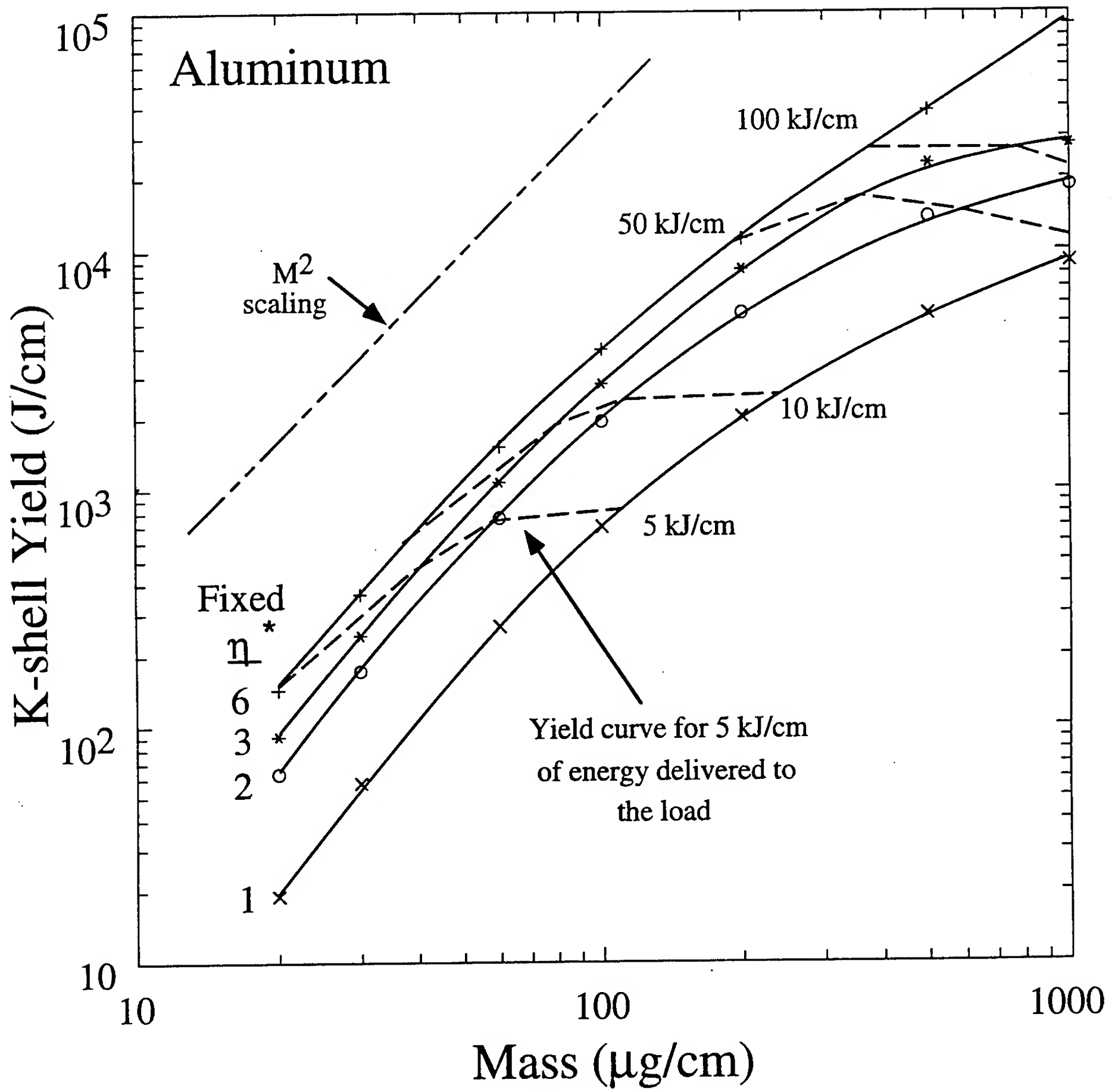


Figure 1

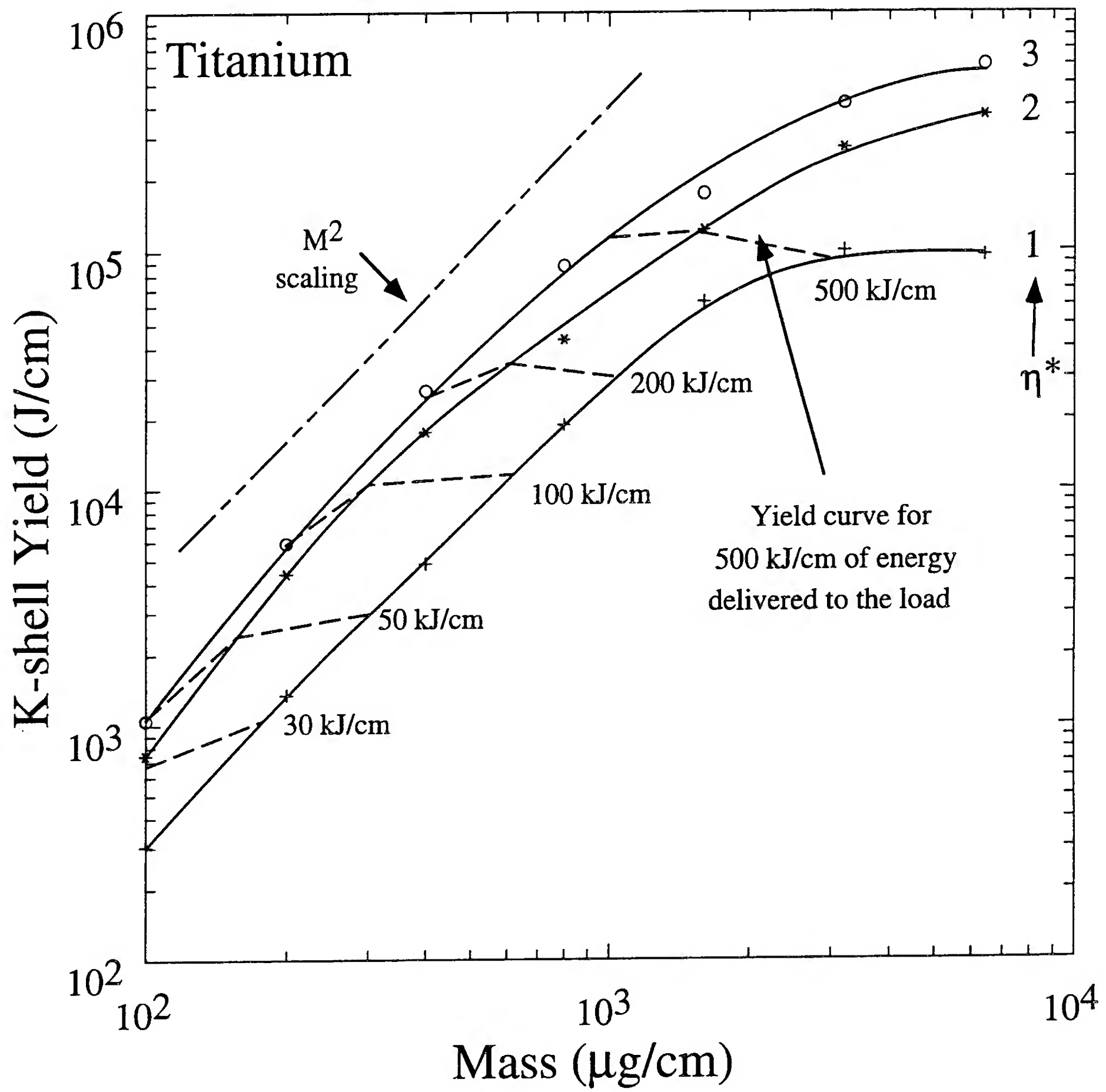


Figure 2

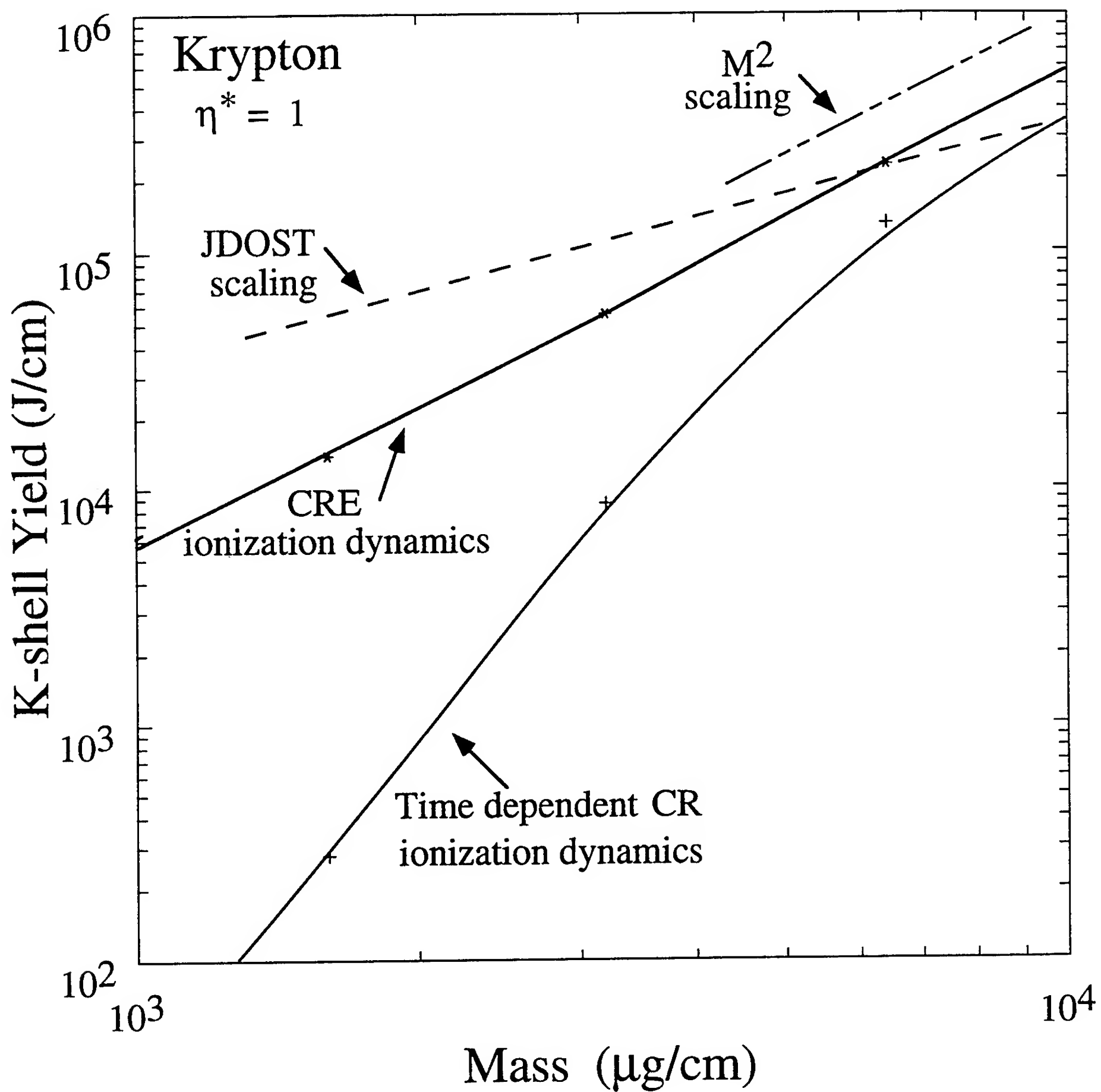


Figure 3

## Minimum Load Energy Requirements for 10 % Conversion to K- Shell X Rays

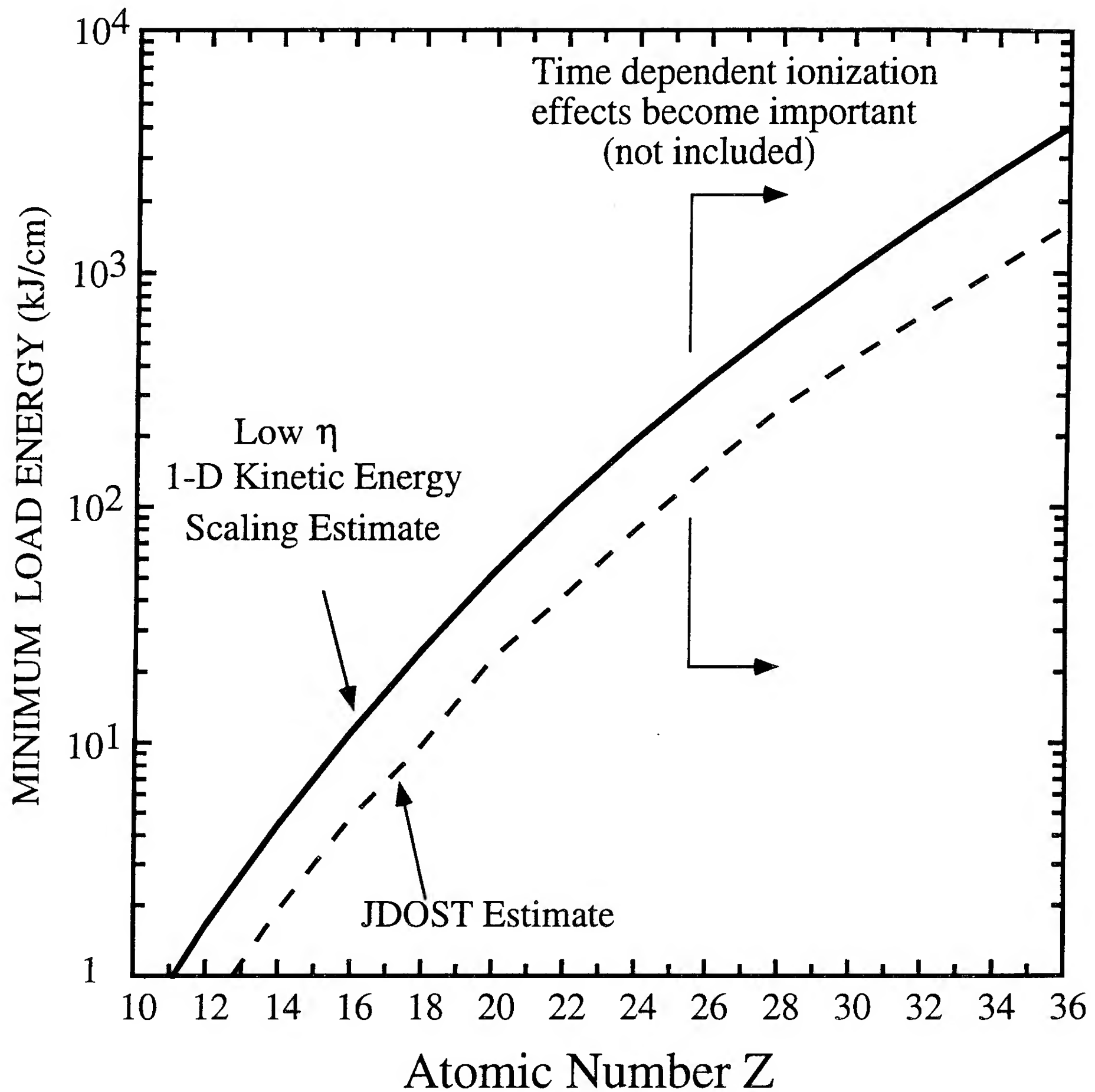


Figure 4

## VI. The Effect of Lossy MITLs on Power Flow in DECADE- and Jupiter-class Generators

### VI.1 Introduction: PRS and Convolute Shunt Interactions

The conversion of PBFA II to a PRS driver will result in front end current and power densities near the operating domain of a Jupiter class machine and perhaps gain access to megajoule kinetic energies for the source plasmas. All such designs require the convolution of high electrical power at radii on the order of a meter or less and thus raise the question of current and power losses to the load due to failures of magnetic insulation or gap closure processes. If treated from a detailed *ab initio* perspective, the modeling of losses in the (3D) electromagnetic fields of the required power convolutes is a rather difficult task. A simpler task, started here, is first to make reasonable assumptions about the wall plasma conditions. Next, regarding the wall plasmas as warm electrodes, we examine the shunting currents that would be expected between them with regard to implications about the energy coupling from the driver to the load.

As the simplest imaginable convolute model, one may consider the convergence of power to a central cylinder of a few centimeters radius via an array of radially connected posts. As the surface current density rises on the inner (solid) cylinder and on the outer (perforated) return current path, wall plasmas can develop and close the effective gap to a value much smaller than the original cold electrode dimension. These surface plasmas would then constitute warm emitters and collectors of electrons in the vacuum gap between them. The wall plasmas would also be subjected to time dependent radial voltage drops and axial wall currents. Hence the level of magnetic insulation available at the convolute site would also depend upon the load impedance behavior, making this a nonlocal problem.

A fairly straightforward problem is the estimate of the convolute losses, in the coaxial geometry just defined, based upon the warm magnetized emission model used in the modeling of POS modules. The use of the warm emission picture presumes that a sufficient energy fluence through the convolute has occurred to ignite plasmas on the electrode surfaces. The convolute gap can be effectively narrowed to a few millimeters by the plasma, and emission across the convolute gap follows much the same rules as it does across the POS gap. By placing a shunt array in the driver

model line at the convolute location, the timing and magnitude of power loss can be estimated.

Included within the scope of this baseline model are several important factors: (i) the nonlinear dependence of the gap impedance on local line voltage, (ii) the nonlocal dependence of the gap impedance on the load impedance (because the gap impedance is sensitive to the line current), and (iii) the smooth transition in gap impedance with magnetization (because of thermal spread in the emitted electron population). Excluded from the scope of this model are two important factors which must be left to future work. In particular some estimate should be made of (i) wall plasma evolution (here the gap size is fixed), and (ii) the microstability of the electron flows constituting the shunted current (here freestreaming Vlasov orbits are used).

## VI.2 Impedance of a Warm, Magnetized Child-Langmuir Gap

The shunt model is constructed as a generalization of bipolar, space charge limited flow across a gap, subjected to a fixed transverse voltage, but magnetized by a current flowing parallel in its walls. Electron emission is from a thermal population on the cathode side. The constraint of steady state net electron flow across the gap requires a unique ratio of voltage and gap current, which defines a shunt impedance, c.f. Fig VI.1a. This impedance, viewed as a line shunt element  $Z_s$ , becomes a function of the five basic line parameters: length  $\delta z_f$ , gap  $\mathcal{D}$ , the effective cathode radius  $r_C$ , and two velocity ratios  $\Omega$  and  $\Phi$ , defined below.

The magnetic field is related to the local wall current by  $B_\theta = \frac{2I}{cr}$ , which serves to define the cyclotron frequency at the emission surface,  $\omega_o = \left(\frac{2e}{m_e c^2}\right) \frac{I}{r_C}$ , equivalent to a circulation velocity ratio  $\Omega = \frac{r_C \omega_o}{v_{th}}$ . The local line voltage is denoted  $V_{gap}$ . The second relative velocity is related to the gap voltage, viz. if  $v_\Phi^2 = (2eV_{gap}/m_e)$  denotes the maximum free fall velocity in the applied electric field, then the dimensionless ratio  $\Phi = \frac{v_\Phi}{v_{th}}$  sets the energy scale of the problem relative to the thermal electron energy. One can write the shunt impedance of the ( $j^{th}$ ) line element in the general form

$$Z_{sj} = \frac{\mathcal{D}_j^2}{\sqrt{V_j^{gap}}} \frac{2^{\frac{3}{2}}}{r_C \delta z_f} \sqrt{\frac{m_e}{e}} \frac{1}{s_{oe}(\Omega_j, \Phi_j) [1 + \alpha_o(\Omega_j, \Phi_j) \sqrt{\frac{Z m_e}{m_i}}]}, \quad (VI.1)$$

and thus make contact with any transmission line formulation. The precise expression of eqn. VI.1 requires the specification of all five basic parameters, but a simplification is available.

### Approximations to the Impedance Function

As to the details, a set of three parameters: magnetization( $\frac{\Omega}{\Phi}$ ), cathode radius ( $r_C$ ), and gap size ( $\mathcal{D}$ ) emerges as a good starting point for the approximation of eqn. VI.1. The first simplification is the limit of a cold, unmagnetized, high voltage problem which has a well known Child-Langmuir solution in terms of the (order unity) parameters  $\alpha_o$  and  $s_{oe}$

$$Z_{CL} = \frac{\mathcal{D}^2}{\sqrt{V_{gap}}} \frac{2^{3/2}}{r_C \delta z_f} \sqrt{\frac{m_e}{e}} \frac{1}{s_{oe} \left[ 1 + \alpha_o \sqrt{\frac{Z m_e}{m_i}} \right]}, \quad (VI.2)$$

and doesn't involve the magnetization.

Bringing up the current in the line then magnetizes the gap, as measured by the parameter  $\frac{\Omega}{\Phi}$ . Larger values of  $\frac{\Omega}{\Phi}$  approach the critical magnetization ratio implied by Ottinger's critical current for magnetic insulation. Since the critical current is a function of the square root of the gap voltage, the critical ratio  $(\frac{\Omega}{\Phi})_{crit}$  becomes a function only of line geometry, viz.

$$(\frac{\Omega}{\Phi})_{crit} = 1.596 \frac{r_C}{\mathcal{D}} \ln\left(\frac{r_C + \mathcal{D}}{r_C}\right), \quad (VI.3)$$

and in a typical line this might be  $(\frac{\Omega}{\Phi})_{crit} \approx 1.5$ .

It turns out that the gap impedance as a function of voltage and current is mostly just a function of the magnetization  $\frac{\Omega}{\Phi}$ . Some complete gap impedance calculations are plotted in Fig. VI.1b for a set of representative test cases depending on the warm ( $\Phi = 25.0$ ) or hot ( $\Phi = 5.0$ ) emission limits. These results vary with all the parameters and span nearly six decades. In all cases the approach to the critical magnetization ratio is sufficient to force the high impedance limit. On a second plot (Fig. VI.1c) one sees the merit of normalizing to the unmagnetized impedance  $Z_{CL}$  and introducing a form factor to model the magnetic insulation. In this representation the results compress to only two orders of magnitude and fall into regular patterns. One clear feature is the asymptotic upper limit to the relative gap impedance, determined by the level of ion current which can be sustained in space charge limited emission from the effective anode surface.



From these observations the impedance rule used for warm, magnetized Child-Langmuir shunts here can be cast in the simplified form

$$Z_{gap}(r_C, \mathcal{D}, \Omega, \Phi) = Z_{CL} \mathcal{F}\left(\frac{\Omega}{\Phi}\right), \quad (VI.4)$$

and the form factor  $\mathcal{F}$  approximated by a simple cubic fit.

### VI.3 Case 1: A short shunt in the DECADE convolute

This loss study is best done by operating our DECADE model in direct drive mode because this provides modest line voltages and mimics a test with the longest exposure to current in the convolute. The shunt model in this MITL does not yet include an accumulation of the energy in the MITL walls or a detailed model of the consequent hydrodynamic or charge exchange neutral closure processes. Making the test in direct drive mode tacitly assumes that such processes have had ample time to act and to produce wall plasmas. The convolute model follows the PI design – an effective cathode radius of 10.5 cm is assumed, and we choose a shunt length of 0.3 cm (0.01 ns). The value of  $160 \text{ mg cm}^2$  for the  $M_0 R_0^2$  product is used to place this check in the mass domain offering good direct drive kinetic energy transfer. The shunt current is compared to the load current in Fig. VI.2. In that figure all time series are normalized to the value shown in the attached legend. Most of the current shunting occurs early in the rundown, before much motional impedance appears in the load, and late, near the time of stagnation.

Peak load kinetic energy (top) and peak load energy (bottom) in MJ are entered in Table VI.1 for forty combinations of initial load radius and shunt gap. The corresponding convolute MITL losses are not shown, but vary only slightly with initial radius at the fixed  $M_0 R_0^2$  value. Larger initial radii produce somewhat higher stagnation voltages but for a shorter time. As a result the efficiency of kinetic energy production (measured by the ratio of the table entries) is slightly higher, even though the peak magnitude of the shunted current is greater. At lower radii, the efficiency is somewhat lower, even though the shunted current is smaller. The higher efficiencies of the large radii implosions are then due to the longer rundown time available once the motional impedance has come up.

Clearly a detailed picture of the wall plasmas that was coupled to the history of wall energy

loading might change these results. As the effective gap in the MITL is lowered, the fractional losses in final kinetic energy are first seen in shots from high initial radii, and only later in those

**Table VI.1 PRS Coupling and Convolute Losses**

Feed Gap	$R_{0,load}$	[cm]	$\Rightarrow$	
[cm] ↓	2.4495	3.0000	4.2426	6.0000
1.20	0.870	0.957	1.080	1.270
–	2.76	2.82	2.86	3.11
0.80	0.869	0.957	1.080	1.270
–	2.75	2.81	2.86	3.10
0.40	0.865	0.949	1.070	1.260
–	2.74	2.79	2.83	3.08
0.30	0.861	0.947	1.060	1.250
–	2.72	2.77	2.81	3.06
0.20	0.852	0.934	1.040	1.230
–	2.67	2.71	2.74	3.01
0.15	0.843	0.922	1.030	1.190
–	2.61	2.65	2.68	2.93
0.10	0.815	0.891	0.987	1.120
–	2.48	2.52	2.54	2.75
0.075	0.783	0.852	0.937	1.040
–	2.34	2.36	2.39	2.56
0.05	0.705	0.755	0.815	0.874
–	2.01	2.03	2.05	2.16
0.01	0.00	0.00	0.00	0.00
–	0.379	0.379	0.379	0.372

from lower initial radii. Once the MITL gap gets below 0.5mm the load does not get to a fully imploded state, hence the null kinetic energy values.

#### **VI.4 Case 2: A longer shunt in the JUPITER IES design convolute**

This loss study uses the SCREAMER code and the JUPITER IES Baseline design model from SNL. The shunt model in this MITL does include an accumulation of the energy in the MITL walls, but no detailed model of the consequent hydrodynamic or charge exchange neutral closure processes is included. The convolute model is similar to the PI design – an effective cathode radius of about 9.88 cm, but the shunt length is chosen to be 1.2 cm (0.04 ns) and the gap is fixed at 0.3 cm. The value of  $150 \mu\text{g} \cdot 4 \text{ cm}^2$  for the  $M_0 R_0^2$  product is used.

The electrical model (Screamer) includes a Zflow POS model for the IES, and the calculation shown in Fig VI.3 provides (by implosion time) an energy delivery of  $\approx 33 \text{ MJ}$  to the line feeding the

PRS. With no shunt in the convolute the PRS absorbs  $\approx 15$  MJ of kinetic energy at implosion. The balance of the IES output energy is absorbed in the walls and stored in the load cavity inductance. Turning on the shunt provides the behavior shown in Fig VI.4, with the PRS receiving most ( $\approx 13$  MJ) of what it got before and the output of the opening switch at implosion actually increasing to  $\approx 34$  MJ. The energy absorbed in the walls is comparable to that absorbed in the shunt, and the early action of the shunt also lengthens the time to implosion. Both the lower shunt impedance seen by the POS and the longer implosion time contribute to the slightly enhanced energy extraction from the POS model.

## VI.5 Conclusions

The primary lesson here is that soft driver machines can respond to a convolute shunt by delivering more energy to the PRS load than they would ordinarily deliver to an unshunted PRS. The additional energy partially makes up for the shunt losses in any convolute and allows effective PRS operation in spite of the convolute short circuit losses. A secondary observation is that the selfconsistent, nonlinear, nonlocal and time dependent nature of the magnetic insulation processes in the shunt are crucial to a credible calculation, since no constant shunt impedance could discriminate between the implosion histories of different masses.

It must be noted as well that the gap sizes quoted here are not the cold ( $t_0$ ) gaps of the convolute MITL, but rather the evolved gaps between warm electrode plasmas which must be estimated by other means. An extensive campaign of study is planned to calibrate and to improve the theory using 2 and 3D particle codes, but the fundamental coupling behavior must remain similar to this 1D formulation.

**Fig. VI.1a Simple Convolute Geometry and Orbits**

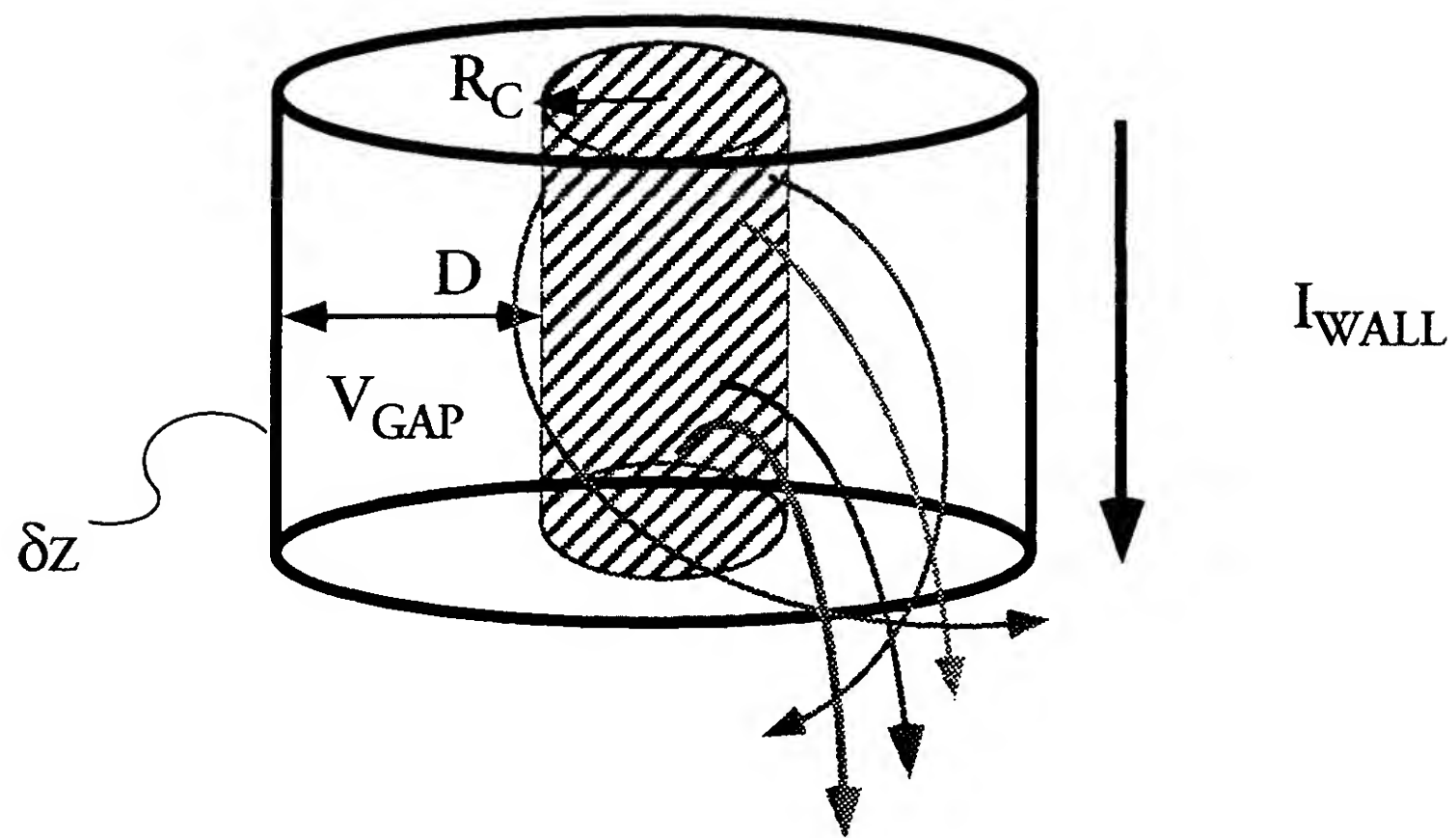


Fig. VI.1b Gap Impedance with Magnetization

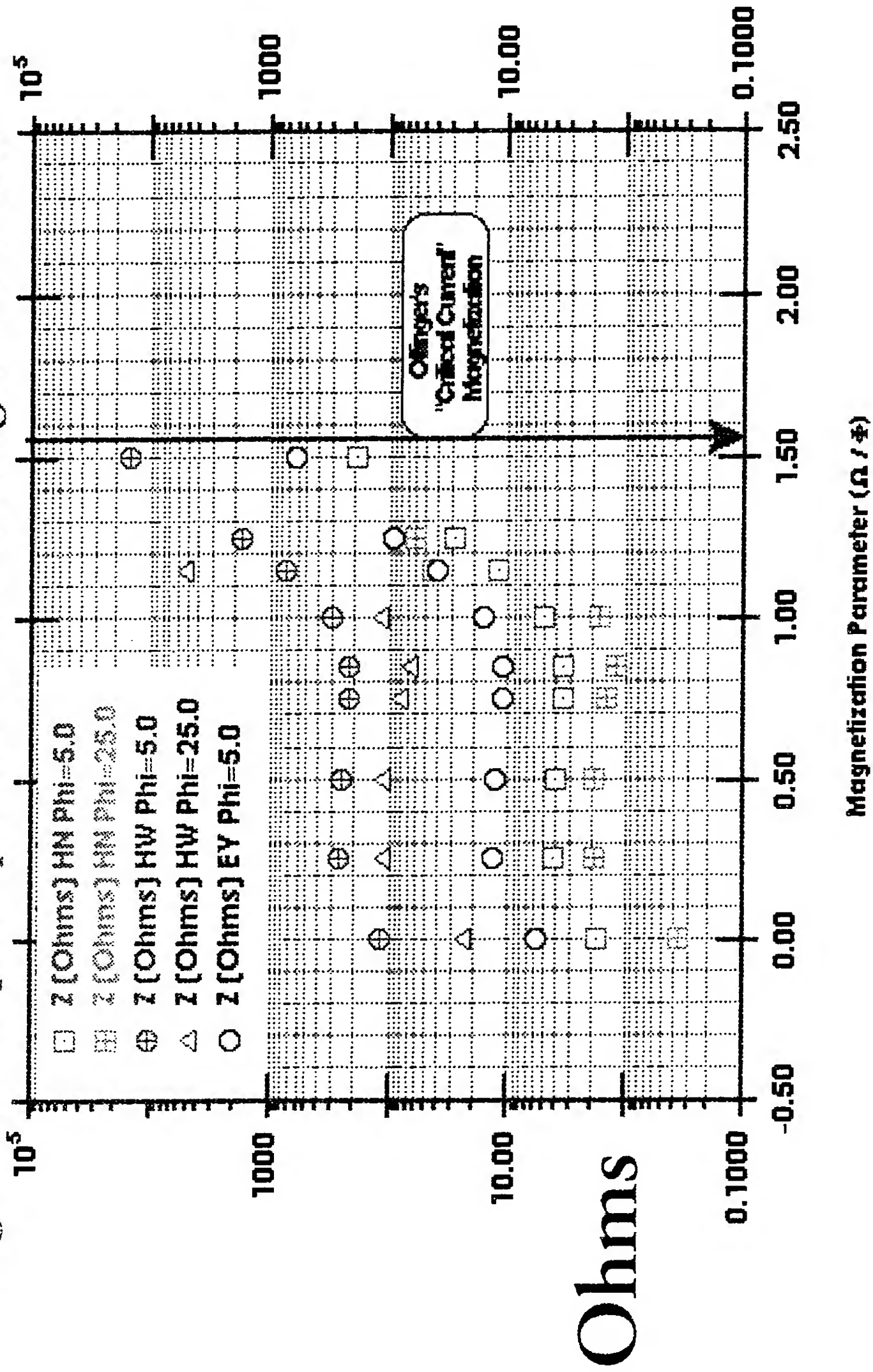


Fig. VI.1c Impedance Form Factor with Magnetization

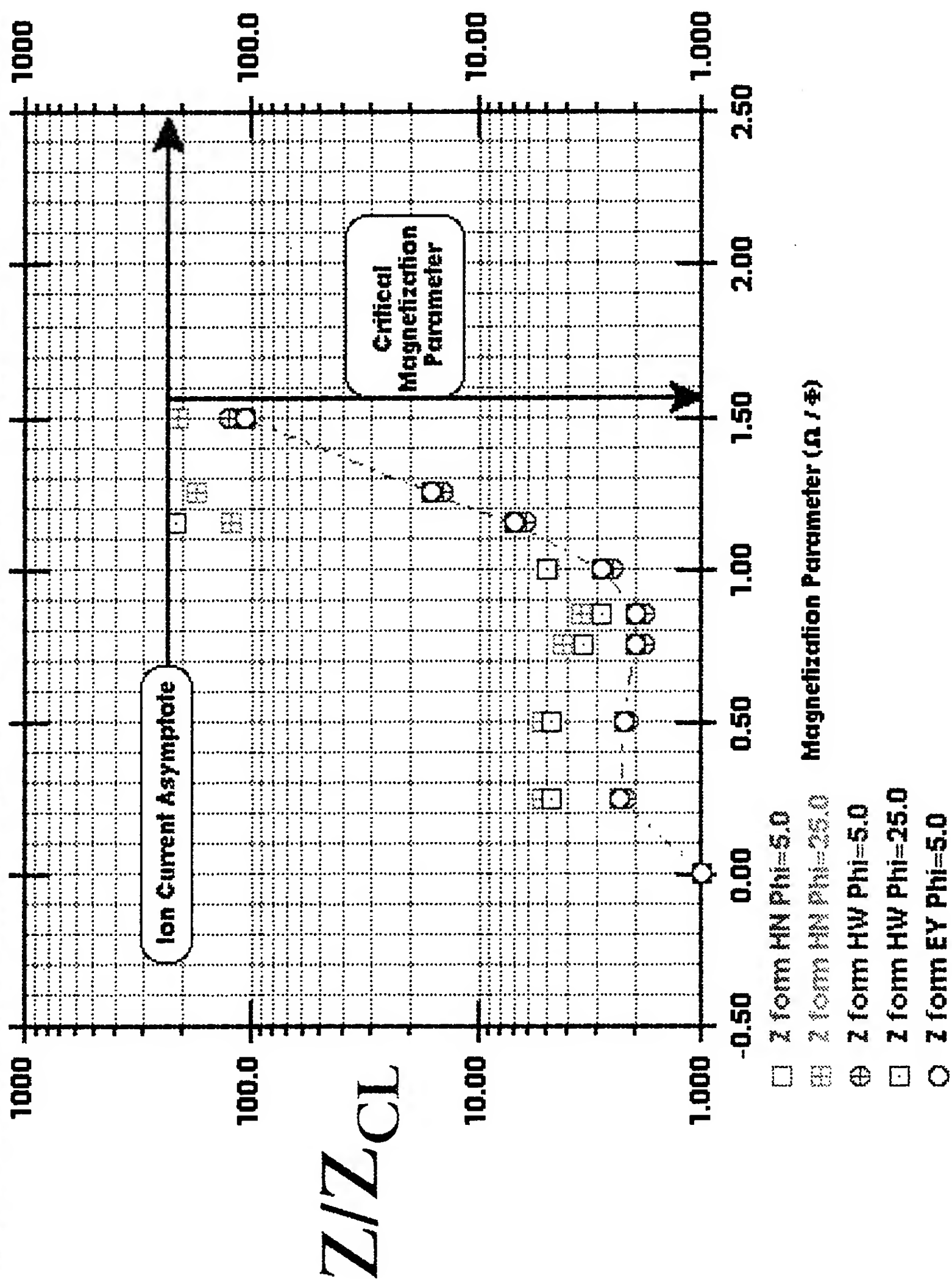


Fig. VI.2 DECADE with a Convolute Shunt

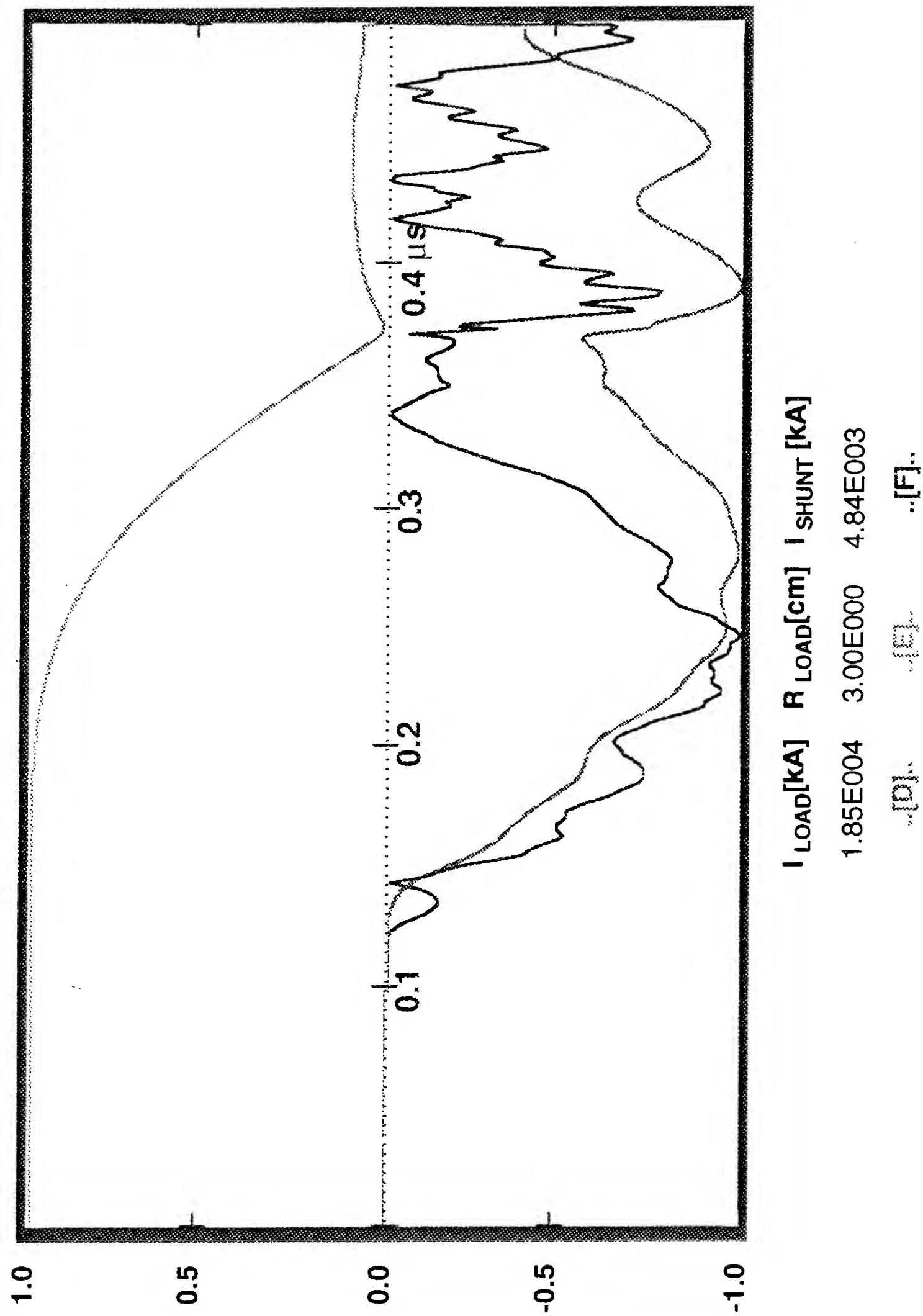




Fig. VI.3 SNL Screamer equipped with the shunt model and the "JDOST Final Baseline Design", using an IES option.

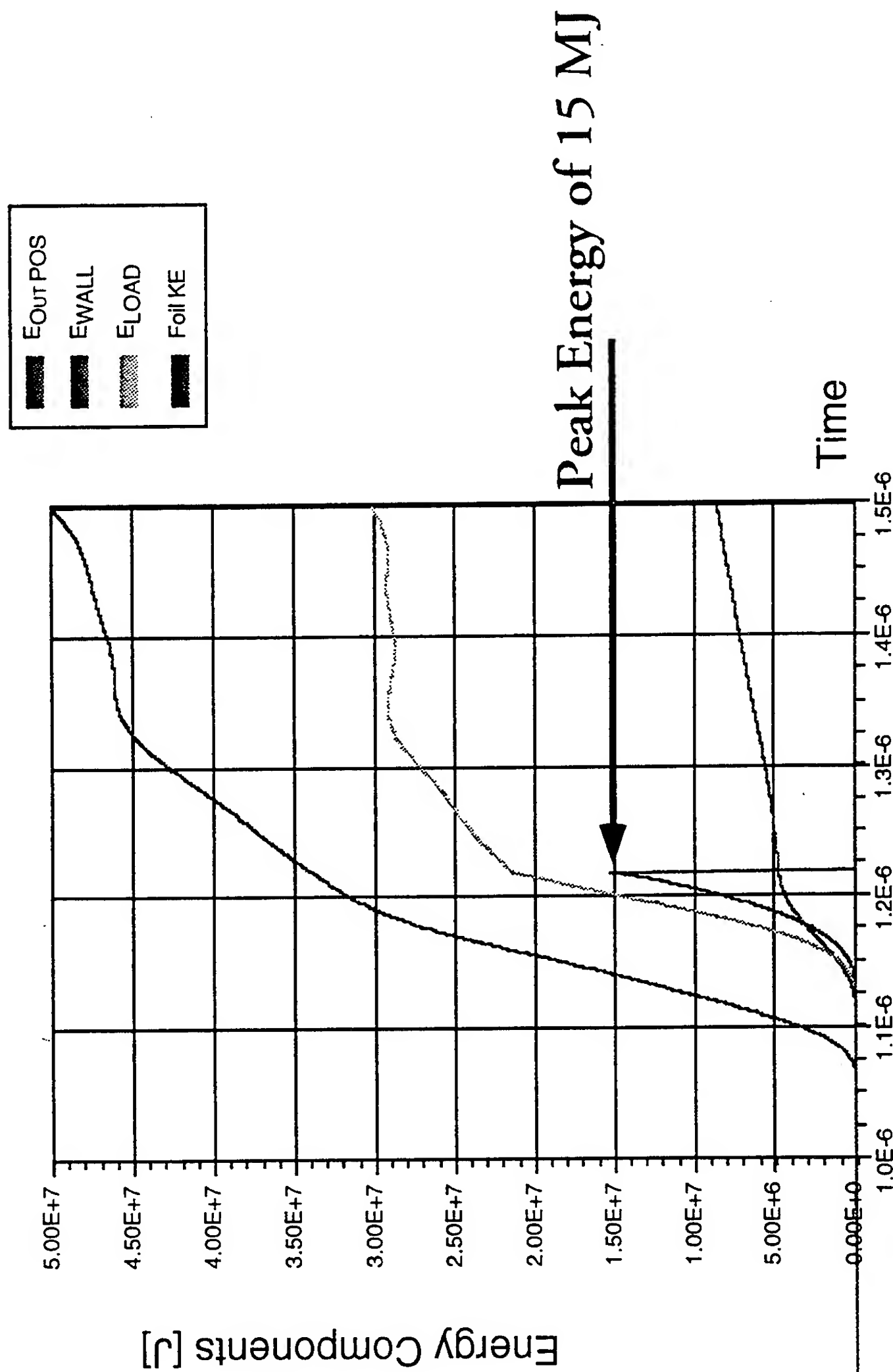
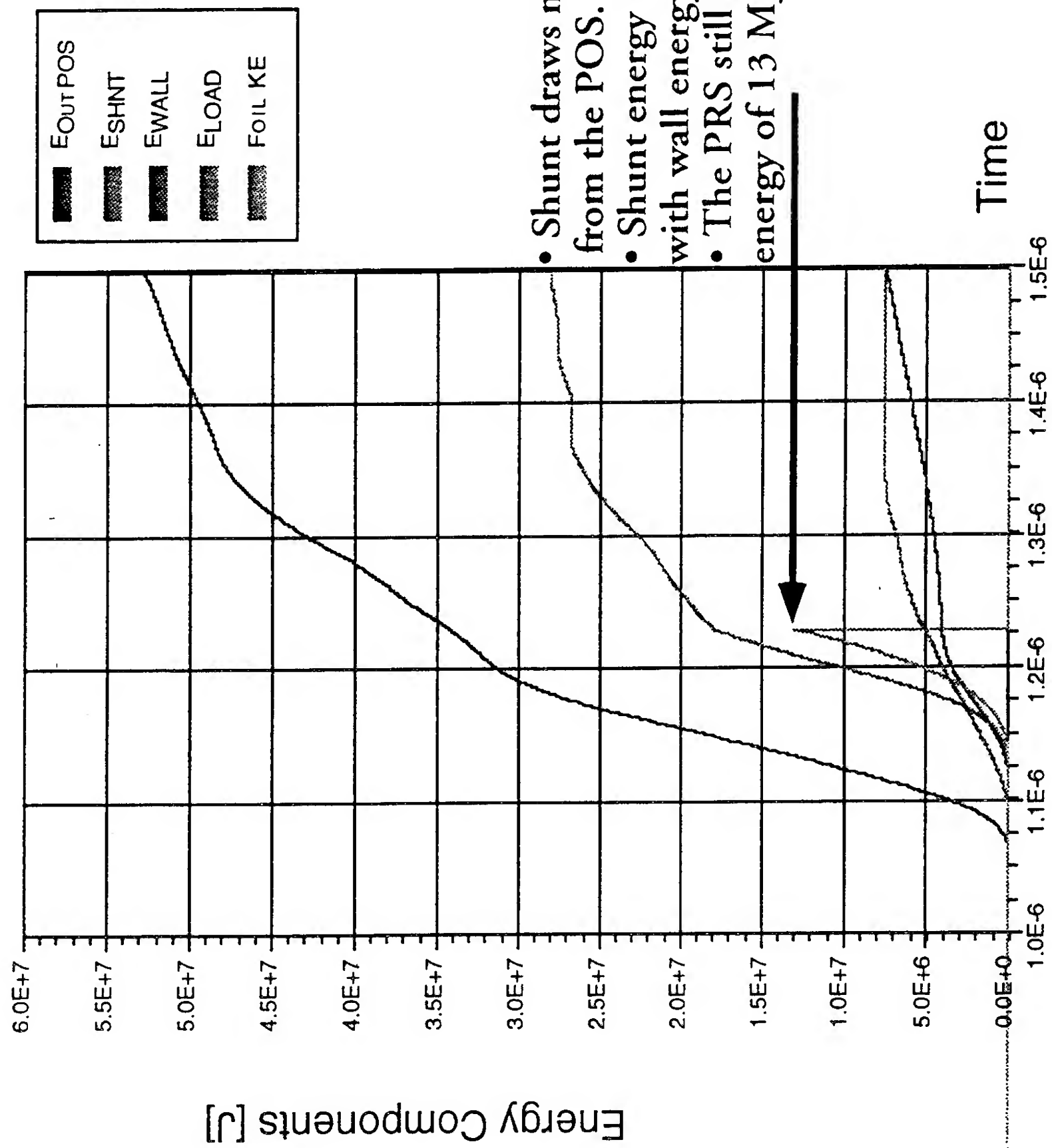


Fig. VI.4 Jupiter calculation with the shunt included



- Shunt draws more energy from the POS.
- Shunt energy is comparable with wall energy dissipation.
- The PRS still gets a peak energy of 13 MJ

## VII. DIAGNOSING THE OPACITY OF K SHELL LINES IN Z PINCHES

For many years, the K shell lines of elements of atomic numbers 10-18 have served as the workhorse in DNA simulators, providing copious yields of radiation in the 1-3 keV region. The strongest lines within the K shells of all of these elements are very optically thick, with optical depths typically in the hundreds. This high opacity surely is one of a number of factors which limit the achievable yields. Yet, until now, there has been no way to measure or even infer accurately the actual opacities of these lines. In analyzing the initial pinches produced on the ACE 4 inductive storage device at Maxwell Laboratories, Inc., a method has been discovered which can shed some light on this important issue. It also may provide us with potentially invaluable information about the underlying conditions of the Z pinch plasmas.

The essence of the technique involves the comparison of the measured and predicted yields arising separately from the K shell lines and continuum. Continuum radiation in the keV and harder spectral regions arises when electrons recombine radiatively with bare nuclei or the H-like stage of the element(s) radiating in the Z pinch. Experimentally, the line radiation virtually always exceeds that of the continuum, usually by factors of two or more. One may summarize the yield-producing status of the continuum by saying that it is significant but not dominant. Frequently, however, the models predict a greater fraction of the keV radiation to be in the continuum than is observed. Continuum cross-sections for the K shell ionization stages are known to high accuracy. When combining the expressions for the continuum optical depth with the known mass loadings and pinch sizes, it is easy to show that the continuum radiation optical depths cannot be more than a few tenths at most. *Therefore, in experiments using presently available machines, the lines will be greatly affected by absorption, but the continuum is essentially unaffected.*

This basic fact underlying the radiative emissions of multimegampere Z pinches provides a method of obtaining the opacity of the lines in an experiment. Since the line emission depends on the line opacity, but the continuum emission is independent of opacity, being thin, *the line-to-continuum ratio depends on the opacity of the lines.*

We now turn to a specific experiment to illustrate this. Some initial shots were taken on the ACE 4 device with the plasma opening switch not in operation. Neon puffs were used as the load, and the nozzle diameter was 5 cm in order to provide a preliminary test of the ability to get mass into a good radiating pinch despite the naturally long implosion times of an inductive store machine. Shot 871 has been analyzed in detail. In this shot, the neon took 380 ns to implode, and a final pinch of no more than 2 mm in diameter was observed. This factor of 25 compression is respectable, especially if a significant fraction of the  $145 \mu\text{g}/\text{cm}$  of the mass load was incorporated into the radiating pinch. A kilovolt radiation yield of  $3.5 \pm 1 \text{ kJ}$  was measured, with a pulsewidth of 48 ns.

The experimental time-integrated spectrum is shown in Fig. 1. Notable features are the approximately equal intensities of the H-like and He-like lines, and the dominance of the line radiation over the continuum, which is barely visible against the background. Lines comprise 75% of the keV radiation. In attempting to fit this spectrum and thereby diagnose the properties of the pinch (including the important factor of mass participation), one is constrained by the observed size of the pinch, as well as the line ratios and absolute measured yield. The opacity of the

lines is expected to be dominated by the Doppler effect of ion motion which broadens the lines. Assuming that the ion and electron temperatures are equal, and matching the ratio of the 1-2 principal resonance lines of the H- and He-like stages, as well as the yield and size of the pinch, the calculated spectrum is as shown in Fig. 2. Note the obvious discrepancy in the continuum. The H- and He-like recombination edges are easily visible on the theoretical spectrum but barely detectable to the eye on the actual measured pinch spectrum, Fig. 1. In Fig. 2, the calculated continuum comprises 60% of the keV and harder radiation whereas it is measured at 25%.

As shown in Fig. 3, this discrepancy can be cured entirely by adjusting the opacity of the lines. As greater broadening is assumed for the K shell lines, their output goes up, whereas that of the continuum, unaffected by opacity, does not. Therefore, the lower the line opacity, the higher the emitted line-to-continuum ratio. In Fig. 3, a fivefold broadening of the lines is assumed, and the line-to-continuum ratio is then calculated to be exactly as measured in ACE 4 shot 871. Therefore, the measurement of the relative yields in the lines and continuum has served to diagnose the opacity of the lines. We emphasize that even with the fivefold broadening, the lines are still quite optically thick, having optical depths of  $\sim 30$  rather than the unbroadened  $\sim 150$ . When the line opacity is reduced, the increased emissivity results in a greater yield, exceeding the experimental value, unless the inferred density is adjusted downward. Note from Figs. 2 and 3 that the diagnosed density has been halved, resulting in the yield as well as the line-to-continuum ratio being in agreement with experiment. The ion density of  $3 \times 10^{19} \text{ cm}^{-3}$  of Fig. 3 would indicate that about 22% of the mass load participated in the K shell radiation.

It is not known at present just what the source of reduced line opacity is. Two very good candidates are, first, that the ion temperature may be much higher than that of the electrons (Apruzese, et al., to be published in J. Comp. Phys.) and, second, various forms of plasma turbulence (Griem, Phys. Rev. A **33**, p. 3580; Whitney and Pulsifer, Phys. Rev. E **47**, p. 1968; Riley, Los Alamos National Laboratory Report No. UC-426). What is certain is that the opacity of the lines vitally affects their emissivity and thus the ultimate yield. We expect to apply this new diagnostic to other existing DNA simulators, and the results are to be incorporated in load designs and load physics analyses for future ultrahigh current machines.

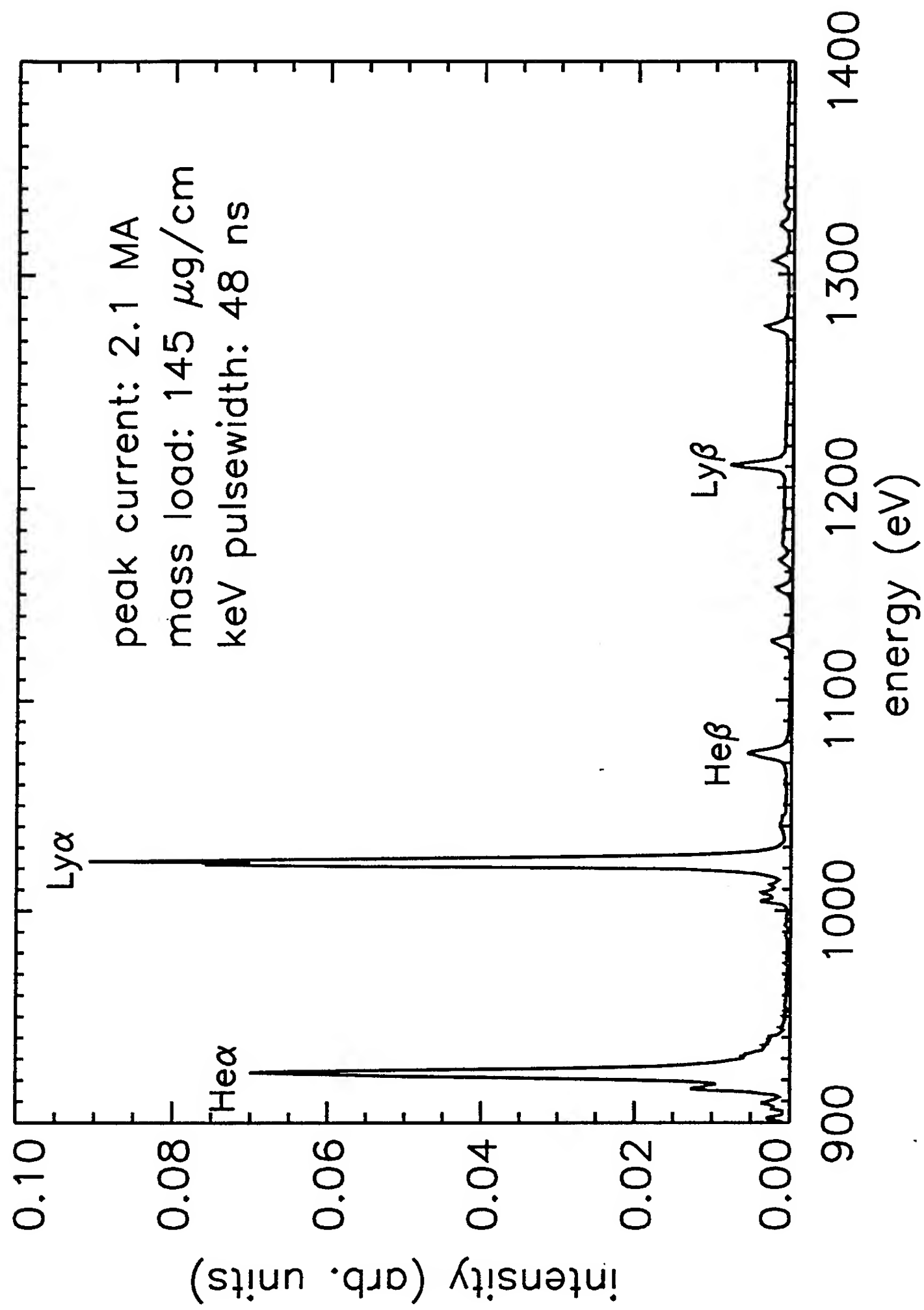


FIG. 1. Experimental spectrum obtained from ACE 4 shot 871.

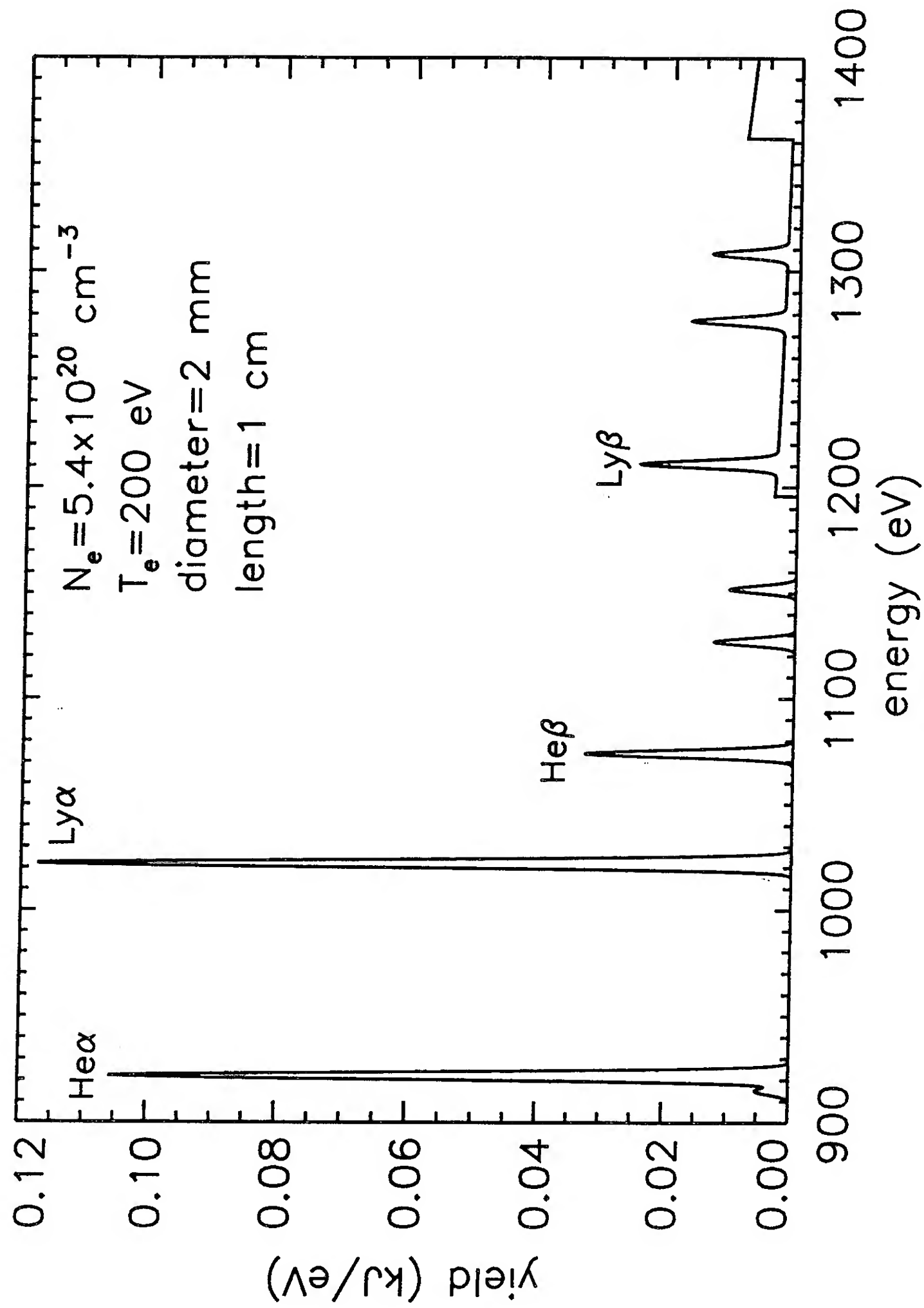


FIG. 2. Calculated spectrum for ACE 4 shot 871 which matches the total yield assuming that line opacity is dominated by the Doppler effect and also that the ion and electron temperatures are equal. Plasma conditions are as indicated.

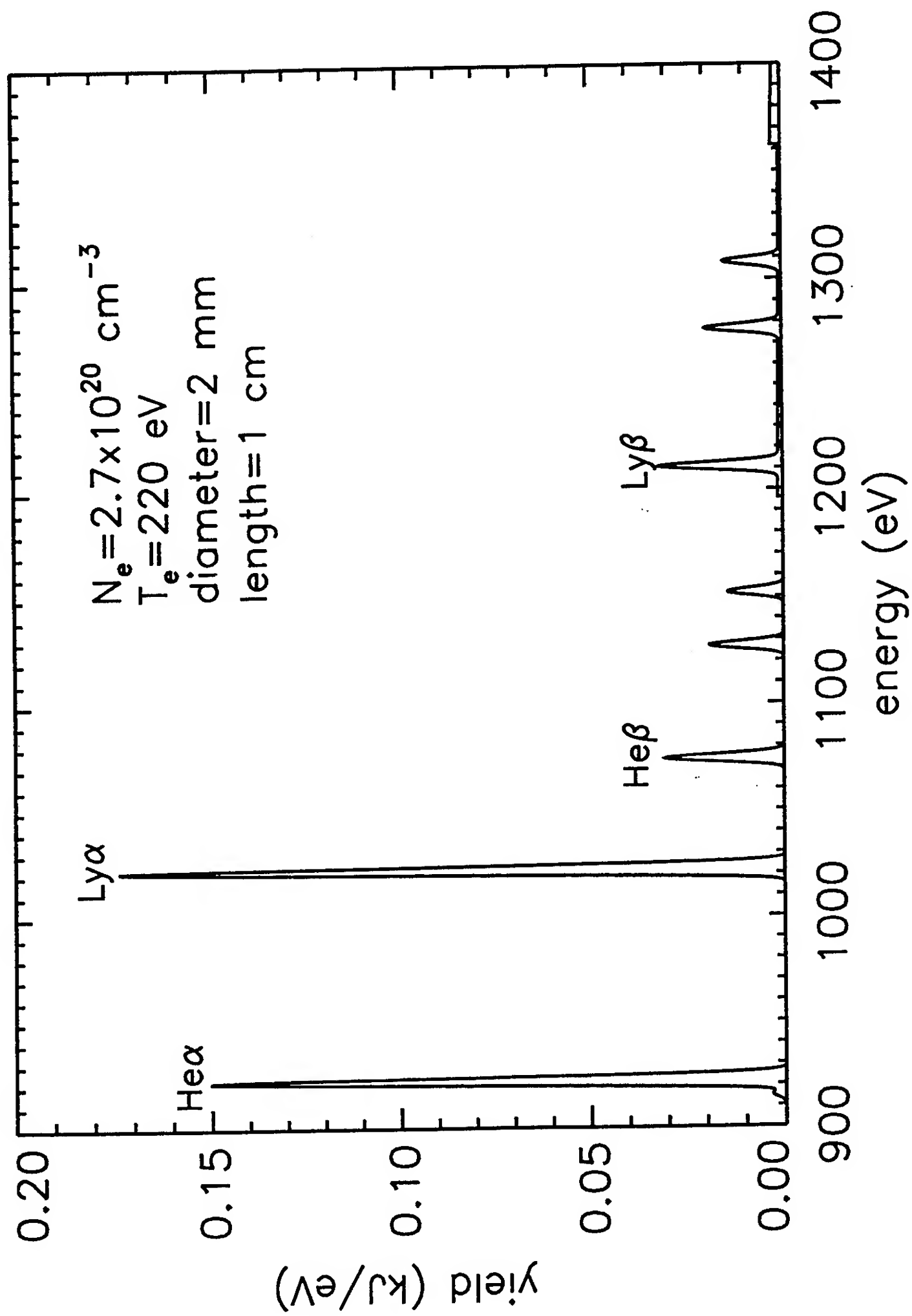


FIG. 3. As in Fig. 2, except that the lines have been broadened by a factor of 5, and the plasma conditions have been modified as indicated to continue matching the measured yield of ACE 4 shot

871.



## VIII. DIAGNOSING PLASMAS USING LINE RATIOS OF SATELLITE TO RESONANCE LINES IN THE L-SHELL

Presently, a great deal of effort is being expended to understand the dynamic processes of pinches, especially the radiation dynamics in hot dense state of Z-pinch plasmas with ions of medium to high nuclear charge.<sup>1</sup> Soft X-ray line spectra from Z-pinch plasmas have been extensively used to diagnose the hot plasmas for K-ions, i.e., ions for which the K-shell is excited.<sup>2-5</sup> Some of these ions also exist as impurities in tokamak discharges.<sup>6,7</sup> One- to three-electron ions are well studied because they entail relatively less complex calculations and experimental observations. Any careful analysis of X-ray emission involving ions with more than three electrons becomes complicated due, in part, to the difficulties of identifying the large number of satellite lines that cannot be resolved in wavelength from the resonance lines. Among the L-shell ions, the study of dielectronic satellite (DS) of resonance lines of Ne-like ions draws special interest because of its closed basic shell configuration and several published works report the use of DS lines of Ne-like ions for plasma diagnostics.<sup>8-10</sup>

Besides analyzing the line shapes from which the plasma ion temperature can be inferred, different kind of line ratios, such as the line ratios of satellite lines from two neighboring ionization stages as well as line ratios of resonance to DS lines of an element can be used for obtaining different information about the state and the dynamics of a plasma. These ratios have important consequences on the diagnosis of different plasma dynamic parameters because the different excitation mechanisms of the lines imply different dependences on these parameters.<sup>11,12</sup> For example, the line ratios of satellite lines from two neighboring ions depends mainly on the ratio of ion populations and thus they can be used to infer the state of ionization of the plasma. On the other hand, since the resonance lines are excited mainly by direct electron collisional excitation and the satellite lines are excited by dielectronic recombination(DR), the line ratios of DS to resonance lines are strongly temperature dependent. In this section we will demonstrate the effect of the ratios of the strong Ne-like resonance to Na-like DS lines in a selenium plasma on diagnosing the plasma's rate of ionization.

In most laboratory conditions the principal excited levels are populated by electron impact excitation from the ground state, and depopulated by spontaneous radiative decay. When these processes are much faster than any characteristic changes in the plasma, steady state rate equations can adequately describe the plasmas. For DECADE or PBFA II plasmas, however, ionization and recombination relaxation times will be longer than the duration of the plasma thermalization times and time-dependent or transient equations must be used for ionization calculations. However, in order to infer plasma characteristics using time dependent calculations and then compare them to experimental observations one will thus require time resolved spectra that are some times not available. But satellites of multiply charged ion resonance lines can be use as reliable ionization gauges provided these line ratios are obtained using detailed and accurate time dependent calculations and therefore future experimental endeavor must be geared towards generating spectrally informative, spatially and time resolved data that can be analyzed in accordance with accurate theoretical predictions.

Since the Ne-like resonance lines are often blended with DS lines and lines belonging to higher multiplicities become superimposed with the satellites, theoretical calculations with the inclusion of these considerations in the atomic model and sufficient spectral resolution in experimental investigations are also extremely important for accurate diagnostics. Previous diagnostic models were unable to predict accurately because they lacked these necessary theoretical considerations in their calculations and experimental refinements.<sup>13-16</sup> Traditionally, the analysis of these line ratios involve Maxwellian electron distributions. However, it is possible that plasmas produced in the laboratory by strong on axis thermalizations can generate time dependent non-Maxwellian ionization states that have significant effects on the line ratios of these plasmas.<sup>2,17,18</sup> In the future the effects of non-Maxwellian distributions on the ionization dynamics and hence on these line ratios will be evaluated.

Our Ne-like atomic model consists of 26  $n=3$  fine structure levels including four  $2p^53s$ , ten  $2p^53p$  and twelve  $2p^53d$ , 3 lumped inner-shell excited configurations of  $2p^63s$ ,  $2p^63p$ , and  $2p^63d$  and a lumped  $n = 4$  level.<sup>19</sup> We have developed the  $n=3$  multiplet levels of F-like ionization stage

of selenium in a similar fashion as was done for Ne-like selenium. Since our F-like selenium model is still in the developmental stage, we have used a less detailed atomic structure for our early calculations. Our compact F-like model consists of the ground state, the  $\Delta n=0$  excited state, 3  $n=3$  excited configurations of  $2p^4 3s$ ,  $2p^4 3p$  and  $2p^4 3d$ , 3 inner shell configurations of  $2p^5 3s$ ,  $2p^5 3p$  and  $2p^5 3d$  and a lumped  $n=4$  state. For the Na-like  $n=3$  excited states, all fine structure levels of the  $2p^6 3l$  as well as doubly excited  $2p^5 3l 3l'$  and  $2s 2p^6 3l 3l'$  states are included. The sodium-like, neon-like and fluorine-like models are embedded in a hydrogenic atomic model of selenium from which the ionization balance is calculated.<sup>20</sup>

In the present diagnostic work we considered the two strong resonance lines:

$$\{[2p^5(2p_{3/2})3d_{5/2}]_1 \rightarrow [2p^6]^1S_0\}(R_1)$$

$$\text{and } \{[2p^5(2p_{3/2})3d_{3/2}]_1 \rightarrow [2p^6]^1S_0\}(R_2)$$

of  $\text{Se}^{24+}$ . The five strongest satellite lines of Na-like selenium include:

$$\{[2p^5(2p_{3/2})3d_{5/2}3d_{5/2}]_{7/2} \rightarrow [2p^6(^1S_0)3d_{5/2}]_{5/2}\}(S_1),$$

$$\{[2p^5(2p_{3/2})3d_{3/2}3d_{5/2}]_{5/2} \rightarrow [2p^6(^1S_0)3d_{5/2}]_{5/2}\}(S_2),$$

$$\{[2p^5(2p_{1/2})3d_{5/2}3d_{5/2}]_{5/2} \rightarrow [2p^6(^1S_0)3d_{5/2}]_{5/2}\}(S_3),$$

$$\{[2p^5(2p_{2/2})3d_{3/2}3d_{5/2}]_{7/2} \rightarrow [2p^6(^1S_0)3d_{5/2}]_{5/2}\}(S_4),$$

$$\text{and } \{[2p^5(2p_{1/2})3d_{3/2}3d_{3/2}]_{3/2} \rightarrow [2p^6(^1S_0)3d_{3/2}]_{3/2}\}(S_5).$$

The following line formation mechanisms are considered in our calculations. For the resonance lines the most dominant contribution comes from direct electron-impact excitation (DE) from the ground state of  $\text{Se}^{24+}$ . Additional contributions due to resonance excitations (RE) whereby the upper levels of the lines are formed by the autoionization decay of the doubly excited states are included in calculating the intensities of the resonance lines. DR from  $\text{Se}^{25+}$  (F-like) ground and first excited states leave the Ne-like ion in the upper levels of the resonance lines. In considering this we have included cascades from all levels up to  $n=10$ . The contributions from the satellites with Rydberg levels  $n \geq 4$  formed due to DR from  $\text{Se}^{24+}$  that are unresolved from the resonance lines must also be taken into account in order to compare line ratios with experiments. However, in this calculation we have not yet included any such contributions. For the formation of the satellite

lines, we included DR from  $\text{Se}^{24+}$ . The satellite lines are formed on the long wavelength side of the resonance lines if the spectator electron is in states  $n=3$ . We also included inner-shell excitation (ISE) from  $\text{Se}^{23+}$ . Since this excitation process produces doubly excited states, and majority of these excitations decay by autoionization whereas the satellite lines are formed by radiative decay from these doubly excited states, the rate-coefficients for ISE is multiplied by the branching ratio  $A_r/(A_a + A_r)$ , where  $A_a$  and  $A_r$  are the autoionization and radiative transition probabilities respectively. The sodium-like and neon-like ground states are independent source terms and thus the populations of the upper levels for the satellite lines due to DR from the ground state and ISE from the Na-like states are added as separate contributions.

The atomic structure calculations were carried out using a modified version of the atomic structure code of R. D. Cowan,<sup>21</sup> called **CATS**.<sup>22</sup> The level energies, oscillator strengths and plane wave Born collision strengths were calculated using **CATS** for ISE from ground and excited states of  $\text{Se}^{23+}$ . For collision excitations from the ground state of  $\text{Se}^{24+}$ , we have used the collision strengths calculated by Zhang *et al.*<sup>23</sup> The excitation rate coefficients were obtained by numerically integrating these collision strengths over a Maxwellian distribution. DR branching ratios and rates to each specific fine structure levels from  $\text{Se}^{25+}$  to  $\text{Se}^{24+}$  and  $\text{Se}^{24+}$  to  $\text{Se}^{23+}$  states were calculated using the HFR (Hartree-Fock with relativistic) method of Cowan.<sup>21</sup> For the low lying doubly excited states the DR branching ratios were explicitly calculated, while for higher Rydberg states,  $1/n^3$  falloff of the DR branching ratios was used. Here  $n$  denotes the principal quantum number of the Rydberg electron.

The power emitted per unit volume for the Ne-like resonance lines are given by:

$$P_R = N_{Ne}^* A_r(j \rightarrow i) E_{ji}$$

and the power emitted per unit volume in a Na-like satellite line is :

$$P_S = N_e [N_{Ne} C_{DR} + N_{Na} C_E] [(A_r/A_a + A_r)] E_{ji}$$

where  $N_{Ne}$  and  $N_{Na}$  are the densities of Ne-like and Na-like ground states,  $N_{Ne}^*$  is the density of the excited state,  $N_e$  is the electron density,  $C_E$  and  $C_{DR}$  are the excitation and DR rate coefficients,

$A_r(j \rightarrow i)$  is the radiative decay rate from level  $j$  to level  $i$  and  $E_{ji}$  is the energy for the transition  $j \rightarrow i$ . The time dependent population densities of the excited states that are analyzed as well as the electron and ion temperatures, are imported into our analysis from time dependent coupled rate equation calculations.

The time histories of the electron temperature is shown for three different rates of plasma heating and ionization in figure 1. We can see the maximum temperature that was achieved in each case and also variations of the temperature within a 20 ps time duration from this figure. The rapid time variation of the electron temperature will affect the ionization stages of selenium and alter the strengths of recombination vs. excitation and ionization. In fact, when the plasmas burn through the L-shell to the K-shell quite rapidly, this will have significant effects on the line ratios. The contributions of ISE to the power emitted by the DS lines can be comparable to that due DR for some of the satellite lines in transient ionization. This can be seen from figure 2 where we show the energy output of one resonance line and a couple of satellite lines for the strongest heating rate (HR). These ISE contributions become much more important with the increase of plasma heating. The effect of ISE on the formation of the DS lines and hence on the line ratios can be seen by comparing the line ratios shown in figures 3 and 4. We can see significant contribution of ISE to the DS to resonance line ratios. As the electron temperature increases, the ratio will come more and more from ISE processes because of the exponent in calculating the ISE rate coefficients.

The ratio of the satellite lines whose upper levels are formed including both DR and ISE, to the resonance lines depend strongly on the ratio of Ne-like to Na-like ion populations. Thus as the plasma burns through the ionization stages, the depletion of Na-like selenium ions compared to that of the Ne-like ions will have important consequences on the line ratios and hence on the diagnostics of plasma parameters. The ratio of the sum of the satellites ( $n>3$ ) and that of the sum of the same DS to the resonance lines can be used to obtain a fractional population abundance ratio of two ionization stages in selenium. We investigated the dependence of the line ratios on changes in electron temperature by varying the heating rate. Even though we do not present the results of such investigation in this report, substantial variations have been seen in the relative line ratios showing

strong temperature dependence. The maximum electron temperature can be determined from the dielectric component of a Na-like satellite to the excitation component of a Ne-like resonance line. In figures 5 and 6 we present the maximum electron temperature and the maximum heating rate (HR) as a function of the line ratios. We thus see that the line ratios can be reliable thermometers in predicting the maximum electron temperatures and heating rates that can be achieved and a good indicator of predicting the maximum energy deposition per mass in a selenium plasma.

The time-dependent excitation and ionization balance formalism can be used to determine electron density from the line ratio of a pair of DS lines when one of them is density sensitive and the other one is not. As mentioned before intense heating will generate non-Maxwellian distributions which are predicted to have non-negligible effects on the line ratios and hence on the diagnostics of these strongly heated selenium plasmas. These non-Maxwellian distributions will be included in the near future to complete the calculations.

In conclusion, even though the complicated interactions that occur in the initial implosion phase of the Z-pinch plasma are not well understood as yet, it is apparent that in future high-current driven Z-pinch experiments involving medium to high Z plasmas, rapid "burn through" the L-shell is required. Thus an accurate and thorough analysis of the line emission in the L-shell spectra of these plasmas will be extremely relevant for a correct understanding of the dynamics of medium to high Z material pinches that are composed of different charged states. Such a study will also be very useful to draw inferences such as how long will the plasma remain in the L-shell states and how fast will the plasma ionize to even higher charge states and eventually burn through to the K-shell states. Based on the analysis presented in this section, we can conclude that an accurate determinations of line ratios will be very useful in predicting the energy absorbed per unit mass of the plasma and the amount of mass participation in the L-shell plasma. Such mass inferences provide a good indication of the quality of implosion and of the X-ray production in Z-pinch experiments.<sup>3</sup>



## REFERENCES

1. N. R. Pereira, J. Davis and N. Rostoker, Dense Z-Pinches, eds., Amer. Inst. Phys., New York (1989)
2. J. P. Matte, J. C. Keifer, S. Ethier, M. Chaker, and O. Peyrusse, Phys. Rev. Lett., **72**, 1208 (1994).
3. M. C. Coulter, K. G. Whitney, and J. W. Thornhill, J. Quant. Spectro. Radiat. Trans., **44**, 443 (1990).
4. V. A. Boiko, S. A. Pikuz, and A. Ya. Faenov, J. Phys. B: Atom. Mol. Phys., **12**, 1889 (1979).
5. A. Zigler et. al., Phys. Rev. A **45**, 1569 (1992).
6. M. Bitter et. al., Phys. Rev. Lett., **71**, 1007 (1993).
7. K. D. Zastrow, E. Kalline, and H. P. Summers, Phys. Rev. A, **41**, 1427 (1990).
8. W. H. Goldstein, R. S. Walling, J. Bailey, M. H. Chen, R. Fortner, M. Klapisch, T. Phillips, and R. E. Stewart, Phys. Rev. Lett, **58**, 2300 (1987).
9. S. Ya. Khakhalin, B. A. Bryunetkin, I. YU. Skobelev, A. Ya. Faenov, J. Nilsen, A. L. Osterheld, and S. A. Pikuz, JETP, bf8, 633 (1994).
10. J. Bailey, R. E. Stewart, J. D. Kilkenny, R. S. Walling, T. Phillips, R. J. Fprtnr, and R. W. Lee, J. Phys. B: Atom. Mol. Phys., **19**, 2639 (1986).
11. A. H. Gabriel, Mon. Not. R. Aston. Soc. , **160**, 99 (1972).
12. A. H. Gabriel and T. M. Paget, J. Phys. B: Atom. Mol. Phys., **5**, 673 (1972).
13. E. V. aglitski, V. A. Bioko, O. N. Krokhin et al., Kvant. Elektron., **1**, 2067 (1974).
14. V. A. Boiko, A. Ya. Faenov, and S. A. Pikuz, J. Quant. Spectr. Radiat. Transfer, **19**, 11 (1978)
15. P. G. Burkhalter and D. J. Nagel, Phys. Rev. A , **11**, 782 (1985).
16. J. F. Seely, T. W. Phillips, R. S Walling et al., Phys. Rev. A, **34**, 2942 (1986).



17. R. Bartiromo, F. Bombarda, and R. Giannella, Phys. Rev. A, **32**, 531 (1985).
18. A. H. Garbiel and K. J. H. Phillips, Mon. Not. R. Astr. Soc., **189**, 319 (1979).
19. A. Dasgupta and K. G. Whitney, Phys. Rev. A , **42**, 2640 (1990).
20. K. G. Whitney and M. C. Coulter, IEEE Trans. on Plasma Sci, **16**, 552 (1988).
21. Atomic structure code of R. D. Cowan following his book The Theory of Atomic Structure and Spectra (University of California Press, Berkeley, CA, 1981).
22. J. Abdallah, Jr., R. E. H. Clark, and R. D. Cowan, **Theoretical Atomic Physics Code Development I. CATS: Cowan Atomic Structure Code**, Los Alamos National Laboratory manual (December 1988).
23. H. L. Zhang, D. H. Sampson, R. H. Clark, and J. B. Mann, Atom. Data and Nucl. Data Tables, **37**, 17 (1987).

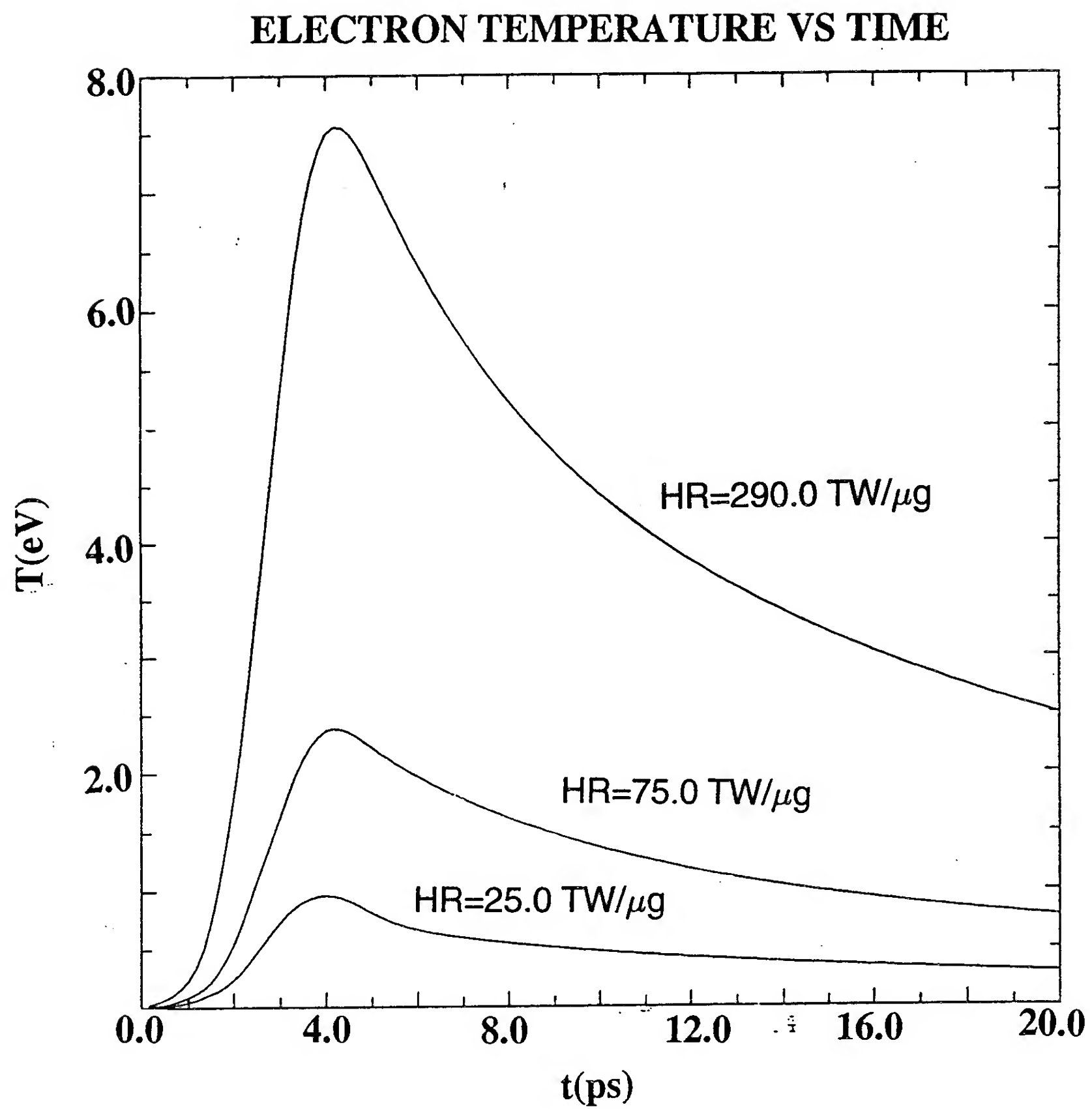


**Fig. 1**

# ENERGY OUTPUT OF RESONANCE AND SATELLITE LINES

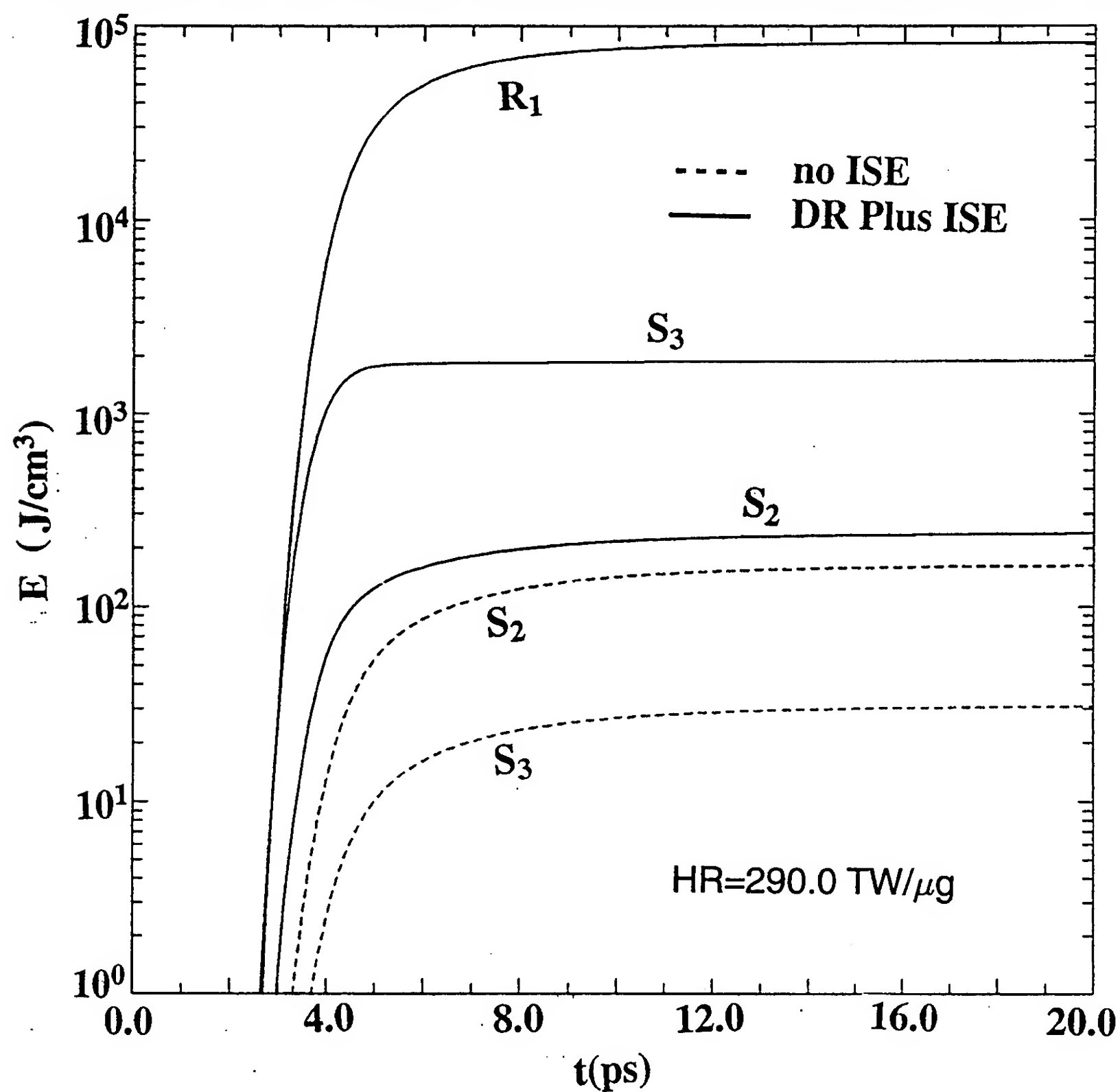
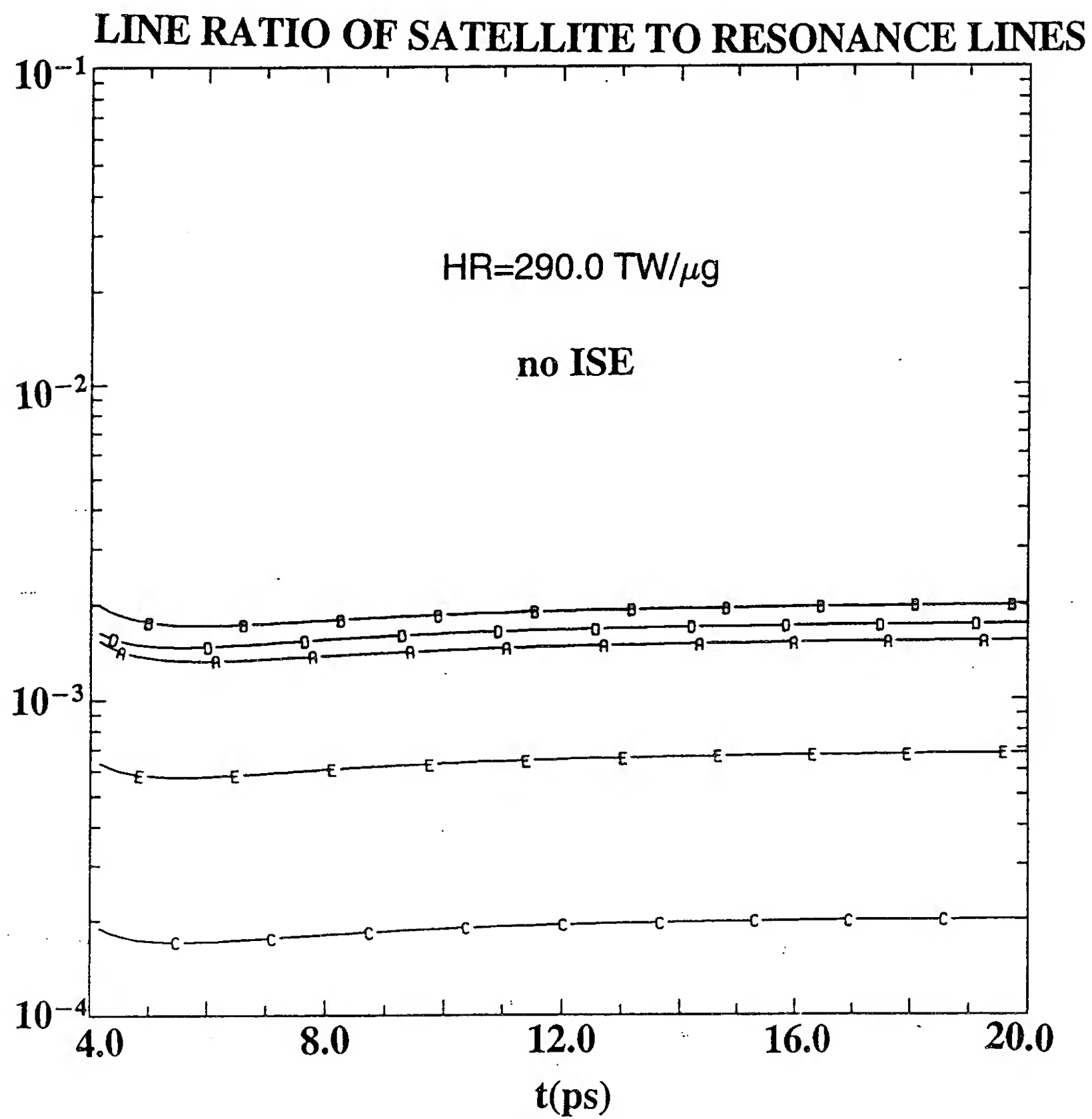
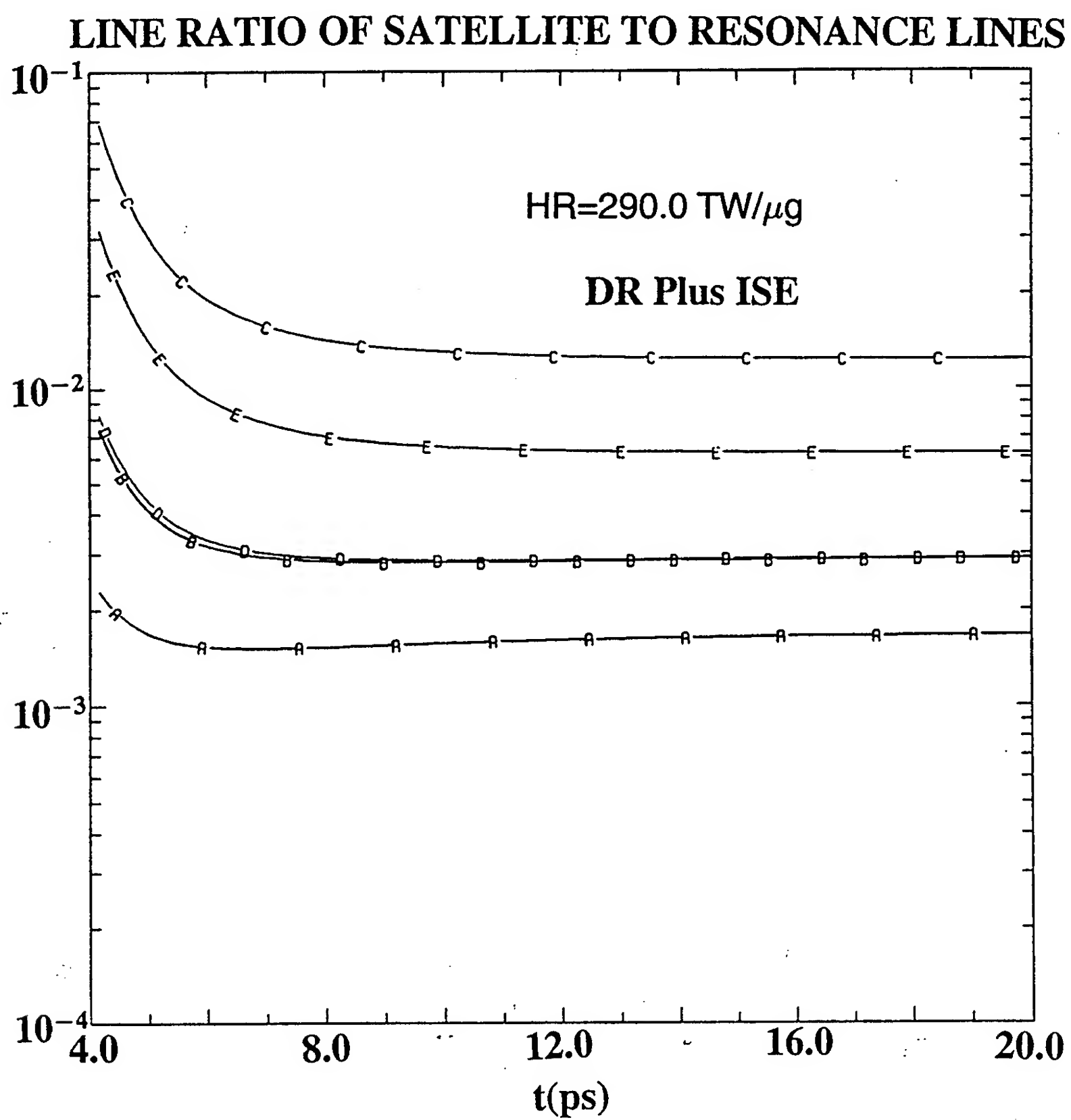


Fig. 2



**Fig. 3**



**Fig. 4**

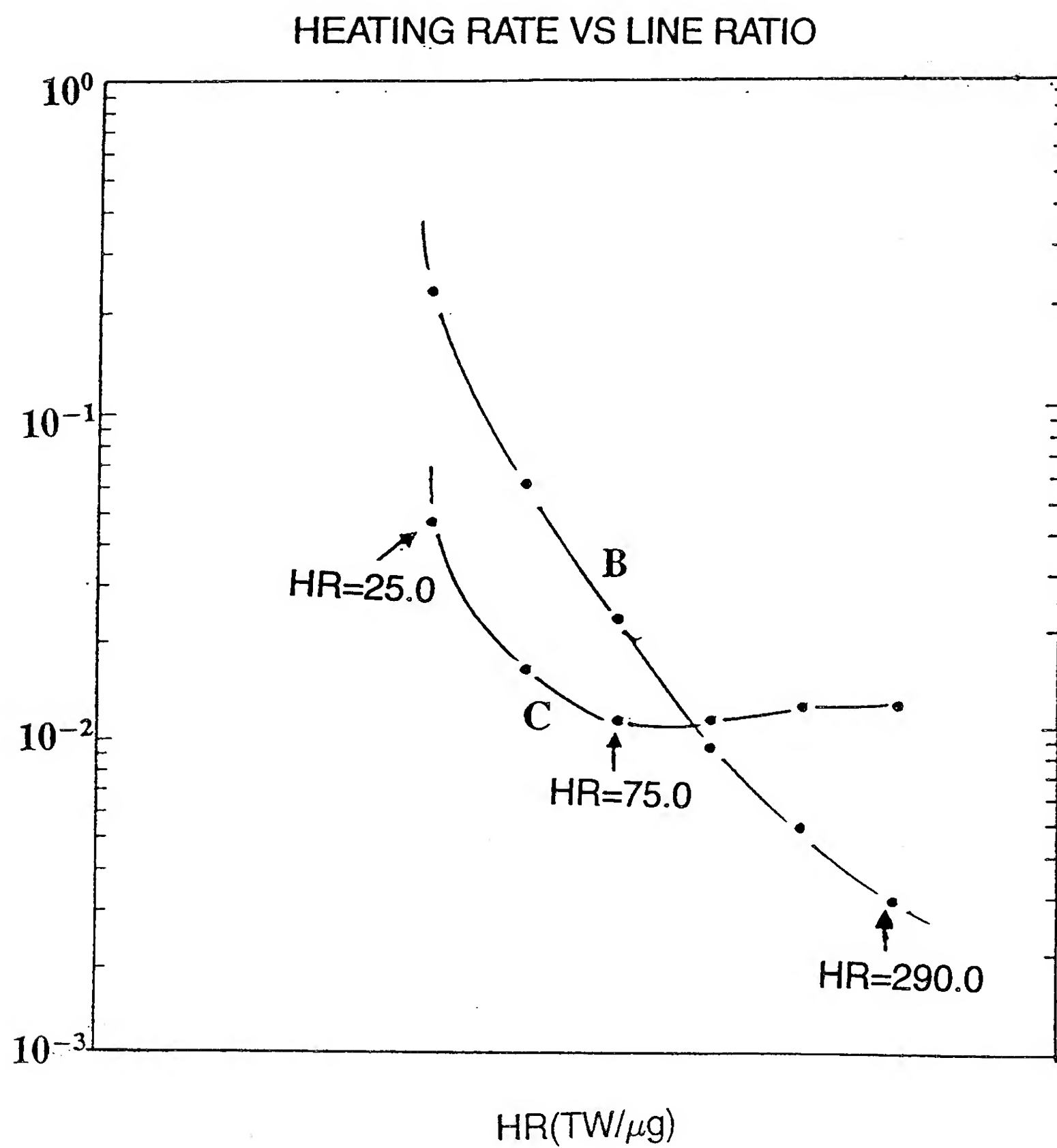


Fig. 5

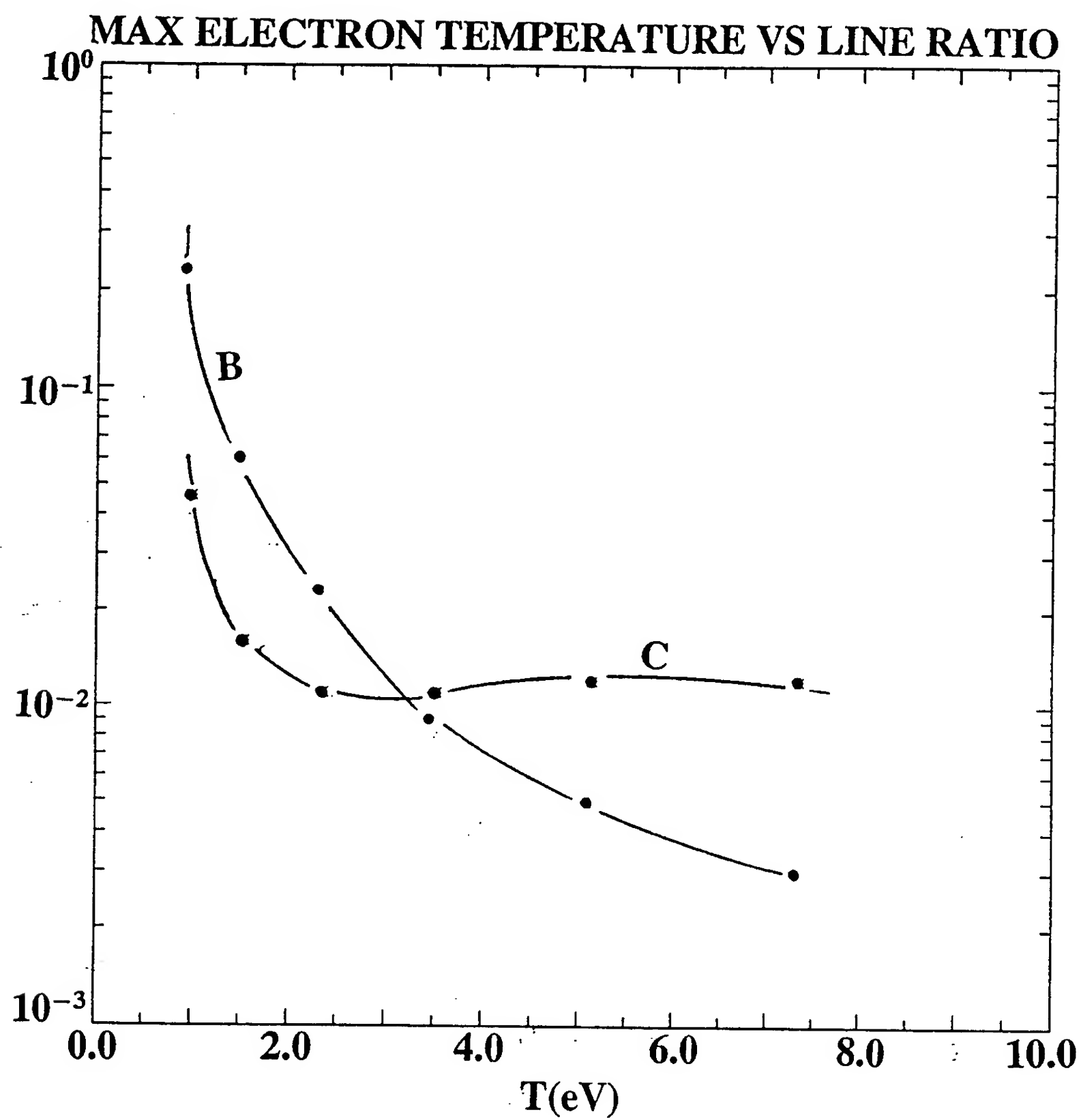


Fig. 6.